Theoretical investigation of nanoscale solid state and cluster structures on surfaces

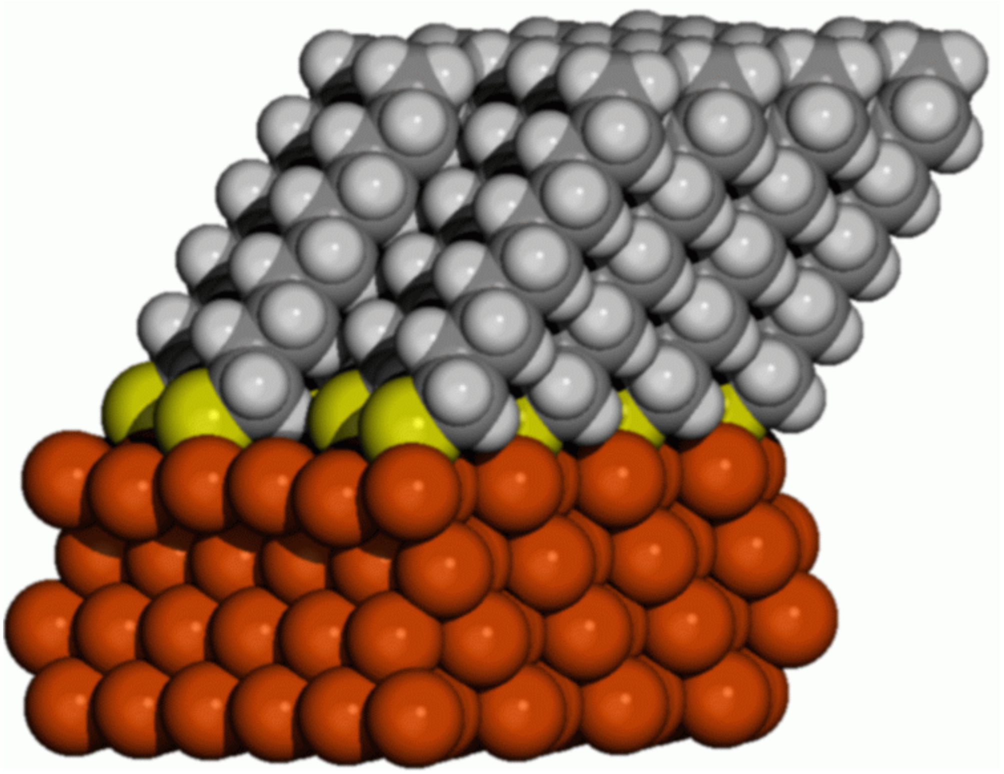

Dissertation

von

Dominik Fischer

Theoretical investigation of nanoscale solid state and cluster structures on surfaces

Dissertation

zur Erlangung des akademischen Grades
des Doktors der Naturwissenschaften (Dr. rer. nat.)
an der Universität Konstanz
Fachbereich Physik

vorgelegt von

Dominik Fischer

Tag der mündlichen Prüfung: 9.12.2002

Referent: Prof. Dr. Peter Nielaba
Referent: Prof. Dr. Wolfgang Dieterich

Contents

List of Figures **iii**

List of Tables **v**

1 Introduction **1**

2 Methods **5**

2.1 Density Functional Theory 5
2.2 Hohenberg Kohn Theorems 6
2.3 The Kohn-Sham Equations 7
2.4 Exchange-correlation Functionals 9
2.5 Practical Implementation of Kohn-Sham Scheme 11
2.6 Pseudopotentials 14
2.7 Calculation of the Total Energy 17
2.8 Optimisation Techniques 19
2.9 Car-Parrinello Molecular Dynamics 21
2.10 Summary 24

3 Hydrogenated Gold Cluster **25**

3.1 Introduction 25
3.2 Methods 27
3.3 Results and Discussion 29
  3.3.1 Bare gold clusters 30
  3.3.2 Structures and energetics of neutral and anionic Au_nH clusters . 32
  3.3.3 Vertical detachment energies and structural assignment 37
  3.3.4 How similar are Au_n and $Au_{n-1}H$? 46
  3.3.5 Electronic properties 55
  3.3.6 Vibrational properties 58
3.4 Summary 60

4 Deposited Si_4 Clusters **63**

4.1 Introduction 63
4.2 Methods 64
4.3 Results and Discussion 65
  4.3.1 Si_4 in the gas phase 65
  4.3.2 Si_4 on Au(111) 65

4.3.3 Si$_4$ on graphite . . . 70
4.4 Summary . . . 75

5 Self-assembled Monolayers on Au(111) 77
5.1 Introduction . . . 77
5.2 Experimental situation . . . 78
5.3 Previous Theoretical Studies . . . 82
5.4 Methods . . . 86
5.4.1 The quantum part . . . 87
5.4.2 The classical part . . . 89
5.4.3 QM / MM coupling . . . 90
5.5 Results and Discussion . . . 91
5.5.1 Energetics . . . 94
5.5.2 Structure . . . 99
5.5.3 Electronic properties . . . 110
5.6 Summary . . . 112

6 Summary 113

7 Zusammenfassung 115

A Conversion of Units 119

B Computational Details 121
B.1 Software . . . 121
B.2 Computational Requirements . . . 121
B.3 Input File . . . 122

Acknowledgment 125

Bibliography 134

List of Figures

2.1 Modelling of a surface in the supercell approach 12
2.2 Illustration of pseudopotential approach 15
2.3 Car-Parrinello method: Illustration of separation between electronic and ionic frequencies 24

3.1 Illustration of VDE and EA 29
3.2 Structures of Au_n clusters 31
3.3 Structures of $\mathrm{Au}_n\mathrm{H}$ clusters 35
3.4 Bond length in selected $\mathrm{Au}_n\mathrm{H}$ clusters 37
3.5 PES spectra for Au_n^- and $\mathrm{Au}_n\mathrm{H}^-$ 38
3.6 Calculated VDEs versus ΔE 39
3.7 Comparison of "parent-related" and "standard" interpretation 41
3.8 Formation channels for $\mathrm{Au}_n\mathrm{H}^-$ 42
3.9 Total energies and transition barriers for $\mathrm{Au}_5\mathrm{H}^-$ 42
3.10 ELF for Au_5 44
3.11 Transition barrier in $\mathrm{Au}_3\mathrm{H}^-$ 45
3.12 Comparison of the VDEs in different xc-functionals 46
3.13 Comparison of measured and calculated VDEs 47
3.14 Comparison of Au_n^- and $\mathrm{Au}_{n-1}\mathrm{H}^-$ structures 48
3.15 Illustration of charge transfer upon cluster formation 49
3.16 Electronic density of states for selected clusters 50
3.17 EDOS for $\mathrm{Au}_5\mathrm{H}^-$ and Au_6^- before and after electron detachment 52
3.18 $\Delta\rho$ for the three- and five-atom species 52
3.19 $\Delta\rho$ for the four- and six-atom species 53
3.20 Wavefunction of the detached electron for the sizes n=4 and 6 54
3.21 Cohesive energies for Au_n and $\mathrm{Au}_n\mathrm{H}$ 56
3.22 Dissociation energies for $\mathrm{Au}_n\mathrm{H}$ 57
3.23 HOMO-LUMO gaps for Au_n^- and $\mathrm{Au}_{n-1}\mathrm{H}^-$ 58
3.24 Vibrational spectra for selected cluster 59
3.25 Eigenmodes of selected $\mathrm{Au}_n\mathrm{H}^-$ clusters 60

4.1 Structure and DOS of Si_4 66
4.2 Illustration of Si_4 adsorption on Au(111) 67
4.3 Geometries of Si_4 on Au(111) 68
4.4 Trajectory of silicon atoms during an MD simulation of Si_4 on Au(111) 69
4.5 Structures of flat and three-dimensional Si_8 clusters 71

4.6 Approach of Si_4 clusters in different orientations 72
4.7 XPS spectra of deposited Si_4 on HOPG and amorphous carbon 74

5.1 Proposed unit cells for SAMs on Au(111) 79
5.2 All-trans and gauche configuration 80
5.3 Illustration of different adsorption sites 83
5.4 Equilibrium structures at low coverage 85
5.5 Illustration of QM/MM approach 88
5.6 Illustration for force field definition 90
5.7 Optimised geometries for different C10/Au(111) configurations 92
5.8 Side view of C10/Au(111) configurations 94
5.9 Energetics in dependence of chain length 96
5.10 Illustration of angles used to define the chain orientation 100
5.11 Side view of thiolate and disulfide models comparing surface relaxations 103
5.12 Illustration of hydrocarbon chain packing 105
5.13 Comparison of X-ray data to calculated diffraction patterns 107
5.14 Comparison of STM images to calculated topological maps 110
5.15 Electronic density of states for bare and adsorbed Au surface 111

List of Tables

3.1 Characteristics of Au_2 and AuH 28
3.2 Au_n: Energies, VDEs and EAs 30
3.3 Au_nH: Energies, VDEs and EAs 34
3.4 Bonding distances in Au_nH clusters 36

4.1 Characteristics of Si_2 65
4.2 Energetics and structure of Si_4 on Au(111) 68

5.1 Detailed position of adsorbed sulfur atoms 93
5.2 Overview of energetics: comparison of different models, chain lengths and coverages 95
5.3 Adsorption and cohesive energies: comparison of different models, chain lengths and coverages 98
5.4 Structural properties of monolayers 102
5.5 Structural analysis of gold surface 103
5.6 Structural analysis of headgroup-surface interface 104

B.1 Computational requirements of simulations 121

Chapter 1

Introduction

Richard Feynman's visionary talk [1] at Caltech in 1959 was the birth of nanoscience - the study of particles and structures with dimensions of the order of a nanometer (10^{-9} m). One of his challenging ideas was that "all of the information, that man has carefully accumulated in all books in the world, can be written... in a cube of materials one two-hundredth of an inch wide". Some decades later, science is still far away from that vision but the study of nanoscale systems has attracted great interest in research laboratories worldwide. A revolution in the investigation of sub-micron structures was triggered by the invention of the scanning tunnelling microscope (STM) by Binnig and Rohrer [2] in 1981. This microscope allowed researchers for the first time to obtain real space atomic resolution images of a sample surface. A further milestone was set ten years later when Don Eigler and co-workers [3] provided the first example of atomic manipulation. They discovered that by bringing the tip of an STM close to an adsorbed surface atom, individual atoms can be dragged along and positioned to build atomic-scale artificial structures. In a first demonstration of the technique they wrote the logo "IBM" with 35 xenon atoms on a nickel surface.

In recent years, the step was made from nanoscience to nanotechnology. Nanotechnology is the creation of functional materials, devices and systems through control of matter on the nanometer length scale. The ability to systematically organise and manipulate matter on the nanometer length scale promises various applications in electronics, optics, magnetics, catalysis etc. Supramolecular chemistry and molecular recognition are of great interest in the field of organic nanoscience. A key idea of nanotechnology is to exploit novel properties and phenomena developed due to that very small scale. For example, it was reported very recently that Au_{55} cluster (1.4 nm diameter) showed an impressively high resistance against oxidation, making these nanoparticles even nobler than bulk gold [4]. There is indeed need for new approaches to advanced materials since well-established techniques slowly reach their technical limits. A striking example is lithography, which is indispensable for the design of computer chips nowadays, which is believed to reach its fundamental limits in several years.

One of the main goals of nanotechnology is the arrangement of atomic-scale building blocks into technologically useful shapes. In order to fulfil this task, one has to think of suitable building blocks and sophisticated ways to arrange these building blocks into the desired structure.

One promising concept for nanofabrication is self-assembly. Self-assembly is the process in which atoms, molecules and aggregates of molecules arrange themselves in ordered functioning entities without the aid of human manipulation. It is a principle familiar in biology, where the right mix of biological molecules will interact on their own to form distinctive structures such as cells, tissues and organs. A nanodevice based on self-assembly is most likely still far in the future but less complex systems gave already a lot of insight. The probably best studied self-assembled structures are the self-assembled monolayers (SAMs). Around 20 years ago it was discovered that a stable, highly ordered monolayer can be prepared by simply exposing a gold surface to a dilute organosulfur solution [5]. The formation process of the monolayer is analogous to those in nature and rests upon the complex interplay of different interactions.

An appropriate choice of building block is crucial for the tailoring of materials with specific properties. In the preceding example, the nanostructure was made from organic molecules. Another type of building block is based on clusters. These promise to play a pivotal role as components in devices ranging from electronics to optics. Clusters are defined to be aggregates of a countable number of atoms (up to $\sim 10^6$) with a diameter in the nanometer range. It has already been demonstrated that new materials can be formed from particular stable clusters such as the famous C_{60}. Besides their possible application in nanoscale devices, clusters are of interest for many other reasons. As nanoparticles they constitute intermediates between molecules, with clearly defined energy states, and condensed matter, where these states form bands. Moreover, finite size effects occur in clusters that can lead to properties different from those of molecules or condensed matter. Another interesting aspect is the adsorption of atoms or molecules onto clusters. The high ratio of surface to bulk atoms suggests properties similar to a surface but in reality, the reactivity can be completely different to that of the surface which makes cluster nanoparticles attractive for the use in catalysis.

The great challenges on the way to nanotechnology are being tackled from both the experimental and theoretical side. Nowadays computers are so powerful that properties of materials can be predicted on the computer. Simulations can not only answer open questions that can not be solved by experiment but can also provide information about materials that do not even exist in the laboratory yet. In this way promising materials can be proposed by theory to be studied in more detail in experiment. A quantum-mechanical approach which is very widely used is density functional theory (DFT). This theory for which Walter Kohn was awarded the Nobel prize in 1998 allows the quantum-mechanical study of large physical or chemical systems without the usage of any empirical parameters. The high accuracy of this method allows a direct comparison between theoretical and experimental results revealing valuable information about system properties.

In this thesis, density functional theory was applied to three systems related to nanostructures and clusters: hydrogenated gold clusters Au_nH, deposited Si_4 clusters and self-assembled monolayers on gold surfaces.

In the first part of this thesis, hydrogenated gold clusters in the gas phase are studied up to a cluster size of seven atoms. Aggregates of gold are currently of great interest in nanoscience as they are key components in nanowires, catalysis and quantum dots. Here, the adsorption of hydrogen onto small gold clusters is studied. The structure of several isomers for each cluster size was calculated and compared to experimental data from photodetachment experiments. This procedure allowed the identification of the isomer that is present in the cluster experiment. Furthermore a surprising similarity between $Au_{n-1}H$ and Au_n that has been observed in experiments is investigated by analysing the numerical data. Finally, a detailed analysis of the electronic and vibrational properties of hydrogenated gold clusters is performed.

As already mentioned, highly stable clusters are believed to be building blocks of new materials. In the second part of this work, the eligibility of Si_4 clusters deposited onto different substrates was studied. The focus was on whether Si_4 clusters on a surface remain as individual species or, less desirably, coagulate to Si_8. The results from the DFT calculations are put into context with X-ray photoelectron measurements and conclusion are drawn concerning the usability of Si_4 clusters as a new building block.

The computational approach as applied in the last part of the thesis goes beyond the standard DFT scheme used in the rest of the thesis. In order to study self-assembled monolayers formed by adsorption of alkanethiol chains ($HS(CH_2)_{n-1}CH_3$) on a Au(111) surface, it was necessary to introduce additional classical interactions. The combination of quantum-mechanical methods with classical methods makes sure that all interactions in the system are treated accurately. Using this so-called “hybrid approach”, the long-lasting debate about the adsorption state of sulfur on the gold surface was investigated. Despite great experimental effort it is still unclear if upon adsorption a sulfur-sulfur bond is formed as suggested in the so-called “disulfide model” or if the chains adsorb as thiolates ($Au\text{-}S(CH_2)_{n-1}CH_3$) without formation of an S-S bond (“thiolate model”).

Parts of this thesis are already published:

- D. Fischer, W. Andreoni, A. Curioni, H. Grönbeck, S. Burkart and G. Ganteför, *Chemisorption on small clusters: Can vertical detachment energy measurements provide chemical information?: H on Au as a case study*, Chem. Phys. Lett., **361**, 389 (2002)

- M. Grass, D. Fischer, M. Mathes, G. Ganteför and P. Nielaba, *A new form of bulk silicon consisting of “magic” clusters?*, Appl. Phys. Lett., **81**, 3810 (2002)

- D. Fischer, A. Curioni and W. Andreoni, *Decanethiols on Gold: The Structure of Self-Assembled Monolayers Unravelled with Computer Simulations*, Langmuir, (accepted)

Chapter 2

Methods

2.1 Density Functional Theory

The computational method used throughout this thesis is based on density functional theory (DFT). It belongs to the class of *ab initio* methods which only rely on the laws of quantum mechanics. This distinguishes them from classical or semi-empirical methods which in contrast depend on empirical parameters derived from experimental data or quantum mechanical simulations. In comparison to other quantum methods, DFT is unique due to its appealing combination of computational efficiency and accuracy. For this reason DFT has become the standard approach to study systems in which a large number of atoms has to be considered as for instance adsorption processes on surfaces. Other methods like the configuration interaction [6] or diffusion Monte Carlo [7] are very accurate but for large systems the computational costs become extremely high since these methods scale with a high power of the number (N) of electrons ($\mathcal{O}(N^m), m \geq 4$). DFT on the other hand scales acceptably as a function of system size with ($\mathcal{O}(N^3)$) or even less with recently developed methods. The remarkable key idea in DFT is to replace the complicated N-electron wave function $\Psi(\mathbf{r}_1, \mathbf{r}_2, ..., \mathbf{r}_N)$ and the associated Schrödinger equation by the much simpler electron density $\rho(\mathbf{r})$ and its associated calculation scheme. The N-electron problem is reduced to N self-consistent 1-electron problems in effective potentials.

In this chapter an introduction into density functional theory and related methods will be given which is based on the Ref. [8–13]. After the derivation of the Kohn-Sham equations it will be demonstrated how DFT can be used efficiently in computer simulations. The discussion will address topics ranging from the choice of a basis set to exchange-correlation functionals to the pseudopotential scheme. Finally, an overview will be given on optimisation techniques and a very efficient molecular dynamics scheme as suggested by Car and Parrinello will be introduced.

Note, that the discussion presented here relies upon two assumptions. Firstly, it is assumed that ions can be regarded as classical particles. Secondly, only systems for which a separation between the classical motion of the ions and the quantum motion of the electrons can be achieved are considered, i.e. systems satisfying the Born-Oppenheimer adiabatic approximation. The idea of this approximation is, that due to the large difference in mass between the electrons and nuclei, the electrons respond essentially instantaneously to the motion of the nuclei. Therefore the nuclei can be treated adiabatically, leading to a separation of electronic and nuclear coordinates. Throughout this chapter the atomic units with e_0=m_0=$\hbar$=1 are used.

2.2 Hohenberg Kohn Theorems

In their landmark paper of 1964 Hohenberg and Kohn [14] proved that the ground state properties of a many-particle system are determined uniquely by the electronic density. Before focusing on the electronic density it is useful to reconsider the variational principle for the electronic wave function. Full minimisation of the functional

$$E[\Psi] = \frac{< \Psi|\hat{H}|\Psi >}{< \Psi|\Psi >} \tag{2.1}$$

with respect to all allowed N-electron wave functions will give the true ground state Ψ_0 and energy $E[\Psi_0] = E_0$; that is,

$$E_0 = \min_{\Psi} E[\Psi]\,. \tag{2.2}$$

If a wave function different from Ψ_0 is substituted in equation (2.1) an energy higher than E_0 will be obtained. It is now important to note that for an N-electron system, the external potential $V_{\text{ext}}(\mathbf{r})$ completely fixes the Hamiltonian and thus N and V_{ext} determine all properties for the ground state.

In place of N and V_{ext}, the first Hohenberg-Kohn theorem legitimises the use of the electron density $\rho(\mathbf{r})$ as basic variable. It states:

- *The external potential $V_{\text{ext}}(\mathbf{r})$ is determined, within a trivial constant, by the electron density $\rho(\mathbf{r})$.*

From this theorem together with the fact that ρ determines the number of electrons, it follows that $\rho(\mathbf{r})$ also determines the ground state wave function and all other electronic properties of the system. In particular, it determines the kinetic energy $T[\rho]$, the potential energy $V[\rho]$, and the total energy $E[\rho]$. The functional of the total energy E_v (v to make explicit the dependence on the potential) can then be written as

$$E_v[\rho] = \int \rho(\mathbf{r}) V_{\text{ext}}(\mathbf{r}) d\mathbf{r} + F_{HK}[\rho] \tag{2.3}$$

where

$$F_{HK}[\rho] = T[\rho] + V_{\text{ee}}[\rho]\,. \tag{2.4}$$

Here, V_{ee} includes all electron-electron interactions, whereas the nuclei-electron interactions are incorporated in the external potential V_{ext}.

The second theorem provides the energy variational principle:

- *For a trial density $\tilde{\rho}(\mathbf{r})$, such that $\tilde{\rho}(\mathbf{r}) \geq 0$ and $\int \rho(\mathbf{r}) d\mathbf{r} = N$,*

$$E_0 \leq E_v[\tilde{\rho}]\,. \tag{2.5}$$

This is analogous to the variational principle for wave functions in equation (2.1).

Note that the functional F_{HK} is defined independently of the external potential V_{ext} and thus it is a *universal functional* of $\rho(\mathbf{r})$. Therefore, once an appropriate expression for F_{HK} is found, it can be applied to any system. A look at the potential V_{ee} in equation (2.4) explains why this is a demanding task:

$$V_{\text{ee}} = J[\rho] + \text{non-classical term} \ . \tag{2.6}$$

Besides the electrostatic repulsion

$$J[\rho] = \frac{1}{2} \int \int \frac{\rho(\mathbf{r})\rho(\mathbf{r}')}{|\mathbf{r} - \mathbf{r}'|} d\mathbf{r} d\mathbf{r}' \tag{2.7}$$

it also includes all complex quantum mechanical effects. The non-classical term is a very important quantity in DFT and the major part of the exchange-correlation energy, discussed in the following sections, is based on this term.

2.3 The Kohn-Sham Equations

Density functional theory was turned into a practical tool for computer simulations by Kohn and Sham [15] who invented an elaborate indirect approach to the kinetic energy functional $T[\rho]$. The exact formula for the ground state kinetic energy of a system is

$$T = \left\langle \Psi | -\frac{1}{2}\nabla^2 | \Psi \right\rangle , \tag{2.8}$$

where Ψ is the N-electron wave function. According to the first Hohenberg-Kohn theorem the kinetic energy is a functional of the total electron density (s is a spin variable)

$$\rho(\mathbf{r}) = |\Psi(\mathbf{r}, s)|^2 \, . \tag{2.9}$$

Kohn and Sham showed that one can build a theory using simpler formulas, namely

$$T_s[\rho] = \sum_i^N \left\langle \Psi_i | -\frac{1}{2}\nabla^2 | \Psi_i \right\rangle \tag{2.10}$$

and

$$\rho(\mathbf{r}) = \sum_i^N \sum_s |\Psi_i(\mathbf{r}, s)|^2 \, . \tag{2.11}$$

This representation of the kinetic energy holds true for the determinantal wave function that exactly describes N *non-interacting* electrons.

The idea is now to introduce a *non-interacting* reference system, with the Hamiltonian

$$\hat{H}_{\text{s}} = \sum_i^N \left(-\frac{1}{2}\nabla_i^2 \right) + \sum_i^N V_s(\mathbf{r}_i) \tag{2.12}$$

in which there are no electron-electron repulsion terms, but its density equals the exact ground-state density of the *interacting* system. For this system there will be an exact determinantal ground state wave function

$$\Psi_s = \frac{1}{\sqrt{N!}} \det \left[\Psi_1 \Psi_2 .... \Psi_N\right] \tag{2.13}$$

where the Ψ_i are the N lowest eigenstates of the one-electron Hamiltonian $\hat{h}_s$:

$$\hat{h}_s \Psi_i = \left[-\frac{1}{2}\nabla_i^2 + V_s(\mathbf{r})\right] \Psi_i = \epsilon_i \Psi_i \tag{2.14}$$

The kinetic energy $T_s[\rho]$ of this system is given by equation (2.10). In order to use the expression for the kinetic energy of the non-interacting system $T_s[\rho]$, equation (2.4) is rewritten as

$$F_{HK}[\rho] = T_s[\rho] + J[\rho] + E_{\text{xc}}[\rho] \tag{2.15}$$

where

$$E_{\text{xc}}[\rho] \equiv T[\rho] - T_s[\rho] + V_{\text{ee}}[\rho] - J[\rho] \, . \tag{2.16}$$

The defined quantity $E_{\text{xc}}[\rho]$ is called the *exchange-correlation energy.* It contains the difference between T and T_s and the non-classical part of $V_{\text{ee}}[\rho]$.

The energy functional $E[\rho]$ in terms of the Kohn-Sham orbitals, as defined in equation (2.13), has the following form

$$E_v[\rho] = T_s[\rho] + J[\rho] + E_{\text{xc}}[\rho] + \int \rho(\mathbf{r}) V_{\text{ext}}(\mathbf{r}) d\mathbf{r} \, . \tag{2.17}$$

The total energy E_v has been split into four contributions:

1. the kinetic energy of the corresponding non-interacting system
2. the electrostatic energy
3. an exchange and correlation term
4. the interaction energy with the external potential

For the minimisation of the functional $E_v[\rho(\mathbf{r})]$, one has to take into account the constraint $\int \rho(\mathbf{r}) d\mathbf{r} = N$ using a Lagrange parameter μ.

$$\frac{\delta[E_v[\rho] + \mu(N - \int \rho(\mathbf{r}) d\mathbf{r})]}{\delta \rho(\mathbf{r})} = 0 \, . \tag{2.18}$$

Instead of varying the density, it is also possible to vary the one-particle wave functions $\Psi_i(\mathbf{r})$ whereby the constraint $\int \rho(\mathbf{r}) d\mathbf{r} = N$ is replaced by $\int |\Psi_i(\mathbf{r})|^2 d\mathbf{r} = 1$:

$$\frac{\delta[E_v[\rho] + \sum_{i=1}^{N} \epsilon_i (1 - \int |\Psi_i(\mathbf{r})|^2 d\mathbf{r})]}{\delta \Psi_i^*(\mathbf{r})} = 0 \, , \tag{2.19}$$

where ϵ_i are the corresponding Lagrange parameters. The minimisation of the energy functional leads to the Kohn-Sham equations

$$\left[-\frac{1}{2}\nabla_i^2 + V_{\text{eff}}(\mathbf{r})\right]\Psi_i = \epsilon_i\Psi_i\,, \tag{2.20}$$

where the effective potential V_{eff} is defined by

$$V_{\text{eff}}(\mathbf{r}) = V_{\text{ext}}(\mathbf{r}) + \int \frac{\rho(\mathbf{r}')}{|\mathbf{r}-\mathbf{r}'|}d\mathbf{r}' + V_{\text{xc}}(\mathbf{r})\,, \tag{2.21}$$

with the exchange-correlation potential

$$V_{xc}(\mathbf{r}) = \frac{\delta E_{\text{xc}}[\rho]}{\delta\rho(\mathbf{r})}\,. \tag{2.22}$$

These equations correspond to a system of non-interacting electrons moving in an external potential $V_{\text{s}}(\mathbf{r}) = V_{\text{eff}}(\mathbf{r})$. For a given $V_{\text{eff}}(\mathbf{r})$ one obtains the ground state density $\rho(\mathbf{r})$ by solving the N one-electron equations (2.20) and setting

$$\rho(\mathbf{r}) = \sum_i^N \sum_s |\Psi_i(\mathbf{r}, s)|^2\,. \tag{2.23}$$

The effective potential V_{eff} depends on $\rho(\mathbf{r})$ through equation (2.22). Hence, the equations (2.20), (2.21) and (2.23) have to be solved self-consistently. One begins with a guessed $\rho(\mathbf{r})$, constructs $V_{\text{eff}}(\mathbf{r})$ from (2.21) and then finds a new $\rho(\mathbf{r})$ from (2.20).

In conclusion, we have rewritten the variational principle stated in the Hohenberg-Kohn theorem as the solution of single-particle Schrödinger equations with an effective potential V_{eff}. By splitting the energy functional in equation (2.17), the system of interacting electrons in an external potential V_{ext} was mapped onto a system of non-interacting electrons in an effective potential V_{eff}, in such a way that the same electron density is obtained. This construction leads to the correct electron density but the wave function is not real. However, according to the first Hohenberg-Kohn theorem, the electron density is sufficient to have access to the ground state properties. Note, that the Lagrange parameters ϵ_i in equation (2.20) are not one-particle energies in DFT. However, it is a common procedure to compare theses values to experimental ionisation energies. In practice, this approach has turned out to be successful.

The Kohn-Sham equations can (like single-particle Schrödinger equations) in principle be solved exactly and the presented scheme is indeed exact. However, the exchange-correlation functional is not known and approximations have to be used to calculate this contribution to the total energy. In the following section different exchange-correlation functionals are presented.

2.4 Exchange-correlation Functionals

The exchange-correlation functional which has been widely used after the formulation of the Kohn-Sham theory is the local density approximation (LDA). It is based on the model of the homogenous electron gas, in which the electron density is constant throughout all space. For this system the exchange-correlation energy can be determined very accurately. The idea in LDA is, to approximate the exchange-correlation energy density at point $\mathbf{r}$ of the actual inhomogeneous system (i.e. the system of interest) with the corresponding expression of the homogenous electron gas $\mathrm{e}_{\mathrm{xc}}^{hom}$ $(\rho(\mathbf{r}))$:

$$E_{\mathrm{xc}} = \int \rho(\mathbf{r}) e_{\mathrm{xc}}^{\mathrm{hom}}(\rho(\mathbf{r})) d\mathbf{r} \,. \tag{2.24}$$

The exchange-correlation functional is obtained by differentiation of this expression:

$$V_{\mathrm{xc}} = \rho(\mathbf{r}) \frac{d e_{\mathrm{xc}}^{\mathrm{hom}}(\rho(\mathbf{r}))}{d\rho(\mathbf{r})} + e_{\mathrm{xc}}^{\mathrm{hom}}(\rho(\mathbf{r})) \,. \tag{2.25}$$

In most applications of LDA, the correlation energy is expressed by analytical parametrisations [16] of the results for the homogenous electron gas, as derived by Ceperley and Alder [17] from Quantum Monte Carlo simulations:

$$e_{\mathrm{c}}(\rho(\mathbf{r})) = \begin{cases} -0.1423 \,/\, (1 + 1.9529\, r_{\mathrm{s}}^{1/2} + 0.03334\, r_{\mathrm{s}}) & , r_{\mathrm{s}} \geq 1 \\ -0.0480 + 0.0311 \ln r_{\mathrm{s}} - 0.0116\, r_{\mathrm{s}} + 0.0020\, r_{\mathrm{s}} \ln r_{\mathrm{s}} & , r_{\mathrm{s}} < 1 \end{cases} \tag{2.26}$$

where

$$r_{\mathrm{s}} = \left(\frac{3}{4\pi\rho} \right)^{1/3} \tag{2.27}$$

is the Wigner-Seitz radius.

For the exchange energy the following expression is commonly used, which is obtained by evaluating the Fock integral for a Slater determinant of orbitals in the case of the uniform gas:

$$E_{\mathrm{x}}^{\mathrm{LDA}}[\rho] = -\frac{3}{2} \left(\frac{3}{4\pi} \right)^{1/3} \int \rho^{4/3}(\mathbf{r}) d\mathbf{r} \,. \tag{2.28}$$

LDA should in principle only be used for systems with a slowly varying density. However, LDA works well for many systems that go beyond this limit. This surprising success can most often be explained by the cancellation of errors. Other deficiencies are the inadequate cancellation of self-interaction contributions. As a consequence, the exchange-correlation potential, V_{xc}, does not exhibit the correct asymptotic behaviour proportional to $1/r$ for localised systems (atoms, molecules, etc.) but instead it declines exponentially.

A large improvement over the LDA approach was the introduction of the gradient of the density into the expression of the xc-energy:

$$E_{\mathrm{xc}}^{\mathrm{GGA}} = \int \rho(\mathbf{r}) e_{\mathrm{xc}}(\rho(\mathbf{r}); \nabla\rho(\mathbf{r})) d\mathbf{r} \,. \tag{2.29}$$

The so-called generalised gradient approximations (GGA) extended the applicability of DFT calculations significantly. Two of the most prominent examples of GGAs, which were also used in this thesis, are the PBE [18] and the BLYP [19, 20] functional. The analytic expressions for the GGAs are rather complicated. The expression for PBE, which is the most extensively used functional in this thesis, has the following form in the non-spin-polarised case:

The correlation energy is given by

$$E_{\mathrm{c}}^{\mathrm{PBE}} = \int \rho[e_{\mathrm{c}}^{\mathrm{hom}}(r_{\mathrm{s}}) + G(r_{\mathrm{s}}, \mathrm{t})]d\mathbf{r}\,, \tag{2.30}$$

where $t = |\nabla\rho|/2k_s\rho$ is a dimensionless gradient with $k_s = \sqrt{4k_F/\pi}$ as the Thomas-Fermi screening wave number ($k_{\mathrm{F}} = (3\pi^2\rho)^{1/3}$). The expression for the gradient contribution G is:

$$G = \gamma \ln\left\{1 + \frac{\beta}{\gamma}t^2\left[\frac{1 + At^2}{1 + At^2 + A^2t^4}\right]\right\}, \tag{2.31}$$

where

$$A = \frac{\beta}{\gamma}\left[\exp\{-e_c^{hom}/\gamma\} - 1\right]^{-1}, \tag{2.32}$$

and $\beta \simeq 0.066725$ and $\gamma \simeq 0.031091$.

The gradient-corrected exchange energy is given by

$$E_{\mathrm{x}}^{\mathrm{PBE}} = \int \rho(\mathbf{r})\,\epsilon_x^{\mathrm{hom}}(\rho(\mathbf{r}))\,F_{\mathrm{x}}(s)d\mathbf{r}\,, \tag{2.33}$$

where F_x is

$$F_{\mathrm{x}}(s) = 1 + \kappa - \frac{\kappa}{1 + \mu s^2/\kappa}\,, \tag{2.34}$$

with $\kappa = 0.804$ and $\mu = 0.219$. The enhancement factor F_{x} is a function of $s = |\nabla\rho|/2k_F\rho$.

2.5 Practical Implementation of Kohn-Sham Scheme

For the application of DFT in a computer simulation, an appropriate choice of the *basis set* and the *supercell* has to be considered. Different basis sets (e.g. localised orbitals, augmented plane waves, plane waves, etc.) have been applied to DFT. In the CPMD [21] program used for the calculations in this thesis, a plane wave basis set is used. This choice of expanding the single-particle orbitals into plane waves has several advantages:

- It permits the use of Fast Fourier Transformation techniques (FFT) which are computationally very efficient

- Plane waves do not depend on atomic positions therefore the forces acting on the nuclei can be calculated easily using the Hellman-Feynman theorem [22]. No Pulay forces [23, 24] occur.
- Plane waves are free of basis-set superposition errors.
- The convergence of plane wave calculations can be controlled in a very simple manner since it depends only on the number of Fourier components included in the expansion of the Ψ_i.

The drawback of a plane wave basis set is that a very large number of plane waves is needed to describe the electronic orbitals. This is in contrast to Gaussian or atomic-like basis sets where far fewer basis functions are needed. This problem is most severe for localised core states because high-energy plane waves have to be included in the expansion of the wave function (nothing smaller than the wavelength of the highest energy plane wave can be described). For a computationally affordable implementation a pseudopotential description of the interaction of ionic cores and valence electrons is necessary and this will be discussed in the next section.

In the simulation of bulk systems, the simulation box is periodically repeated in all three directions. The application of periodic boundary conditions (PBC) is the natural choice for the simulation of periodic systems because it implicitly introduces periodicity. In the case of a surface the periodicity in the surface plane is still given but there is no periodicity perpendicular to the surface. The supercell for a surface calculation is sketched in Fig. 2.1. It contains a crystal slab and a vacuum region. It is repeated over all space, so the total energy of an array of crystal slabs is calculated. To ensure that the results of the calculation accurately represent an isolated surface, the vacuum region must be wide enough so that faces of adjacent crystal slabs do not interact across the vacuum region. Moreover, the crystal slab must be thick enough

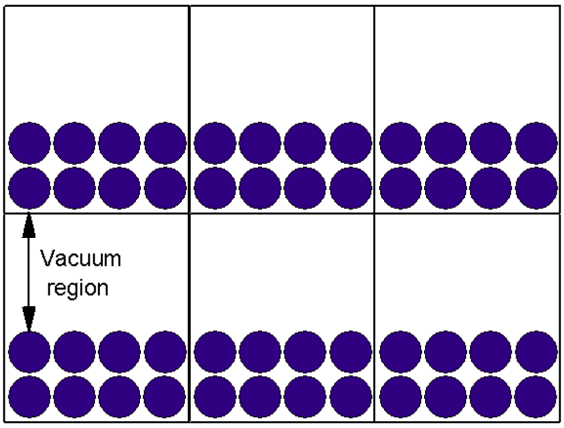

Figure 2.1: Modelling of a surface in the supercell approach. In this example the surface is modelled by a slab consisting of two layers (in reality more layers are used). The supercells are (enclosed by the solid lines) periodically repeated in all three directions. A vacuum region is introduced to decouple the slabs in the direction perpendicular to the surface.

so that the two surfaces of each crystal slab do not interact through the bulk crystal. Also molecules can be studied in this way if the supercell is chosen large enough that the interactions between the molecules are negligible.

In this supercell approach, one can take advantage of the translational symmetry of the Hamiltonian and use Bloch's theorem. This theorem states that the eigenstates of the periodic system Ψ_i can be chosen to have the form of a plane wave multiplied by a function with the periodicity $\mathbf{R}$ of the Bravais lattice:

$$\Psi_{i\mathbf{k}}(\mathbf{r}) = e^{i\mathbf{kr}} u_{i\mathbf{k}}(\mathbf{r}) \,, \tag{2.35}$$

where

$$u_{i\mathbf{k}}(\mathbf{r}+\mathbf{R}) = u_{i\mathbf{k}}(\mathbf{r}) \tag{2.36}$$

for all $\mathbf{r}$ in the Bravais lattice. The expansion of $u_{i\mathbf{k}}(\mathbf{r})$ as a sum of plane waves

$$u_{i\mathbf{k}}(\mathbf{r}) = \sum_{\mathbf{g}} c_{i\mathbf{k}}(\mathbf{g}) e^{i\mathbf{gr}} \tag{2.37}$$

with the reciprocal lattice vectors $\mathbf{g}$ of the supercell as the wave vectors, satisfies equation (2.36). Using this expression the expansion of the wave function takes the following form:

$$\Psi_{i\mathbf{k}}(\mathbf{r}) = e^{i\mathbf{kr}} \sum_{\mathbf{g}} c_{i\mathbf{k}}(\mathbf{g}) e^{i\mathbf{gr}} \,, \tag{2.38}$$

where $\mathbf{k}$ lies within the first Brillouin zone of the reciprocal lattice of the supercell. The coefficients $c_{i\mathbf{k}}(\mathbf{g})$ are the Fourier components of the single-particle wave function which are treated as time-dependent degrees of freedom in the calculation.

The basis set (2.38) which includes the infinite sum over the reciprocal lattice vectors is reduced to a finite set by truncating this sum to include only those plane waves with a kinetic energy $E_{\mathrm{K}} = \frac{1}{2}(\mathbf{k}+\mathbf{g})^{\mathbf{2}}$ less than a given energy E_{cut}. The value of E_{cut} depends on the specific system and in particular upon the choice of the pseudopotential for the description of the core-valence interaction. For a given pseudopotential, the choice of E_{cut} determines the accuracy of the calculation.
The computation of the electronic density $\rho(\mathbf{r})$ and then of the total energy requires an integral over the Brillouin zone:

$$\rho(\mathbf{r}) = \sum_{\mathbf{k}} w_{\mathbf{k}} \sum_{i} |\Psi_{i\mathbf{k}}(\mathbf{r})|^2, \tag{2.39}$$

where $w_{\mathbf{k}}$ is the k-point weight. The use of an appropriate $\mathbf{k}$-point mesh is the most efficient method to calculate the total energy of a periodic system. Equivalently, the calculation can be performed using a supercell consisting of replications of the unit cell and a single integration point for the Brillouin zone. In systems where the translational symmetry is broken, e.g. disordered systems or liquids, periodic boundary conditions can still be used if combined with a supercell approach. Therefore, in molecular dynamics simulations it is common to use large supercells and a single $\mathbf{k}$-point integration scheme. But also for systems in which large lattice relaxations are of importance, it is more appropriate to use a single **k**-point plus a large supercell than many **k**-points together with a cell that is too small to account for the relaxations.

The only point calculated in this approach is the centre of the Brillouin zone (Γ-point;$\mathbf{k}=\mathbf{0}$). This has the important computational advantage that at $\mathbf{k}=\mathbf{0}$, one can choose the single-particle orbitals $\Psi_i(\mathbf{r})$ to be real, since the phase factor of the wave function is arbitrary:

$$\begin{aligned} \Psi_i(\mathbf{r}) &= \Psi_i^*(\mathbf{r}) && (2.40) \\ \sum_{\mathbf{g}} c_i(\mathbf{g})e^{i\mathbf{gr}} &= \sum_{\mathbf{g}} c_i^*(\mathbf{g})e^{-i\mathbf{gr}}\,. && (2.41) \end{aligned}$$

This symmetry relation between the **g** and $-\mathbf{g}$ vectors has the consequence that only half of the Fourier components have to be stored and the computational costs of the Fourier transformation are reduced substantially. It should be noted that $\mathbf{g}=\mathbf{0}$ is a special vector and $c_i(0)$ becomes real. In general, for every operation on **g**, this special symmetry has to be taken into account (i.e. orthogonality). Setting $\mathbf{k}=\mathbf{0}$ in equation (2.38) the plane wave cutoff now simplifies to $\frac{1}{2}g^2 < E_{\text{cut}}$. All vectors with $|\mathbf{g}| < \mathbf{G_{max}}$ are included in the calculation where

$$\mathbf{g} = \frac{2\pi}{a}(i\mathbf{b_1} + j\mathbf{b_2} + k\mathbf{b_3}) \qquad (2.42)$$

and $\mathbf{b_1}, \mathbf{b_2}, \mathbf{b_3}$ are the reciprocal lattice vectors and i,j,k are integers. The number of **g** vectors depends on the shape of the unit cell and the cutoff and can be estimated by $\frac{4\pi}{3\Omega}E_{\text{cut}}^{3/2}$, where Ω is the volume of the unit cell.

2.6 Pseudopotentials

A plane-wave basis set is usually poorly suited to expanding electronic wave functions. This is because a very large number of plane waves are needed to expand the tightly bound core orbitals and to follow the rapid oscillations of the wave functions of the valence electrons in the core region. An extremely large plane-wave basis set would be required to perform an all-electron calculation. The pseudopotential approximation allows the electronic wave functions to be expanded using a much smaller number of plane-wave basis states.

It is well known that most physical properties of solids are dependent on the valence electrons to a much greater extent than on the core electrons. The pseudopotential approximation exploits this by removing the core electrons and by replacing them and the strong ionic potential by a weaker pseudopotential that acts on a set of pseudo wave functions rather than the true valence wave functions. The valence wave functions oscillate rapidly in the region occupied by the core electrons due to the strong ionic potential in this region (see Fig. 2.2). These oscillations maintain the orthogonality between the core wave functions and the valence wave functions, which is required by the exclusion principle. The most general form for a pseudopotential is

$$V_{\text{ps}} = \sum_{lm} Y_{lm}(\mathbf{r})V_l(\mathbf{r})\delta_{\mathbf{r},\mathbf{r}'}Y_{lm}(\mathbf{r}')\,, \qquad (2.43)$$

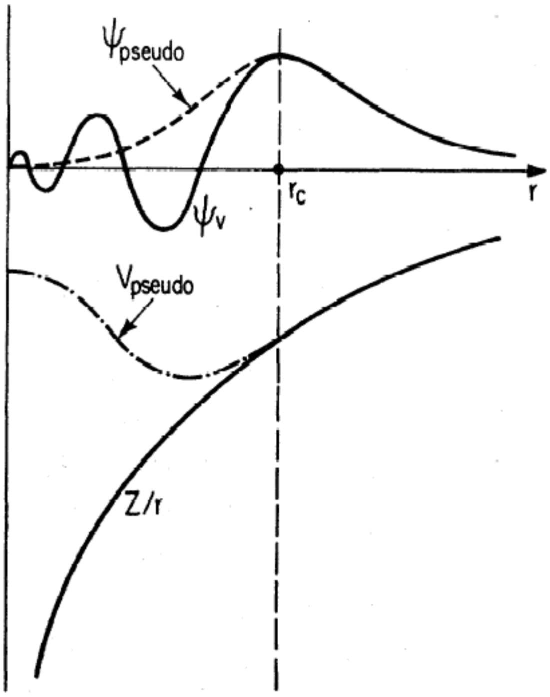

Figure 2.2: Illustration of the pseudopotential approach in the upper part the all-electron wave function Ψ_{v} and the pseudo wave function Ψ_{pseudo} are shown, in the bottom part the corresponding potentials. Outside a core radius r_c the all-electron and pseudoelectron values are identical (from Ref. [9]).

where Y_{lm} are the spherical harmonics and V_l is the pseudopotential for angular momentum l. A pseudopotential that uses the same potential for all the angular components of the wave function is called a local pseudopotential. A local pseudopotential is a function only of the distance from the nucleus. However, for most elements a fully local pseudopotential cannot accurately reproduce the properties of the all-electron wave functions.

There is a list of requirements for pseudopotentials to provide accurate results in computer simulations. Pseudopotentials are required to correctly represent the long range interactions of the core and to produce pseudo wave function solutions that approach the full wave function outside a core radius r_c. Inside this radius the pseudopotential and the wave function should be as smooth as possible, in order to allow for a small plane wave cutoff. For the pseudo wave function this requires that the nodal structure of the valence wave functions is replaced by a smooth function (Fig. 2.2). In addition it is desired that a pseudopotential is transferable, this means that the same pseudopotential can be used in calculations of different chemical environment. A major step to achieve all this conflicting goals was the introduction of "norm-conservation". The idea of "norm-conservation" is that the charge within the core radius is the same for the pseudo and true wave functions. Norm-conserving pseudopotentials have to be angular momentum dependent and thus are non-local.

In the Hamann-Schlüter-Chiang scheme [25] norm-conserving pseudopotentials in the so-called semi-local form were suggested. For most elements of the periodic table it is a good approximation to assume $V_l(\mathbf{r}) = V_{\bar{l}}$ for $l \geq \bar{l}$, where $\bar{l}$ is usually 1, 2 or 3. In this approximation the pseudopotential can be written as

$$V_{\mathrm{ps}}(\mathbf{r}) = V_{\mathrm{loc}}(r) + \sum_l \Delta V_l(\mathbf{r}) \hat{P}_l \,, \tag{2.44}$$

where $V_{\mathrm{loc}}(r)$ is the local potential and $\Delta V_l = V_l(r) - V_{\mathrm{loc}}(r)$ is the non-local (or more precisely) semi-local potential for the angular-momentum component l, and $\hat{P}_l$ projects out the lth angular-momentum component from the wave function. The local part of the pseudopotential is usually chosen to be the same as one of the $V_l(\mathbf{r})$.

The pseudopotentials are derived for the free atom by defining a core radius cutoff beyond which the bound pseudo wave-function matches the all-electron wave function. They have to satisfy the following conditions:

- For every angular-momentum channel, the pseudo eigenstates must have the same energy as the all-electron eigenstates.

- In the core region, the pseudo wave function is nodeless and carries the same charge as the all-electron wave function. This is known as the norm-conserving condition.

The second condition implies that the logarithmic derivative of the pseudo eigenstate matches the corresponding all-electron ones at any given point beyond the cutoff radius (r_c). This ensures that the pseudopotential gives an accurate description of the wave functions at energies close to the eigenvalues.

The typical method for generating an ionic pseudopotential proceeds as follows [9]. All-electron calculations are performed for an isolated atom in its ground state and some excited states, using a given form for the exchange-correlation functional. This provides valence electron eigenvalues and valence electron wave functions for the atom. A parametrised form for the ionic pseudopotential is chosen. The parameters are then adjusted, so that a pseudoatom calculation using the same form for exchange-correlation as in the all-electron atom gives both pseudo wave functions that match the valence wave functions outside some cutoff radius r_c and pseudoeigenvalues that are equal to the valence eigenvalues. The ionic pseudopotential obtained in this fashion is then used, without further modification, for any environment of the atom.

Note that a pseudopotential can be reproduced when the following information are given: the construction scheme (here: Hamann-Schlüter-Chiang, others are e.g. Troullier-Martins [26] or Bachelet-Hamann-Schlüter [27]), the cutoff radii and the reference state for the different angular momentum channels and the specification of the local part of the pseudopotential.

2.7 Calculation of the Total Energy

In the following only one **k**-point is included in the Brillouin zone sampling and the summation over **k** is dropped. The total energy of the system is given by the Hohenberg-Kohn energy functional and the ion-ion interaction energy E_M:

$$E = E_{\mathrm{k}} + E_{\mathrm{xc}} + E_{\mathrm{H}} + E_{\mathrm{ps}} + E_{\mathrm{M}}\,, \tag{2.45}$$

where

$$E_{\mathrm{M}} = \frac{1}{2}\sum_{I\neq J}\frac{Z_I Z_J}{|\mathbf{R}_I - \mathbf{R}_J|} \tag{2.46}$$

with $\mathbf{R}_I$ as the position of the nuclei I. The kinetic energy of the electrons is easily evaluated in Fourier space:

$$E_{\mathrm{k}} = \sum_{i,\mathbf{g}} \mathbf{g}^2 c_i^*(\mathbf{g}) c_i(\mathbf{g})\,. \tag{2.47}$$

The exchange-correlation is computed in real space whereby the electron density is calculated on a real space grid containing N_{R} grid points:

$$\begin{aligned} E_{\mathrm{xc}} &= \int e_{\mathrm{xc}}(\mathbf{r})\rho(\mathbf{r})d\mathbf{r} && (2.48)\\ &= \frac{\Omega}{N_R}\sum_R e_{\mathrm{xc}}(\mathbf{r})\rho(\mathbf{r})\,. && (2.49)\end{aligned}$$

The pseudopotential energy is given by

$$E_{\mathrm{ps}} = \int V(\mathbf{r})\rho(\mathbf{r})d\mathbf{r}\,, \tag{2.50}$$

where V is the total ionic potential acting on the electrons, expressed as a sum of ionic norm-conserving pseudopotentials V_{ps}:

$$V(\mathbf{r}) = \sum_I V_{\mathrm{ps}}(\mathbf{r} - \mathbf{R}_I) \tag{2.51}$$

According to the formulation of Hamann-Schlüter-Chiang (equation (2.44)) the energy E_{ps} is split into two contributions, a local ($\mathrm{E}_{\mathrm{ps}}^{\mathrm{L}}$) and a non-local one ($\mathrm{E}_{\mathrm{ps}}^{\mathrm{NL}}$):

$$E_{\mathrm{ps}}^{\mathrm{L}} = \int \rho(\mathbf{r})\sum_I V_{\mathrm{loc}}(|\mathbf{r} - \mathbf{R}_I|)d\mathbf{r}\,, \tag{2.52}$$

respectively

$$E_{\mathrm{ps}}^{\mathrm{NL}} = \sum_i \langle\Psi_i|V_{\mathrm{NL}}|\Psi_i\rangle\,, \tag{2.53}$$

where

$$V_{\mathrm{NL}} = \sum_I \sum_{l=0}^{\bar{l}-1} \Delta V_l(|\mathbf{r}-\mathbf{R}_I|)\hat{P}_l(\mathbf{R}_I)\,. \tag{2.54}$$

The operator $\hat{P}_l(\mathbf{R}_I)$ is the projector on the lth angular momentum with respect to the point $\mathbf{R}_I$. The evaluation of the terms E_{H}, $E_{\mathrm{ps}}^{\mathrm{L}}$ and E_{M} requires some care due to the presence of slowly decaying Coulomb forces. For this reason it is convenient to replace the ionic core point charges by smeared charge distributions ρ_I, e.g. Gaussians centred at the ionic sites:

$$\rho_I(\mathbf{r}-\mathbf{R}_I) = -\frac{Z_I}{(R_I^c)^3}(\pi)^{-3/2}\exp\left(-\frac{|\mathbf{r}-\mathbf{R}_I|^2}{(R_I^c)^2}\right)\,. \tag{2.55}$$

R_I^c determines the width of the Gaussian distribution associated with site I. The term E_{M} can now be expressed as follows:

$$E_{\mathrm{M}} = \frac{1}{2}\sum_{I,J}\int \frac{\rho_I(\mathbf{r}-\mathbf{R}_I)\rho_J(\mathbf{r}'-\mathbf{R}_J)}{|\mathbf{r}-\mathbf{r}'|}d\mathbf{r}d\mathbf{r}' - E_{\mathrm{self}} - E_{\mathrm{ovrl}}\,, \tag{2.56}$$

where the sum runs over all I and J. The term E_{self} is the self-interaction of the smeared charge and must be substracted out in equation (2.56) because it does not appear in equation (2.46), where the sum runs over I different from J:

$$E_{\mathrm{self}} = \frac{1}{2}\sum_I\int \frac{\rho_I(\mathbf{r}-\mathbf{R}_I)\rho_I(\mathbf{r}'-\mathbf{R}_I)}{|\mathbf{r}-\mathbf{r}'|}d\mathbf{r}d\mathbf{r}' = \frac{1}{\sqrt{2\pi}}\sum_I\frac{Z_I^2}{(R_I^c)^2}\,. \tag{2.57}$$

The term E_{ovrl} accounts for the difference between the original point-charge interactions and the interactions between smeared charges:

$$E_{\mathrm{ovrl}} = \frac{1}{2}\sum_{I\neq J}\left[\frac{Z_I Z_J}{|\mathbf{R}_I-\mathbf{R}_J|} - \int\frac{\rho_I(\mathbf{r}-\mathbf{R}_I)\rho_J(\mathbf{r}'-\mathbf{R}_J)}{|\mathbf{r}-\mathbf{r}'|}d\mathbf{r}d\mathbf{r}'\right]\,, \tag{2.58}$$

which can be evaluated using equation (2.55):

$$E_{\mathrm{ovrl}} = \frac{Z_I Z_J}{R_{IJ}}\mathrm{erfc}\left(\frac{R_{IJ}}{\sqrt{(R_I^c)^2+(R_J^c)^2}}\right)\,, \tag{2.59}$$

where R_{IJ}=$|R_I - R_J|$ and erfc as the “complementary error-function” defined by erfc(x)=$2/\sqrt{\pi}\int_x^\infty e^{-u^2}du$.

On performing the summation of the three terms E_{M}, E_{H} and $E_{\mathrm{ps}}^{\mathrm{L}}$: according to equations (2.52) and (2.56) we obtain:

$$E_{\mathrm{M}} + E_{\mathrm{H}} + E_{\mathrm{ps}}^{\mathrm{L}} = \frac{1}{2}\int\frac{\rho_{\mathrm{tot}}(\mathbf{r})\rho_{\mathrm{tot}}(\mathbf{r}')}{|\mathbf{r}-\mathbf{r}'|}d\mathbf{r}d\mathbf{r}' + \int\rho(\mathbf{r})\sum_I V_{\mathrm{loc}}^I(|\mathbf{r}-\mathbf{R}_I|)d\mathbf{r} - E_{\mathrm{self}} - E_{\mathrm{ovrl}}\,, \tag{2.60}$$

where $\rho_{tot} = \rho + \rho_I$, and

$$V^I_{\text{loc}}(r) = \left[V_{\text{loc}}(r) - \frac{Z_I}{r} \text{erf}\left(\frac{\text{r}}{\text{R}^{\text{c}}_{\text{I}}} \right) \right] . \tag{2.61}$$

Here, erf is the "error-function" defined by erf(x)=$2/\sqrt{\pi}\int_0^x e^{-u^2}du$. In equation (2.61) the term $-(Z_I/r)\text{erf}(r/R^c_I)$ results from $\int \rho_I(\mathbf{r}')/|\mathbf{r}-\mathbf{r}'|d\mathbf{r}'$. The smeared core charge which replaces the ionic core point charge can be treated in Fourier space, on the same footing as the electronic charge. The sum of electronic and smeared charges ρ_{tot} corresponds to the charge density of a *neutral* system and thus explicit evaluation of Madelung sums is avoided.

2.8 Optimisation Techniques

The search for the atomic configuration with the lowest potential energy is a basic task in computer simulations and needed throughout this thesis. The potential energy surface is generally a complicated, multi-dimensional function of the coordinates. A number of efficient methods exist, of which some will be introduced in this section, to determine a minimum on the potential energy surface. Note that if the number of atoms in the system is very large, it is extremely difficult to find the global minimum and often the optimisation process leads to a local minimum on the potential energy surface. To be more precise, these methods converge to a nearby stationary point. Another numerical task in DFT simulations is the solution of the self-consistent Kohn-Sham equations. For reasons of computational efficiency the Kohn-Sham equations are usually not solved by diagonalisation of the Hamiltonian but by optimising the wave function in an iterative process. In contrast to the problem of the optimisation of the ionic coordinates the Kohn-Sham energy functional normally has a single well defined minimum. Both cases can be generalised to a search for stationary points of a function F($\mathbf{x}$). Stationary points are defined by

$$\left. \frac{\partial F(\mathbf{x})}{\partial \mathbf{x}} \right|_{\mathbf{x}_k} = \mathbf{g}(\mathbf{x}_k) = 0 \, . \tag{2.62}$$

The stationary points are characterised according to the properties of the matrix of second derivatives:

$$\left. \frac{\partial^2 F(\mathbf{x})}{\partial \mathbf{x}^2} \right|_{\mathbf{x}_k} = \mathbf{H}(\mathbf{x}_k) \, . \tag{2.63}$$

If all eigenvalues of $\mathbf{H}$ are negative (positive) the stationary point corresponds to a maximum (minimum). In the case of negative and positive eigenvalues a saddle point was found.

The expansion of the function F($\mathbf{x}$) around $\mathbf{x}_k$ into a Taylor series is given by

$$F(\mathbf{x}) = F(\mathbf{x}_k) + g(\mathbf{x}_k)(\mathbf{x}-\mathbf{x}_k) + \frac{1}{2}(\mathbf{x}-\mathbf{x}_k)^\dagger \mathbf{H}(\mathbf{x}_k)(\mathbf{x}-\mathbf{x}_k) + \mathcal{O}(\mathbf{x}-\mathbf{x}_k)^3 \tag{2.64}$$

where $\mathbf{H}$ is the Hessian matrix of second derivatives. Minimisation techniques can be classified in two categories: first-order methods that use the first derivative (i.e. the gradients) and second-order methods that use both first and second derivatives.

A very simple first-order scheme is the method of "Steepest Descent". In the absence of any information about the function $\mathrm{F}(\mathbf{x})$, the optimum direction to move from the point $\mathbf{x}_k$ to minimise the function is just the steepest descent direction $\mathbf{g}_k$.

$$\mathbf{x}_{k+1} = \mathbf{x}_k - \alpha \mathbf{g}_k \tag{2.65}$$

If α is $>(<)0$ the walk is toward a minimum (maximum). This algorithm performs well when far off a stationary point. However, in a region near a stationary point it is more effective to use a more sophisticated method like the conjugate-gradients technique. Here, the basic idea is to restrict the search direction to paths that are orthogonal to all previous searches. Since minimisations along the conjugate gradient directions are independent, the dimensionality of the vector space explored in the conjugate-gradients technique is reduced by one at each iteration. Therefore the exact location of a minimum of a quadratic function will be found in a number of iterations that is equal to the dimensionality of the vector space. In practise, however, it is usually possible to perform the calculation so that far fewer iterations are required to locate the minimum. The conjugate gradients method moves in a direction $\mathbf{v}_k$ from point $\mathbf{x}_k$ where $\mathbf{v}_k$ is computed from the gradient at the point and the previous direction vector $\mathbf{v}_{k-1}$:

$$\mathbf{v}_k = -\mathbf{g}_k + \gamma_k \mathbf{v}_{k-1} \,, \tag{2.66}$$

where γ_k is a scalar constant given by

$$\gamma_k = \frac{\mathbf{g}_k \cdot \mathbf{g}_k}{\mathbf{g}_{k-1} \cdot \mathbf{g}_{k-1}} \,. \tag{2.67}$$

Second-order methods use in addition the second derivatives to locate a minimum. The advantage of using second derivatives in a minimisation scheme is that they provide valuable information about the curvature of the function what can be exploited to find stationary points more efficiently.

Using the information that the gradient is zero at the stationary point the first derivative of equation (2.64) can be written as

$$g(\mathbf{x}) = \mathbf{H}(\mathbf{x}_k)(\mathbf{x} - \mathbf{x}_k) + \mathcal{O}(\mathbf{x} - \mathbf{x}_k)^2 \,, \tag{2.68}$$

and solving this equation for $\mathbf{x}_k$ gives

$$\mathbf{x}_k = \mathbf{x} - \mathbf{H}(\mathbf{x}_k)^{-1} g(\mathbf{x}) + \mathcal{O}(\mathbf{x} - \mathbf{x}_k)^2 \,. \tag{2.69}$$

This scheme is called the "Newton-Raphson" method. For a purely quadratic function it finds the minimum in one step from any point on the surface. However, in practice the surface is only quadratic to a first approximation. This means that a number of steps will be required, at each of which the Hessian matrix must be calculated and inverted.

For a system with many atoms the inversion of the matrix becomes computationally very expensive.

An alternative approach is taken in the "quasi-Newton" methods in which the inverse Hessian is gradually built up in successive iterations instead of considering the exact Hessian. Here, a sequence of matrices $\mathbf{H}_k$ is constructed that has the property

$$\lim_{k\to\infty} \mathbf{H}_k = \mathbf{H}\,. \tag{2.70}$$

At each iteration k the new positions $\mathbf{x}_{k+1}$ are obtained from the current positions $\mathbf{x}_k$, the gradient $\mathbf{g}_k$ and the current approximation to the inverse Hessian matrix $\mathbf{H}_k$. Having moved to the new positions $\mathbf{x}_{k+1}$, $\mathbf{H}_k$ is updated from its value at the previous step according to a formula depending upon the specific methods being used. One of these methods, which was also used in the calculations for this thesis, is the Broyden-Fletcher-Goldfarb-Shano (BFGS) scheme [28–31]. Its update formula is given by

$$\begin{aligned}\mathbf{H}_{k+1} &= \mathbf{H}_k + \frac{(\mathbf{x}_{k+1}-\mathbf{x}_k)\otimes(\mathbf{x}_{k-1}-\mathbf{x}_k)}{(\mathbf{x}_{k-1}-\mathbf{x}_k)\cdot(\mathbf{g}_{k+1}-\mathbf{g}_k)} - \frac{[\mathbf{H}_k\cdot(\mathbf{g}_{k+1}-\mathbf{g}_k)]\otimes[\mathbf{H}_k\cdot(\mathbf{g}_{k+1}-\mathbf{g}_k)]}{(\mathbf{g}_{k+1}-\mathbf{g}_k)\cdot\mathbf{H}_k\cdot(\mathbf{g}_{k+1}-\mathbf{g}_k)} \\ &\quad +[(\mathbf{g}_{k+1}-\mathbf{g}_k)\cdot\mathbf{H}_k\cdot(\mathbf{g}_{k+1}-\mathbf{g}_k)]\mathbf{u}\otimes\mathbf{u}\,, \end{aligned} \tag{2.71}$$

where

$$\mathbf{u} = \frac{(\mathbf{x}_{k+1}-\mathbf{x}_k)}{(\mathbf{x}_{k+1}-\mathbf{x}_k)\cdot(\mathbf{g}_{k+1}-\mathbf{g}_k)} - \frac{[\mathbf{H}_k\cdot(\mathbf{g}_{k+1}-\mathbf{g}_k)]}{(\mathbf{g}_{k+1}-\mathbf{g}_k)\cdot\mathbf{H}_k\cdot(\mathbf{g}_{k+1}-\mathbf{g}_k)}\,. \tag{2.72}$$

The symbol $\otimes$ when interposed between two vectors means that a matrix is to be formed. The ijth element of the matrix $\mathbf{u}\otimes\mathbf{v}$ is obtained by multiplying $\mathbf{u}_i$ by $\mathbf{v}_j$. For the initialisation of $\mathbf{H}$ the unit matrix is often used. Finally, note that the method converges to a minimum, for a quadratic function of M variables, in M steps.

2.9 Car-Parrinello Molecular Dynamics

A very efficient molecular dynamics (MD) scheme was proposed by Car and Parrinello in 1985 [32]. Its great advantage over other MD schemes such as Born-Oppenheimer molecular dynamics is that the forces on the nuclei of the electronic structure are calculated "on-the-fly". In practice this means that for each geometry step only one wave function step has to be performed. This is in opposition to Born-Oppenheimer molecular dynamics where the Kohn-Sham equations have to be solved self-consistently after each change of the atomic coordinates.

The key idea of the Car-Parrinello method is the definition of a fictitious dynamical system whose potential energy surface E is an appropriate functional of both ionic and electronic degrees of freedom. The fictitious system is devised in such a way that the trajectories generated by its dynamics reproduce very closely those of the physical system with potential energy surface ν.

The classical Lagrangian of the *physical* system is given by the sum of the ionic kinetic energy and the ionic potential energy with reversed sign.

$$\mathcal{L}^{el} = \frac{1}{2}\sum_I M_I \dot{\mathbf{R}}_I^2 - \nu[\{\mathbf{R}_I\}]\,, \tag{2.73}$$

where M_I are the physical masses of the ions.

The generalised classical Lagrangian of the *fictitious* system is defined as

$$\mathcal{L} = \sum_{i=1}^{N} \int \mu_i |\dot{\Psi}_i(\mathbf{r})|^2 d\mathbf{r} + \frac{1}{2}\sum_I M_I \dot{\mathbf{R}}_I^2 - E[\{\Psi_i\}, \mathbf{R}_I] + \sum_{ij} \Lambda_{ij} \left(\int \Psi_i^*(\mathbf{r}) \Psi_j^*(\mathbf{r}) d\mathbf{r} - \delta_{ij} \right) . \tag{2.74}$$

$\mathcal{L}$ is a functional of two sets of classical degrees of freedom, the Ψ_i and the $\mathbf{R}_I$. The μ_i are arbitrary parameters of units (mass)×(length)^2 which play the role of generalised masses for the electronic degrees of freedom. For simplicity a unique μ is used for the Ψ_i independent from the electronic state. The first and second term in equation (2.74) are the kinetic energy of the electronic and ionic degrees of freedom. E is the potential energy of the coupled electron-ion fictitious system. The Lagrangian multipliers Λ_{ij} are used to impose orthonormality conditions on the Ψ_i.

The Euler equation associated with the Lagrangian of the *physical* system is

$$M_I \ddot{\mathbf{R}}_I = -\frac{\partial \nu[\{\mathbf{R}_I\}]}{\partial \mathbf{R}_I}\,. \tag{2.75}$$

The equations of motion derived from the Lagrangian of the *fictitious* system are

$$\mu \ddot{\Psi}_i = -\frac{\delta E}{\delta \Psi_i^*} + \sum_j \Lambda_{ij} \Psi_j\,, \tag{2.76}$$

$$M_I \ddot{\mathbf{R}}_I = -\frac{\partial E}{\partial \mathbf{R}_I}\,. \tag{2.77}$$

In general the trajectories generated by equation (2.75) and those obtained from equation (2.77) do not coincide unless $E[\Psi_i, \{\mathbf{R}_I\}]$ is at the instantaneous minimum. However, the parameter μ and the initial conditions for Ψ_{i0},$\dot{\Psi}_{i0}$ can be chosen in such a way that the time-scale for the electronic degrees of freedom is much shorter than that of the nuclei. In this case nuclear trajectories, initially lying on the Born-Oppenheimer surface, will deviate from it only after times that are significantly longer than the MD time step. In other words, if these parameters are chosen so that the two sets of classical degrees of freedom, ions and electrons, are only weakly coupled, the transfer of energy between them is small enough to allow the electrons to follow adiabatically the ionic motion, remaining close to the Born-Oppenheimer surface.

For a more qualitative discussion the fictitious temperature $\propto \sum_i^N \mu_i |\dot{\Psi}_i(\mathbf{r})|^2$ that is associated to the electronic degrees of freedom and the physical temperature $\propto M_I \dot{\mathbf{R}}_I^2$

of the nuclei may be considered. In this terminology, “low electronic temperature” or “cold electrons” means that the electronic subsystem is close to the exact Born-Oppenheimer surface. To ensure that the electronic subsystem stays cold also for long times the two subsystems have to be decoupled. This is possible if the power spectra stemming from both dynamics do not have substantial overlap in the frequency domain so that energy transfer from the “hot nuclei” to the “cold electrons” becomes practically impossible on the relevant time scales. An important question is under which circumstances the adiabatic separation can be achieved, and how it can be controlled. For a further understanding it is interesting to consider the dynamics generated by equation (2.76) when the ions are not allowed to move. The most noticeable feature of this dynamics is that it accounts for the quantum eigenvalue spectrum of the electrons. For small deviations from the ground state the dynamics of the ground state can be well described as a superposition of oscillations whose frequency is given by

$$\omega_{ij} = \left(\frac{2(\epsilon_j - \epsilon_i)}{\mu} \right)^{1/2} \tag{2.78}$$

where $\epsilon_j(\epsilon_i)$ is the Kohn-Sham eigenvalue of an empty (occupied) state. The lowest frequency that can appear is $\omega_{\min} = (2E_{\text{gap}}/\mu)^{1/2}$, where E_{gap} is the energy gap. This point is illustrated in Fig. 2.3, which shows the frequency spectrum of the velocity-velocity autocorrelation

$$\gamma(\omega) = \int_0^\infty \cos(\omega t) \sum_i \left\langle \dot{\Psi}_i(t) \dot{\Psi}_i(t) \right\rangle \tag{2.79}$$

for the occupied Kohn-Sham orbitals of a model system of 8 Si atoms in the diamond structure. One can see that there is a lower bound for the electronic frequency spectrum at about 1010 THz. This is in good agreement with the number given by the expression for $\omega_{\min}$ using the energy gap of the model E_{gap}=2.24 eV and the fictitious electron mass used in the simulation μ=300 a.u. This value has to be compared with the highest ionic frequency for this model which is Ω=140 THz. This large difference in frequencies, e.g. the clear separation between electronic and ionic characteristic frequencies, is the clue to understanding how the Car-Parrinello method works. If the system is initially prepared in the instantaneous ground state with zero velocity, then the high-frequency motion of the electrons will ensure that they follow the motion of the atoms adiabatically, while the irreversible energy exchange between the fast and slow degrees of freedom is kept very small.

Considering equation (2.78) it is obvious that the smaller the value of μ the better the adiabaticity is preserved. However, small values of μ result in small values for the integration time step. In practice a satisfactory compromise between these two opposite requirements has to be found. From this discussion it is also clear that if E_{gap} is small one needs a very small value of μ to obtain an adiabatic separation of ionic and electronic frequencies. In the case of metals, E_{gap} is vanishing in an infinite system and very small in a finite one. Therefore it is much harder to perform Car-Parrinello molecular dynamics simulations for metals than for insulators or semiconductors. Generally for reasonable values for the time step electrons quickly slide

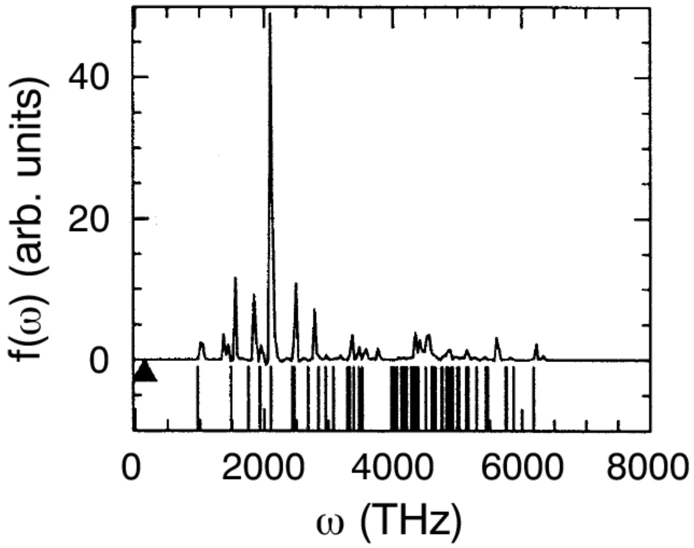

Figure 2.3: The vibrational spectrum of the normal modes of the electronic degrees of freedom for a system with a large gap (8 Si atoms in the diamond structure). The triangle indicates the position of the highest ionic frequency. The vertical bars below the spectrum represent the frequencies from equation (2.78) (from Ref. [33]).

away from the Born-Oppenheimer surface what leads simultaneously to a cooling of the ions. An improvement can be achieved when two different thermostats are applied, one to the ionic and the other to the electronic degrees of freedom. The role of the two thermostats is to maintain the ions at the desired temperature while at the same time keeping the electrons “cold”.

2.10 Summary

In this chapter a computational scheme was presented that enables the quantum-mechanical description of systems from physics and chemistry. Its great advantage is, that it does not depend on empirical parameters and therefore the results are not biased by the specific choice of the parameters. The scheme based on density functional theory provides a very useful tool to understand and interpret experimental data. It provides the high accuracy needed and at the same time it gives access to properties that can be directly compared to experiment. In addition, due to its computational efficiency it is possible to study systems at a size scale which is not accessible by other methods. For these reasons DFT is the method of choice to study the systems of interest in this thesis: nanostructures at surfaces and clusters.

Chapter 3

Hydrogenated Gold Cluster

3.1 Introduction

Clusters are defined as aggregates of atoms ranging from three to about 10^6. Due to this size regime clusters exhibit a variety of interesting properties. At small sizes, the addition of a single atom to a cluster can change the properties of the cluster dramatically. For example the high stability of some alkali clusters (n=8,20,40,..) is caused by the stepwise evolution of the electronic structure that leads to electronic shell closings responsible for the enhanced stability [34]. These clusters as well as clusters with a closed geometric shell (e.g. the icosahedron Al_{13}) are much more stable than those with one atom more or less. Another interesting aspect is, that clusters represent the bridge between molecular and bulk systems. The electronic structure of the clusters approaches the band structure of the bulk system with increasing size. For instance in the case of gold, it was shown recently [35] that the transition from bulk to atom-like properties occurs between $33< n <100$.

For a detailed understanding of many phenomena involving clusters (e.g. catalytic activity) the geometry of the cluster is of great interest. However, for experiments alone it is almost impossible to deduce the exact shape of a cluster. To perform this task it needs a combination of experimental data and reliable calculations. One approach from the experimental side is the measurement of ion mobilities. The comparison of experimentally determined mobilities to calculated cluster mobilities allowed the determination of silicon [36] and carbon cluster [37] geometries up to medium sizes. Another method that proved to be very useful to determine equilibrium geometries is the photoelectron spectroscopy (PES). From PES measurements the electron affinity is available which can also be calculated using DFT.

In this chapter density functional theory will be applied to the investigation of bare gold clusters and hydrogenated gold clusters. In the first part of the study it will be demonstrated how DFT and PES can be combined to obtain structural information for clusters including two to six gold atoms.

Gold clusters recently attracted considerable interest for their unexpected catalytic activity [38]. It was shown that in contrast to the inert gold surface, nanoscale gold particles efficiently catalysed the oxidation of CO, with Au_8 as the smallest active cluster size. Furthermore aggregates of gold proved to be key components in nanotechnology [39].

Adsorption processes onto clusters - as the hydrogen adsorption on gold clusters discussed here- are of growing interest in the field of cluster physics. For example the adsorption of alkanethiol onto Au_{28} clusters allows the stabilisation of the gold core and makes the compound water-soluble [40]. Furthermore adsorbed gold clusters found application as tracers in biological molecules.

Recently, as a result of improved experimental methods, hydrogenation of gold clusters became possible despite the low reactivity of gold. The photoelectron spectra recorded by Stefan Burkart [41] at the University of Konstanz is taken as the reference for a large part of the theoretical analysis presented in this chapter. The class of hydrogenated clusters provides interesting information about the similarities and differences of hydrogen chemisorption on smaller particles and surfaces. In contrast to adsorption on a gold surface where molecular hydrogen is formed instantaneously [42], single hydrogen atoms chemisorb strongly to the cluster. So far, there is still a lack of understanding in the mechanism of adsorption of atoms and molecules to small gold particles. The nature of the Au-H binding in small cluster systems is not intuitive. Is it of metallic type as the other bonds in the cluster or is it rather covalent as the bonding of atomic hydrogen to a gold surface? This question as well as adsorption site preference and bond strength will be addressed in this chapter using *ab initio* methods.

Finally, the surprising results of the PES measurements that revealed a striking similarity in the vertical detachment energies of Au_n and $Au_{n-1}H$ will be discussed. These experimental findings call for a theoretical analysis to understand the influence of the replacement of a gold atom by a hydrogen atom on the electronic structure.

In summary the main goals of this study are the following:

- Determination of the structure of the Au_nH clusters observed in experiment
- Understanding of the adsorption process of hydrogen on small gold clusters
- Study of the effects due to the exchange of a gold atom by a hydrogen atom ($Au_n \leftrightarrow Au_{n-1}H$)

In the next section the computational details and the methods used to analyse the data are introduced. Before the extensive discussion of the hydrogenated clusters, a short overview is given on the results for bare gold clusters. In Section 3.3.2 the various Au_nH ($n \leq 6$) structures calculated and the corresponding energies are presented. These results will be compared (Section 3.3.3) to data from photoelectron spectroscopy. Hereby, it will be demonstrated how the structures found in the simulations can be assigned to features in the PES spectra. This is followed by a comparison of the properties of bare gold clusters to hydrogenated clusters. Finally, electronic and vibrational properties of Au_nH clusters are presented (Section 3.3.5 and 3.3.6).

To ensure high reliability of the results three exchange-correlation functionals were applied. This procedure allows to draw conclusion which are not biased by the choice of a particular functional. The performance of the different exchange-correlation functionals is discussed and the effect of including gradient corrections is explained.

Note that in a major part of the discussion the focus will be on the anionic clusters because these are the species that are actually detected in the experiment.

3.2 Methods

Density functional theory as described in Chapter 2 is applied with exchange correlation (xc) functionals in the local-density approximation (LDA [16, 17]) and including gradient corrections (BLYP [19, 20] and PBE [18]). For all functionals spin polarisation is included. The valence wavefunction is expanded in a plane wave basis set up to a kinetic energy cutoff of 50 Rydberg. As discussed in Section 2.6, the core-valence interaction is treated with pseudo potentials. In the case of gold it is crucial to include 11 electrons ($5d^{10}$ $6s^1$) in the valence because one-electron pseudo potential underestimated bond lengths by $\sim 25\%$ and bond strengths by $\sim 35\%$ [43]. For Au the norm-conserving, l-dependent, scalar relativistic pseudopotential was generated following the scheme of Troullier-Martins [26]. Note, that this pseudopotential takes relativistic effects as the contraction of the s-wavefunctions and the expansion of the d-wavefunctions into account. The ground state configuration ($d^{10}s^1$) was used for the s and d potentials, whereas $s^{0.75}p^{0.25}d^9$ was used for the p-potential. Core radii for the s, p and d components are 2.35, 2.35 and 1.5 Bohr, respectively. As the local part of the pseudopotential the s component was used. The Au pseudopotential was previously used in a study by Grönbeck *et al.* [43] where the structure of bare gold clusters was studied in the LDA and BLYP functional. For hydrogen the analytic potential according to Car and von Barth is used:

$$V(r) = \mathrm{erf}(r/r_c) + (a_l + b_l r^2)\exp[(r/r_{cl})^2] \tag{3.1}$$

where erf is the "error-function" defined by $\mathrm{erf}(x)=2/\sqrt{\pi}\int_0^x e^{-u^2}du$. The parameters were chosen to be a_l=-2.010249, b_l=0.496017, r_c=0.249841 and r_{cl}=0.279813 which allow a good fit to the all-electron wave functions. The calculation were performed using a cubic cell free of periodic boundary conditions [44] with an extension of 25 Bohr in each direction. Spin-orbit effects have been neglected in all calculations. However, it was argued [45, 46] that these effects are very small for Au_2 and Au_3.

The reliability of this computational approach was tested in comparing the DFT results to experimental data for AuH and Au_2. The numerical and experimental values for the bonding distance, the binding energy and the stretch vibration frequency are listed in Table 3.1. The bonding distances for AuH are in excellent agreement with experiment. For the gold dimer LDA performs best but PBE and BLYP are also in reasonable agreement. The binding energies E_B are well described by PBE and BLYP whereas LDA gives a value that is much too high. The overestimation of the binding energy is typical for LDA [48] and generally the use of gradient corrections in the xc-functional leads to a much better description of the binding, as also demonstrated in this case. The vibrational stretch frequencies are within 10% of experimental results for all xc-functionals.

Interestingly, the results for the dimers are very similar in the PBE and BLYP functional whereas the data for LDA differs significantly. Though LDA gives a better

	Au_2			AuH		
	d(Å)	E_B (eV)	$\omega(cm^{-1})$	d(Å)	E_B (eV)	$\omega(cm^{-1})$
PBE	2.54	2.27	173	1.55	3.12	2249
BLYP	2.56	2.12	173	1.55	3.15	2195
LDA	2.48	2.87	195	1.54	3.72	2223
Exp.	2.47	2.30	191	1.52	3.36	2305

Table 3.1: Characteristics of Au_2 and AuH. The bonding distance d, the binding energy E_B and the frequency of the vibrational stretch ω in the PBE, BLYP and LDA xc-functionals are compared to experimental data (Ref. [47]).

agreement with experiment in some cases, the introduction of gradient corrections leads to more reliable results since the strong overbinding is compensated. In the class of functionals including gradient corrections, the PBE functional gives slightly better results than the BLYP functional. Some portions of the analysis in Section 3.3 will therefore be only presented in terms of the PBE results.

The reported structures were optimised and converged to 1×10^{-4} Hartree/Bohr for the largest element of the gradient. It was shown in Ref. [49] that high spin multiplicity states are energetically unfavourable for bare gold clusters. Test calculations on higher spin multiplicity states resulted in isomers higher by 1 eV or more confirming these findings for hydrogenated clusters. For example, for the Au_4H^- clusters triplet states are at least 1.2 eV higher than singlets. The same applies for neutral and anionic Au_5H cluster with the triplet being 1.75 eV higher for the Au_5H(d) (see Fig. 3.3) structure and the quartet state being 1.4 eV higher than the doublet for Au_5H^-(a). For this reason only electron states of low spin multiplicity (singlets and doublets) have been considered.

For each cluster size ($n > 1$) the geometrical configurations of several isomers were optimised. Car-Parrinello molecular dynamics simulation [32] were performed to explore configurational space further and to investigate the probability of temperature-induced structural transformations. In these molecular dynamics simulations a time step of 0.12 fs and a fictitious electron mass μ of 500 atomic units was used.

For a comparison between theoretical and experimental data the vertical detachment energy (VDE) is used. Experimentally the VDE can be extracted from photoelectron spectra of the cluster anions. In a photodetachment spectra of anions each peak is assigned to a transition from the anionic electronic ground state to a transition to either the neutral ground state or one of the excited states of the neutral cluster. The detachment process is very fast compared with the vibrational motion, so that the geometry of the cluster remains unchanged. Therefore a vertical transition from the anionic state to the neutral state is observed (see Fig. 3.1). The transition energy is called the vertical detachment energy. Note that due to the fast detachment process the photoelectron spectra provides information about the neutral cluster in the geometry of the anionic cluster. The VDE is similar to the well known electron affinity, which is defined as the binding energy of an additional electron to the neutral particle [50]. However, the electron affinity can generally not be measured using a photodetachment experiment. It is only accessible in cases where the vibrational fine structure can be

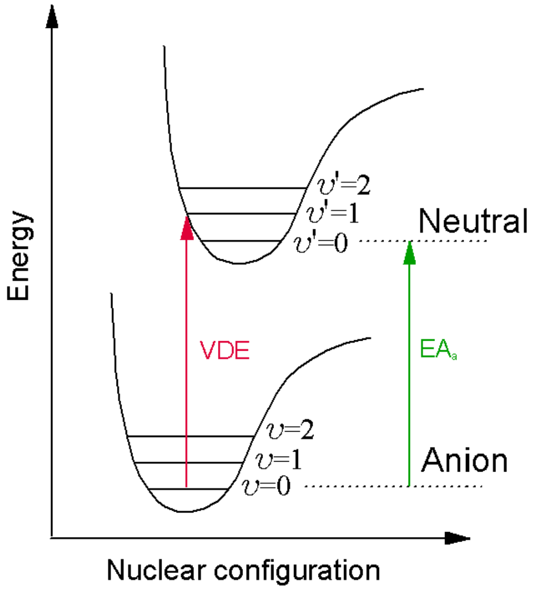

Figure 3.1: Illustration of vertical detachment energy (VDE) and adiabatic electron affinity (EA$_a$). The VDE corresponds to the transition from the ground state of the anion to the neutral cluster in the geometry of the anion. The EA$_a$ corresponds to a transition between the vibrational ground states ν'=0← ν=0. The VDE is always higher than the EA$_a$ unless the geometries in the anionic and neutral state are identical.

resolved in the spectra and the 0←0 transition can be identified (see Fig. 3.1). For some cluster types, e.g. small silicon clusters, the vibrational fine structure was determined experimentally but mostly it is not possible. In these cases only the VDE can be determined. In the DFT scheme the vertical detachment energy is computed as the difference in total energy of the anionic cluster and the neutral cluster in the geometry of the anionic cluster. The electron affinity (EA), on the other hand, is defined as the total energy difference of the neutral and the anionic species in their fully relaxed geometries.

The vibrational spectra presented in Section 3.3.6 were calculated using finite differences. Starting from the well-converged geometry corresponding to a minimum on the potential energy surface each atom was displaced by 0.01 Bohr in the x, y and z-direction and an optimisation of the wavefunction at fixed nuclear coordinates was performed. This procedure yields the energy and the forces on the nuclei. From this information the matrix of the second derivative of the energy (Hessian) can be calculated and derived from that, the eigenvectors and eigenfrequencies of the vibrations are accessible.

3.3 Results and Discussion

Before the discussion of the results for the hydrogenated gold cluster system the focus will be on the bare gold clusters. The equilibrium structures of neutral and anionic Au$_n$ with $n \leq 6$ are presented based on the calculations in the PBE functional. It will turn out later that the topology of neutral gold clusters is the key to match experimental

	$\Delta E(0)$	$\Delta E(-)$	EA$_a$	VDE	Exp.
Au_2	-	-	2.02	2.08	2.0
Au_3(a)	0.37	0	3.97	4.03	
Au_3(b)	0.02	1.58	2.04	2.10	3.9
Au_3(c)	0	-	-	-	
Au_4(a)	0.48	0	3.23	3.48	
Au_4(b)	0.05	0.06	2.74	2.79	2.8
Au_4(c)	0	0.13	2.56	2.63	
Au_4(d)	0.90	0.13	3.53	3.58	
Au_5(a)	0	0	3.06	3.10	
Au_5(b)	0.44	0.67	2.83	2.93	3.2
Au_5(c)	0.93	0.94	3.05	3.16	
Au_5(d)	0.85	1.19	2.73	3.04	
Au_6(a)	0	0	2.02	2.32	
Au_6(b)	0.48	0.18	2.57	2.63	
Au_6(c)	1.78	0.34	3.72	3.78	2.2
Au_6(d)	1.95	0.83	3.39	3.44	
Au_6(e)	1.07	-	-	-	
Au_6(f)	2.07	-	-	-	

Table 3.2: Bare gold clusters Au_n: Relative Energies (wrt. the ground state) ΔE(0) and ΔE(-) in eV, adiabatic electron affinities EA$_a$ and vertical detachment energies VDE. All energies are given in eV. The structures are ordered according to the stability of the anions (with Au_n(a) as the ground state). Experimental values for the VDE are taken from [41]. These structures will be referred to in the text as e.g. (4c) for Au_4(c).

data obtained for Au_nH to the numerical results. In addition structural characterisation is necessary in order to understand effects of hydrogen adsorption. The structure of small gold clusters was recently investigated by several groups [49, 51]. The following results can be considered to be an extension of Grönbecks and Andreonis work [49] to the PBE functional. In that study Au_n clusters ($n \leq 5$) were studied using the same pseudopotential as here, but in the LDA and BLYP functional.

3.3.1 Bare gold clusters

For each cluster size several isomers were considered and geometry optimisations were performed. The energetics for anionic and neutral clusters, the VDE and the electron affinity are compiled in Tab. 3.2, the corresponding geometries are shown in Fig. 3.2. The structures are ordered according to the stability of the anions. The experimental values for the VDEs are taken from S. Burkart's PhD thesis [41]. For small gold clusters the vertical detachment energy exhibits a strong odd/even-alternation. This phenomenon is reflected in the PES spectra in Fig. 3.5 for the cluster sizes n=3-8 but was reported to continue up to n=15 in Ref. [52]. Sizes with an even number of electrons have a much higher threshold energy than the clusters with an odd number of electrons. This phenomenon can be explained as a subshell closing, i.e. the pairing of two electrons.

For the gold trimers three geometries were considered: a linear cluster and two triangles with obtuse and acute shape. The equilateral triangle is unstable with respect to a Jahn-Teller distortion as expected for a three-electron system [53, 54]. Depending on which of the degenerate states of the highly symmetric structure is populated, the distortion is either to an obtuse or an acute triangle [49]. For the anions the linear configuration (3a) is clearly favoured. The triangles are either much higher in energy (3b) or even unstable (3c). The situation is completely different for the neutral trimers. Here, the triangles are nearly degenerate with the obtuse triangle slightly more stable. The linear cluster was found to be much higher in energy (ΔE=0.37 eV).

For Au_4 the situation is more ambiguous. PBE gives the zig-zag structure (4a) as anionic ground state but three other structures are within 0.13 eV. However, the VDE of the zig-zag structure is much too high compared to experiment (3.48 eV vs. 2.8 eV). It seems likely that the Y-structure (ΔE=0.06 eV) is the true ground state since its VDE (2.79 eV) matches the experiment much better, but the rhombus (ΔE=0.13 eV) is also a possible candidate (2.63 eV). In the neutral case the rhombus (4c) is lowest but this isomer is only separated by 0.05 eV from the Y-shaped structure (4b). As for the trimers the more open structures (4a) and (4d) show much lower stability. The anionic and neutral pentamer prefers clearly the most compact planar configuration (5a) which resembles a truncated triangle. This geometry is separated by more than 0.4 eV from the next higher planar structure (5b) which has the more open X-shaped geometry. Three-dimensional topologies are much less favourable. The distorted square pyramid

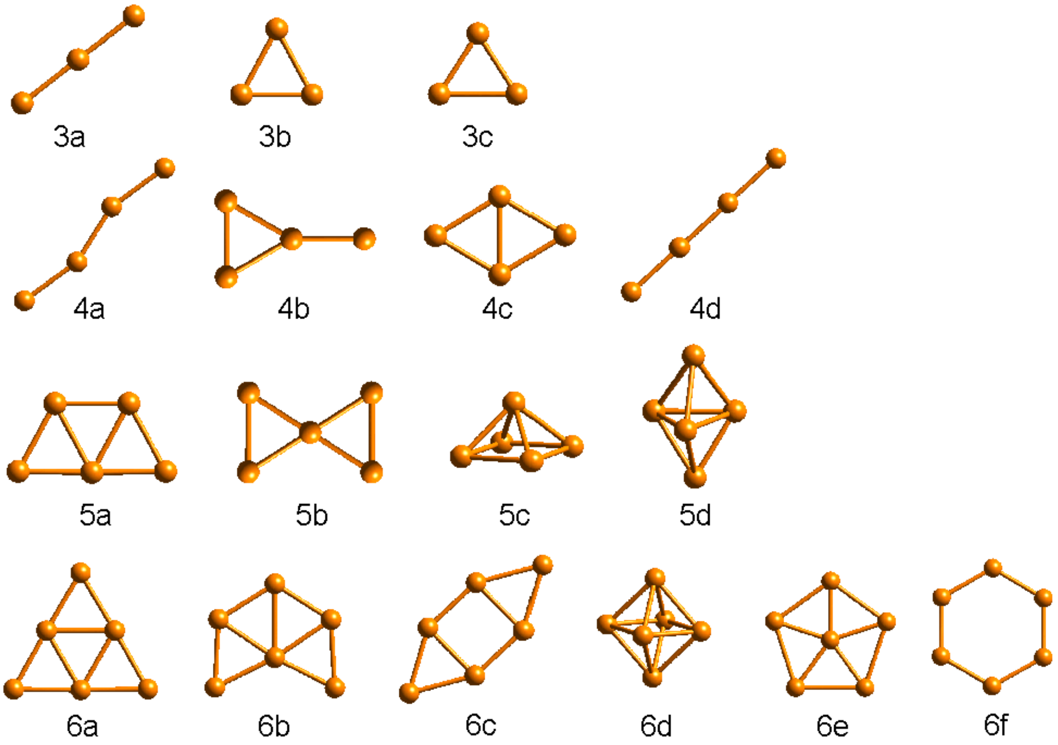

Figure 3.2: Optimised geometries for small anionic gold clusters Au_3^- to Au_6^- in the PBE functional. The structures are ordered according to their thermodynamical stability. The geometries of the neutral cluster are not significantly different.

(5c) and the distorted trigonal bi-pyramid (5d) are more than 0.8 eV higher in energy in the anionic and neutral state.

Also for Au_6 there is a clear structural preference. The triangular structure (6a) is favoured for the neutral and anionic species. It is separated by 0.48 eV respectively 0.18 eV from the next lowest-lying structure (6b) which can be considered as a distortion of the triangular reducing the symmetry to two-folded. All other structures including the three-dimensional square bi-pyramid are considerably higher in energy.

Interestingly, it was reported recently [55] that for anionic gold clusters the transition from two-dimensional to three-dimensional structures occurs at n=12. This is in clear contrast to the other noble metals, copper and silver, where the seven-atom cluster were found to be three-dimensional already [56].

More properties of gold clusters will be presented in the next sections when the comparison is drawn between bare and hydrogenated gold clusters. The electronic density of states of the bare anionic clusters can be found in Fig. 3.16. The cohesive energy of the neutral clusters is displayed in Fig. 3.21.

3.3.2 Structures and energetics of neutral and anionic Au_nH clusters

For the rest of the chapter the focus will be on the hydrogenated gold clusters. In order to obtain a complete picture of the physics and chemistry of the hydrogenated species, a large number of Au_nH structures in the size range from n=2-6 was taken into account in the simulations. In the search for local minima on the potential energy surface many isomers proved to be unstable and transformed into one of the stable geometries shown in Fig. 3.3. In this figure all isomers are shown which are stable in the neutral and anionic state or in either of them. The corresponding energies for the neutral and anionic species in the three xc-functionals (PBE, BLYP, LDA) and the values for the EA_a and the VDE are listed in Table 3.3. The structures are ordered according to the stability of the anions in the PBE functional. The isomers that are stable in the uncharged state only are added at the end of the list for each cluster size.

Anionic cluster

For Au_2H^- the linear configuration (2Ha) with the hydrogen atom at one end was found to be the most stable isomer for all xc-functionals. Structure (2Hb) with H bridging two gold atoms is more than 0.5 eV higher in energy and the triangular geometry (2Hc) is not stable.

Four configurations were found to be stable for Au_3H^-. The triangle with the hydrogen single-bonded to a gold atom (3Ha) is lowest in energy for PBE and LDA followed by the zig-zag-structure (3Hb) which is separated by 0.08 eV respectively 0.23 eV in PBE and LDA. In the BLYP functional there are three isomers within 0.1 eV with the zig-zag-like structure as the ground state geometry. This is a first example of the preference of this functional to favour more open (linear) structures.

In the case of Au_4H^- there is agreement for all three functionals. The most stable cluster for this size is a linear-type structure (4Ha) distorted by the hydrogen atom in bridge position (bonded to two Au atoms). This isomer is by far (0.24 eV in PBE) the thermodynamically most stable cluster. It is energetically well separated from structure (4Hb) that can be considered as a Y formed by the gold atoms plus the hydrogen forming a single bond to it and structure (4Hc) a gold rhombus with a hydrogen atom attached to it.

The calculations on Au_5H^- revealed that there are a number of isomers competing for the ground state geometry in PBE. There are three isomers within 0.01 eV and a total of six isomers within 0.11 eV. The reason for this is that most of the low-lying structure (except (5Hb)) are based on the favourable geometry for Au_5 (a truncated triangle). The same trend is observed for the results in LDA. The most favourable structure in PBE as well as LDA is the one (5Ha) where the hydrogen is bonded to a side atom in the base of the Au_5 core. In contrast to these findings BLYP prefers structure (5Hg) that consist of a gold triangle as the core with the three other atoms bonded to it.

Finally, the ground state structure for Au_6H^- is for all xc-functionals the bicapped square with the hydrogen in bridge position (6Ha). It is more than 0.1 eV lower in energy than isomer (6Hb) which is a gold triangle with the hydrogen in apex position. All other clusters are more than 0.3 eV separated from the equilibrium structure.

Neutral cluster

The analysis of the cluster geometries in the neutral state revealed interesting differences to the anionic clusters at some cluster sizes.

For the small Au_2H clusters the triangular cluster (2Hc) which was unstable in the anionic state is now the ground state for all xc-functionals. In BLYP it is almost degenerate with structure (2Ha) but it is clearly favoured for LDA and PBE ($\Delta E>0.1$ eV). This demonstrates again the difference between the xc-functionals: PBE and LDA show a similar preference whereas BLYP favours clearly the linear structures.

The same trend is apparent for Au_3H. Though the equilibrium geometry (3Ha) is the same for all functionals the energy differences are quite different depending on the xc-functional. In opposition to PBE and LDA which show a clear separation of the ground state ($\Delta E>0.2$ eV) to the next higher state (3Hb), these clusters are almost degenerate in BLYP.

For Au_4H the thermodynamically most stable structure is the rhombus with the hydrogen in bridge position (4Hg) for all xc-functionals. This is interesting because in none of the functionals this topology corresponds to a minimum for the anions. In the anionic case the structure relaxes to isomer (4Hc). The other isomers are considerably higher in energy in the PBE and LDA functional ($\Delta E>0.2$ eV) but in BLYP cluster (4Hb) is only 0.04 eV higher.

The favourite location of the hydrogen on the gold pentamer is clearly the bridge position (5He) leading to a configuration similar to the ground state of Au_6 with a gold atom replaced by the hydrogen atom. This is true for all functionals and other structures are more than 0.35 eV less favourable.

The ground state for Au_6H in PBE and LDA has a geometry (6Hi) that can be considered as a distortion of the anionic equilibrium structure (6Ha). It is only 0.02

	PBE				BLYP				LDA				Exp.
	ΔE(0)	ΔE(-)	EA_a	VDE	ΔE(0)	ΔE(-)	EA_a	VDE	ΔE(0)	ΔE(-)	EA_a	VDE	VDE
AuH	-	-	1.00	0.96	-	-	0.93	0.91	-	-	1.03	0.91	0.9
Au_2H(a)	0.11	0	3.30	3.31	0.02	0	3.24	3.26	0.16	0	3.56	3.58	3.6
Au_2H(b)	0.18	0.58	2.79	2.81	0.08	0.51	2.79	2.82	0.35	0.66	3.09	3.11	
Au_2H(c)	0	-	-	-	0	-	-	-	0	-	-	-	
Au_3H(a)	0	0	2.59	2.63	0	0.06	2.56	2.61	0	0	2.78	2.83	2.6
Au_3H(b)	0.22	0.08	2.73	3.01	0.06	0	2.67	2.97	0.30	0.23	2.85	3.20	
Au_3H(c)	0.86	0.16	3.30	3.33	0.68	0.08	3.21	3.27	1.07	0.34	3.52	3.56	
Au_3H(d)	0.86	0.79	2.66	2.74	0.95	0.93	2.64	2.73	0.77	0.69	2.87	2.93	
Au_4H(a)	0.37	0	4.00	4.01	0.09	0	3.92	3.94	0.71	0	4.29	4.31	3.2
Au_4H(b)	0.24	0.24	3.63	3.84	0.04	0.27	3.60	3.77	0.44	0.18	3.85	4.05	
Au_4H(c)	0.22	0.38	3.46	3.53	0.10	0.55	3.39	3.49	0.23	0.15	3.67	3.70	
Au_4H(d)	-	0.41	-	4.10	0.36	0.29	3.90	4.05	1.09	0.48	4.20	4.38	
Au_4H(e)	0.26	0.86	3.02	3.12	0.18	1.00	3.01	3.12	0.34	0.64	3.29	3.36	
Au_4H(f)	0.47	1.01	3.08	3.19	0.27	1.03	3.08	3.16	0.63	0.93	3.28	3.37	
Au_4H(g)	0	-	-	-	0	-	-	-	0	-	-	-	
Au_5H(a)	0.60	0	2.77	3.02	-	0.13	-	2.99	0.69	0	2.97	2.99	2.05
Au_5H(b)	1.08	0.01	3.18	3.22	0.85	0.07	3.13	3.20	1.34	0.24	3.38	3.43	
Au_5H(c)	-	0.01	-	2.71	-	0.13	-	2.68	-	0.01	-	2.88	
Au_5H(d)	0.43	0.09	2.52	2.64	0.37	0.21	2.50	2.67	0.47	0.08	2.67	2.80	
Au_5H(e)	0	0.10	2.08	2.21	0	0.29	2.06	2.24	0	0.18	2.10	2.24	
Au_5H(f)	-	0.11	-	3.22	-	0.09	-	3.18	-	0.27	-	3.37	
Au_5H(g)	-	0.15	-	3.50	0.79	0	3.14	3.45	-	0.46	-	3.68	
Au_5H(h)	0.52	0.19	2.51	2.65	-	0.27	-	2.35	-	0.14	-	2.82	
Au_5H(i)	1.54	0.20	3.51	3.68	1.13	0.01	3.47	3.63	-	0.66	-	3.94	
Au_5H(j)	-	0.43	-	2.91	-	0.58	-	2.86	0.89	0.36	2.81	3.10	
Au_5H(k)	1.79	0.47	3.50	3.78	1.26	0.17	3.45	3.71	2.39	0.98	3.69	3.97	
Au_5H(l)	0.68	0.50	2.34	2.81	0.46	0.53	2.29	2.57	0.89	0.56	2.57	3.25	
Au_6H(a)	0.02	0	3.46	3.50	0	0	3.41	3.47	0.10	0	3.82	3.83	3.6
Au_6H(b)	0.14	0.13	3.45	3.50	0.12	0.14	3.40	3.43	0.17	0.22	3.68	3.72	
Au_6H(c)	0.51	0.36	3.59	3.66	-	0.30	-	3.63	0.67	0.54	3.86	3.91	
Au_6H(d)	-	0.40	-	3.57	-	0.38	-	3.53	-	0.50	-	3.84	
Au_6H(e)	0.35	0.46	3.33	3.48	0.32	0.44	3.29	3.44	0.41	0.58	3.56	3.71	
Au_6H(f)	0.43	0.46	3.41	3.47	0.38	0.42	3.37	3.44	0.50	0.53	3.69	3.73	
Au_6H(g)	0.07	0.47	3.05	3.13	0.13	0.48	3.06	3.14	0.06	0.51	3.27	3.32	
Au_6H(h)	0.09	-	-	3.00	0.08	-	-	3.00	0.10	-	-	3.38	
Au_6H(i)	0	-	-	-	-	-	-	-	0	-	-	-	

Table 3.3: Hydrogenated gold clusters Au_nH: Relative Energies (wrt. the ground state) ΔE(0) and ΔE(-) in eV, adiabatic electron affinities EA_a and vertical detachment energies VDE in the PBE, BLYP and LDA functional. Structures are ordered according to the stability of the anions in the PBE functional (with Au_n(a) as the ground state). Experimental values for the VDE are taken from Ref. [41].These structures will be referred to as e.g. (4Hc) for Au_4H(c).

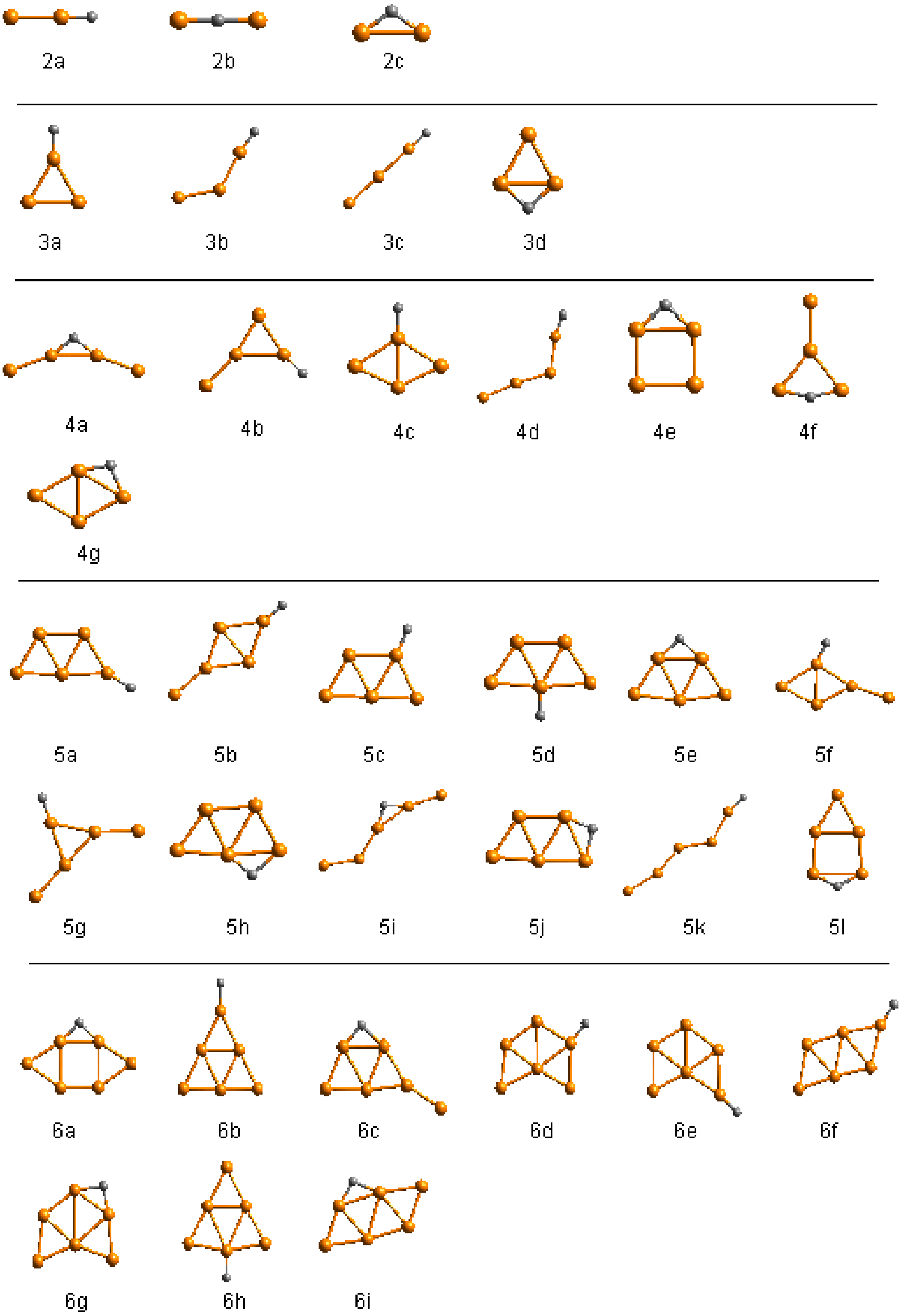

Figure 3.3: Optimised geometries of hydrogenated gold clusters Au_2H^- to Au_6H^- in the PBE functional. All geometries shown correspond to the anionic case except for isomers 2c, 4g and 6i, which are only stable in the neutral state. The structures are ordered according to their thermodynamical stability in the anionic state.

	Au-H	Au-H-Au	Au-Au	Au bulk
PBE	1.60	1.76	2.68	2.93
BLYP	1.58	1.75	2.71	3.00
LDA	1.57	1.72	2.61	2.87

Table 3.4: Bonding distances in Å as average over all neutral clusters. Comparison of the three functionals in terms of the single H-Au bonds, the H-Au bonds in bridge position, the Au-Au bonds (in the cluster) and the bond length in gold bulk.

eV (PBE) respectively 0.10 eV (LDA) lower in energy but it seems that the distortion further stabilises the cluster. In BLYP, though, the more symmetric structure (6Ha) is preferred whereas isomer (6Hi) is not stable.

Bond lengths in Au_nH and Au_n

In this section the structure of neutral Au_nH clusters will be analysed in terms of Au-Au and Au-H bond lengths. To obtain an overall picture the length of Au-Au and Au-H bonds was averaged over all stable cluster species. Since hydrogen can form single- and double-bonds to the gold clusters these bond lengths are listed separately in Tab. 3.4. As expected Au-H bond lengths depend on the choice of the xc-functional. The shortest bonds appear for LDA (1.57 Å) followed by BLYP (1.58 Å) and PBE (1.60 Å). Adsorption in bridge position (double-bond) leads to an increased bond length of $\sim$ 0.15 Å. Also here LDA gives the shortest and the PBE the longest bonding distances. This is quite surprising since usually properties in PBE lie between LDA and BLYP. In comparison to the AuH molecule the bond length increases by about 0.04 Å for all xc-functionals.

The length of Au-Au bonds in Au_nH clusters does not significantly change upon hydrogen adsorption for most clusters. However, the strength of the relaxation depends strongly on the isomer. For example the Au-Au bond in Au_2H is 0.05 Å longer than in Au_2. On the other hand, the hydrogen adsorption on the gold triangle and rhombus [(3a) and (4c) in Fig. 3.2] does not change the Au-Au bonds by more than 0.02 Å. Compared to Au in the bulk phase [43] the bond lengths are significantly shorter for microclusters. The contraction amounts to 0.25-0.29 Å depending on the functional what corresponds to a decrease of about 9%. Note, that there is no clear trend of increased Au-Au bond length going from Au_2H to Au_6H.

The effect of cluster ionisation on the bond lengths is studied in more detail in Fig. 3.4. For each cluster size one isomer is picked and the bond lengths of the neutral respectively anionic species are given. The configurations chosen are the ones which were determined to be present in the experiment according to the "parent-related" interpretation (see Section 3.3.3). The gold bonds of the neutral species range from 2.60 to 2.82 Å. The relaxation upon charging leads generally to an elongation of the bonding distances which can increase by up to 0.15 Å for some bonds. In the average of the five clusters there is a Au-Au bond elongation of 0.04 Å upon charging. There is also a slight lengthening of the Au-H bond apparent.

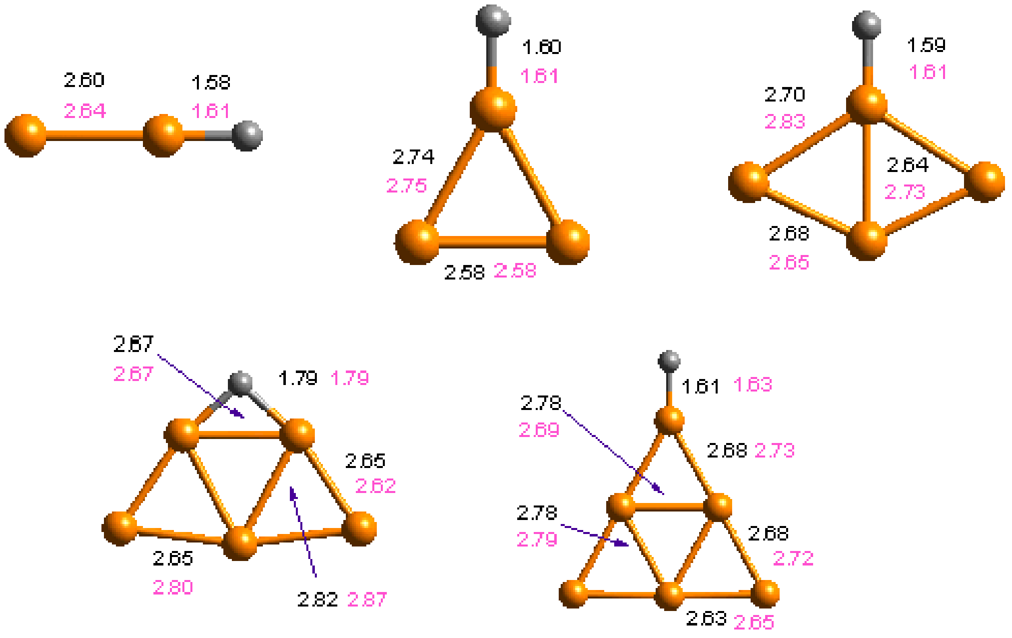

Figure 3.4: Bond lengths for Au_nH: The structures chosen are the ones which were determined to be present in the experiment according to the "parent-related" interpretation (see Section 3.3.3). The bond lengths (all in Å) in the PBE functional for the neutral clusters are in black and for the anionic in magenta. There is a tendency to increased bonding distances for the charged clusters.

Summary

In conclusion, LDA and PBE give the same ground state structures for all neutral and anionic clusters. The equilibrium structures for BLYP differ in several cases. Generally it seems that BLYP has the tendency to privilege the open structures (linear or zig-zag-like) too strongly. The search for structures corresponding to local minima on the potential energy surface revealed that hydrogen chemisorption on small gold clusters can take place at atomic (single-bonded) as well as bridge sites (double-bonded). The introduction of generalised gradient corrections (PBE and BLYP) leads to a shortening of Au-Au and Au-H bonds of the order of 2-4% with respect to LDA (no gradient corrections). Comparing the results of the neutral and anionic clusters there is a clear trend towards more open structures in the charged state. For example for n=2 and 4 the equilibrium structure changes from more compact to more open when an electron is added to the cluster.

3.3.3 Vertical detachment energies and structural assignment

The determination of cluster geometries is generally a difficult task and it demands the combination of experimental and theoretical data. Experiments can provide ion mobility measurement (e.g. [57, 58]), photoabsorption spectra (e.g. [59]), or, as in this study, photodetachment spectra. In the experiment performed in the group of Gerd Ganteför, anionic clusters were mass-separated before the extra electron of the anionic cluster was detached by means of a laser pulse. The measurement of the kinetic energy E_{kin} of the electron gives access to the binding energy E_{B}:

$$E_{\text{B}} = E_{\text{photon}} - E_{\text{kin}}(e^{-}) \,. \tag{3.2}$$

The first feature in the photodetachment spectrum is of particular interest because it defines the vertical detachment energy.

On the theoretical side the stability and the VDE (respectively EA) of a variety of isomers of a specific size can be computed using *ab initio* methods. The comparison of these two data sets gives insight in the structural properties of the clusters.

The results of the photodetachment experiments taken from Stefan Burkart's thesis [41] for Au_n^- and Au_nH^- are shown in Fig. 3.5. The experimental resolution is 0.1 eV with the exception of AuH^- where it is 0.25 eV. One can see that the VDEs of the bare and hydrogenated gold clusters exhibit a clear odd-even alternation. Surprisingly, the threshold energies of Au_nH and Au_{n+1} are in close accordance. This phenomenon, which suggests that a hydrogen atom behaves electronically like a gold atom in this chemical environment, will be discussed in detail in Section 3.3.4. Beforehand it is crucial to determine the isomers that were detected in the PES experiment on the base of the results presented in the preceding chapter. The following analysis uses mainly

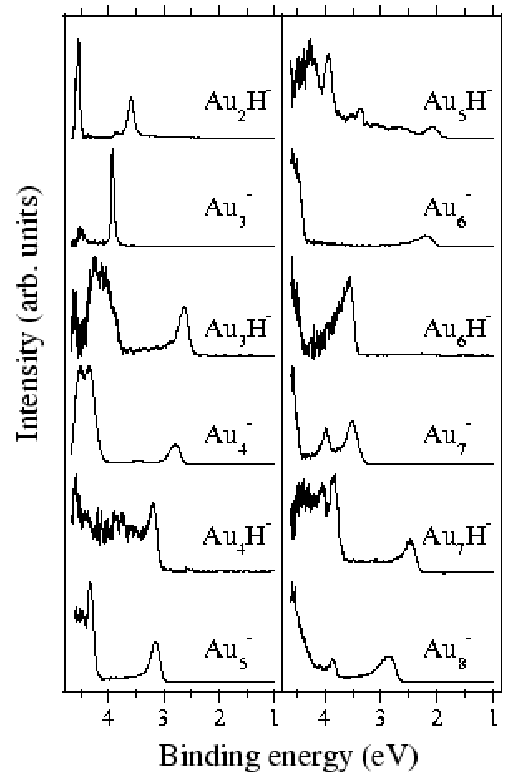

Figure 3.5: Photoelectron spectroscopy measurements of Au_n^- and $\text{Au}_{n-1}\text{H}^-$ recorded at a photon energy of 4.66 eV. The electronic structure of the clusters with the same number of atoms exhibit a strong similarity. The vertical detachment energy (VDE) is defined as the first feature in the spectra. The spectra are taken from [41].

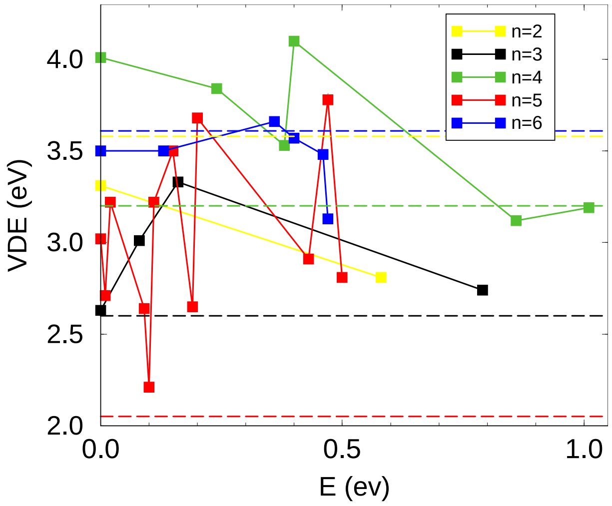

Figure 3.6: Calculated VDEs versus ΔE for Au_nH^- clusters in the PBE functional from n=2-6. The dashed lines correspond to the experimental VDEs. For n=2,3 and 6 the ground state isomer (ΔE=0 eV) is separated by less than 0.3 eV from the experimental value. For n=4 and 5 it deviates from experiment by more than 0.8 eV. For AuH (not shown) the calculated VDE of 0.96 eV agrees very well with experiment (0.9 eV).

the results in the PBE functional but it will be demonstrated that the conclusions do not depend on the choice of the functional.

The common approach to determine cluster geometries is, to compare the VDE of the ground state structure found in the simulations to the VDE measured in experiment. In this chapter this approach will be referred to as the “standard” interpretation. It is common for bare clusters and was successfully applied to several bare cluster systems (see e.g. [52, 60–63]).

In the system discussed in this chapter, the comparison between experimentally determined VDE and the VDE of the ground state structure shows very good agreement for AuH, Au_2H, Au_3H and Au_6H. This can be seen in Fig. 3.6 where the calculated VDEs (PBE functional) versus the energy difference to the ground state ΔE is shown. For the cluster sizes n=2,3 and 6 the ground state isomer (ΔE=0 eV) indicated on the left hand side of the figure is separated by less than 0.3 eV from the experimental value (dashed line).

The two stable isomers for Au_2H^- are separated by more than 0.5 eV and the VDE of the ground state (2Ha) is 3.31 eV compared to 3.6 eV from experiment. The VDE of the other stable structure diverges from the experimental value by $\sim$0.8 eV.

The assignment for the hydrogenated trimer is also clear: the lowest-lying isomer’s (3Ha) VDE is 2.63 eV which is in excellent agreement to the measured 2.6 eV. The VDEs of the other low-energy isomers are considerably higher (3.33 and 3.01 eV). The fourth isomer’s VDE is close to experiment (2.74 eV), however it is almost 0.8 eV higher in energy. A possible presence of this isomer will be discussed later in this section.

For Au_6H the VDE of a number of isomers match the experimental value. There are six isomers within an total energy difference of less than 0.5 eV relative to the ground state and all but one have a VDE that is close to experiment (3.6 eV). The

VDE of the two most stable isomers (separated by 0.13 eV) is identical (3.5 eV). The structural assignment for this cluster size will be made after the discussion for Au_4H and Au_5H.

In contrast to the cluster sizes discussed so far the application of the "standard" interpretation to Au_4H and Au_5H completely fails although more than 10 structures were considered for either sizes. The ground state structure for these cluster sizes give VDEs that are more than 0.8 eV too high in comparison to experiment (see also Fig. 3.6). These findings do not depend on the choice of the xc-functional. The same problem arises in the BLYP and LDA functional where the disagreement is 0.7-1.3 eV. The accuracy of DFT calculations is considerably higher than this discrepancy. Experience shows that VDEs can generally be determined to an accuracy better than 0.3 eV. There is in principle the possibility that an isomer whose VDE would fit the experiment value was not considered but in view of the large number of isomers taken into account this is very unlikely. It is remarkable that the two corresponding photoelectron detachment spectra are the only ones which exhibit numerous peaks. A deeper understanding of the formation process is necessary to explain the discrepancies in the VDE and the occurrence of several peaks in the PES measurement.

At this point it is helpful to have a look at the way the chemisorbed cluster systems are generated. In the PACIS (Pulsed Arc Cluster Ion Source) [50] the target material is eroded and then cooled down by interaction with He atoms (that are also ionised in the arc) so that gold clusters are built. Mostly neutral clusters are produced but a small fraction of the particles are charged. For materials like aluminium [64] the molecular hydrogen is added afterwards and clusters with one or more hydrogen atoms are generated. Because of golds low reactivity (it was not possible to produce Au_nH_2 clusters in a significant amount) the hydrogen is directly admixed to the helium and therefore it will be dissociated in the arc resulting in hydrogen anions and cations. At this stage the cluster temperature is estimated to be about 1000 K. Up to the time of the electron detachment the cluster is cooled down to roughly 300 K. Since the molecular hydrogen is dissociated in the arc into a hydrogen anion and cation it is very likely that the Au_nH^--clusters are a product of the reaction

$$\mathrm{Au}_n + \mathrm{H}^- \rightarrow \mathrm{Au}_n\mathrm{H}^- \, . \tag{3.3}$$

In this context the results have to be analysed in a completely different way. A closer look at Fig. 3.6 shows that for Au_4H^- and Au_5H^- there exists indeed an isomer that is based on the Au_n ground state structure *and* is in good agreement with the experimental VDE. The VDE of isomer (5He) is 2.21 eV compared to 2.05 eV, the VDE of structure (4Hc) is 3.53 eV in accordance with experiment (3.2 eV). This interpretation that considers isomers which are related to the equilibrium structure of Au_n ("parent") is hereafter called the "parent-related" interpretation. An analysis of the other cluster sizes n=2,3 and 6 shows that this interpretation is also valid for these cluster sizes. The ground state structures of Au_2H^- and Au_3H^- namely (2Ha) and (3Ha) do both consist of a hydrogen adsorbed to the Au_n (n=2,3) ground state. Therefore the two interpretations suggest the same isomer and it was already shown that these isomers agree well with PES data. For Au_6H^-, the ground state and the core-preserving structure are not the same. The former (6Ha) is a bicapped square with

H on a bridge position, the latter (6Hb) has the shape of a triangle with H at an apex site. However, their VDEs are the same. Thus, the "parent-related" interpretation gives excellent agreement for *all* cluster sizes.

In Fig. 3.7 the "parent-related" interpretation is compared to the "standard" interpretation. For all xc-functionals the "parent-related" interpretation provides an appropriate description of Au$_n$H clusters in contrast to the "standard" interpretation that fails the description at n=4 and 5. This demonstrates, that the success of the "parent-related" interpretation is not an artefact due to the use of a special xc-functional but it represent the intrinsic properties of the studied system.

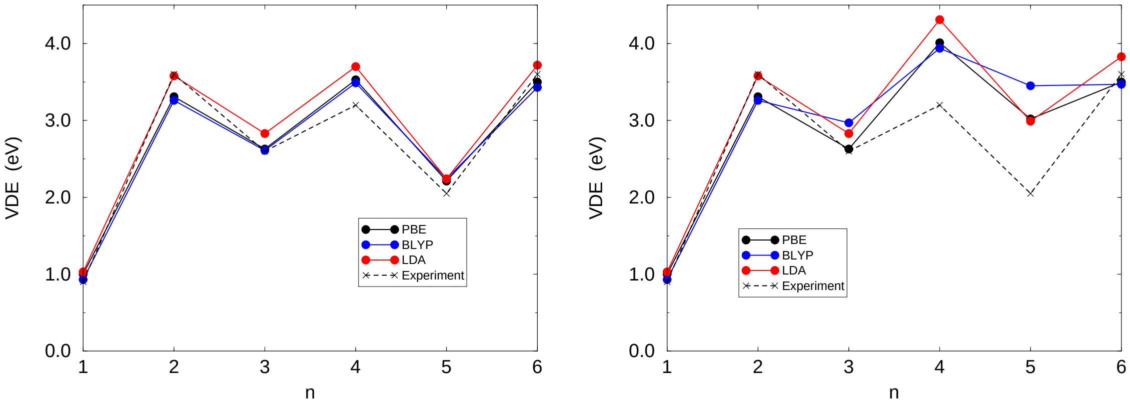

(a) "Parent-related" **(b)** "Standard"

Figure 3.7: Comparison of the "parent-related" interpretation (a) to the "standard" interpretation (b). The VDEs from experiment are indicated as dashed black lines. The VDEs in PBE, BLYP and LDA are in black, blue and red. Clearly, the agreement with experiment is excellent for the "parent-related" interpretation. In contrast the "standard" interpretation differs by $\sim$1 eV from experiment for some cluster sizes.

There is a valid argument in support of this interpretation. The preceding discussions suggest that when a H$^-$ hits a neutral gold cluster it binds strongly and the newly formed cluster has a low probability to transform to the ground state. The following results corroborate this picture.

Firstly, the formation energy of different channels resulting in a Au$_n$H$^-$ cluster was calculated (Fig. 3.8). The energy gain upon the reaction suggested in equation (3.3) is very high (4-5 eV for $n > 1$) and in particular it is much higher than the attachment of neutral atomic hydrogen to a Au$_n^-$ cluster or the attachment of an Au$^{(-)}$ monomer to a Au$_{n-1}$H$^{(-)}$ cluster where the adsorption energy is more than 1 eV smaller for all n. This proves the high probability of this formation channel and the strong binding of the hydrogen anion to the gold core.

Next, as mentioned above this interpretation implies that there exist high energy barriers for the transformation to the ground state. In order to deepen this idea, isomers of Au$_5$H$^-$ that originate from the Au$_5$ equilibrium structure are investigated in more detail. The geometry of Au$_5$ gives rise to six different Au$_5$H$^-$ isomers. All possible adsorption sites corresponded to local minima on the Born-Oppenheimer surface for

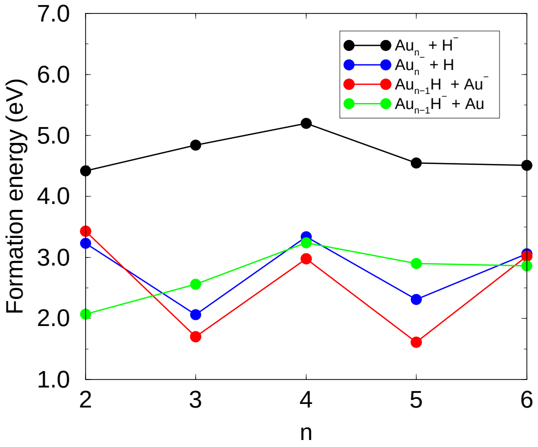

Figure 3.8: Four different formation channels for Au_nH^- (in PBE). Shown are the channels corresponding to the reaction with a neutral/anionic monomer of gold respectively hydrogen. The gain of energy upon reaction with the anionic hydrogen is by far the highest.

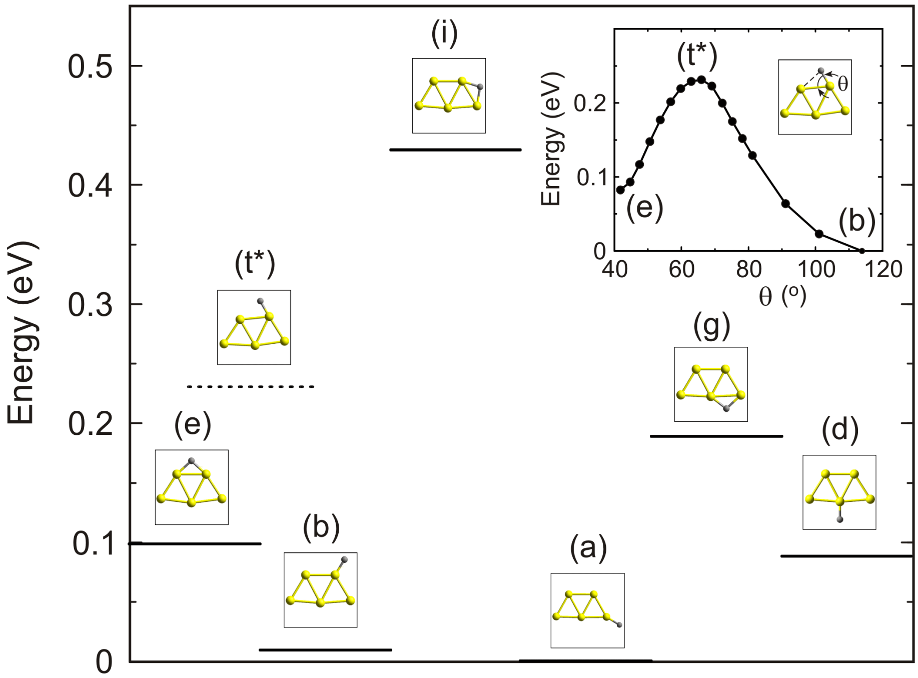

Figure 3.9: The total energies of Au_5H^- for different hydrogen adsorption sites in PBE. All configurations correspond to minima on the Born-Oppenheimer surface. In the inset the energy profile of the transition from (e) to (b) is shown. The calculated height of the barrier (0.13 eV) corresponds to a temperature of ~1800 K indicating a very low transition probability.

all xc-functionals. The six possible configurations and their energies according to PBE are shown in Fig. 3.9. Two isomers [(5Ha) and (5Hb)] are accidentally degenerate and compete for the ground-state structure. However their VDEs are more than 0.6 eV higher than the experimental value. The structure suggested by the "parent-related" interpretation is Au_5H^-(e). Its easiest isomerisation should end up to the (5Hb) isomer since this corresponds to the shortest hopping distance for H. Therefore the transition of interest here is the one from (5He) to (5Hb). The calculated energy profile as a function of the Au centred angle (reaction coordinate) is illustrated in the inset of Fig. 3.9. The transition of H from the bridge site (5He) through the transition state (t^*) to the atomic site (5Hb) implies an energy barrier of 0.13 eV corresponding to ~ 1800 K. This high transition barrier indicates that whenever a H^- hits a neutral cluster a strong Au-H bond is formed and the cluster gets trapped in this configuration. This was confirmed in consequent MD-simulations at 1000 K which revealed that the hydrogen atom remains stuck at the initial adsorption site for all six possible geometries. Remarkably, the gold core is heavily distorted while the length of the hydrogen bond does not change significantly.

Another question to address is, if it is possible that not only one but several isomers were detected in the experiment ("unselective" interpretation) and caused the manifold of peaks for some cluster sizes (n=4,5).

There is one example for this in the bare gold cluster system. For Au_4 besides the main signal at 2.7 eV a small peak at 3.4 eV can be spotted. These two peaks can probably be identified with different low-lying isomers ($\Delta E < 0.1$ eV) that were found in the geometry optimisations: the VDEs of isomers (4b) and (4c) is close to the peak at lower energy, the VDEs of isomers (4a) and (4d) are in agreement with the high-energy peak (see Tab. 3.2). The spectra of the other bare gold clusters (Fig. 3.5) do not show an additional peak or they are likely to be assigned to excited states. This is in accordance to our calculation where only for n=4 multiple isomers at low energy were observed. Therefore it seems probable that different isomers can occur in the cluster beam at a significant population if they are low enough in energy.

In the case of hydrogenated gold clusters a noticeable density in the PES spectra for Au_5H^- was observed in the 2.5-3.0 eV range what coincides with the VDE of three parent-related isomers. This idea can be further investigated by analysing the distribution of the electron localisation function (ELF [65–67]). It is defined as

$$\mathrm{ELF}(\mathbf{r}) = \frac{1}{[1 + (D(\mathbf{r})/D_0(\mathbf{r}))^2]} \tag{3.4}$$

where D is the difference between the positive definite local kinetic energy of a system of non-interacting fermions, $t_s(\mathbf{r})$, having the same density as the real system, and the von Weizsäcker kinetic energy density, $t_w(\mathbf{r})$,

$$D(\mathbf{r}) = t_s(\mathbf{r}) - t_w(\mathbf{r})\,, \tag{3.5}$$

where $t_w(\mathbf{r})$ is given by

$$t_w(\mathbf{r}) = 1/8|\nabla\rho(\mathbf{r})|^2\rho(\mathbf{r})\,. \tag{3.6}$$

D has the physical meaning of the excess local kinetic energy due to Pauli repulsion. In equation (3.4) D is put into context with the local kinetic energy of an homogenous electron gas D_0:

$$D_0 = 2.781\rho(\mathbf{r})^{5/3}\,. \tag{3.7}$$

Therefore, the ELF is a measure of the influence of the Pauli principle relative to a homogenous electron gas. In an illustrative picture, one can say that the lower the ELF values (they range from 0 to 1), the lower the charge accumulation, thus the greater the attraction centres for an H^-. The ELF of the parent Au_5 cluster is displayed in Fig. 3.10. It is uniformly distributed over the outside of the cluster and the three nonequivalent atomic sites are equivalent as attraction centres for an H^-, and bridge position are not significantly dissimilar.

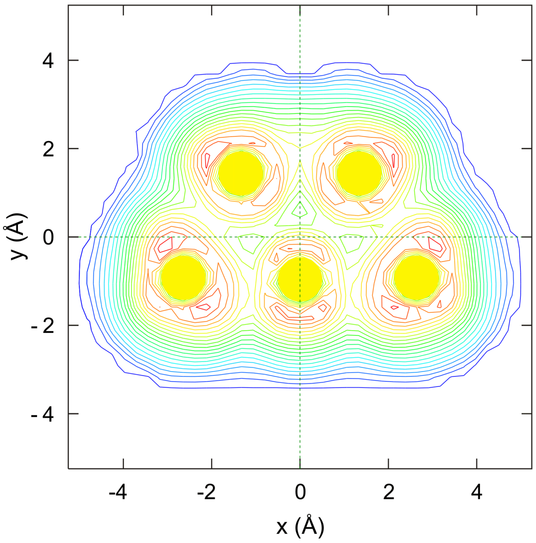

Figure 3.10: Contour plot of the electron localisation function (ELF) for Au_5. Values increase from 0.003 to 0.369 (with a spacing of 0.019) from blue to red. Low ELF values indicate low charge accumulation and thus attraction centres for H^-. The ELF is uniformly distributed over the outside of the cluster and the three nonequivalent atomic sites are equivalent as attraction centres for an H^-, and bridge position are not significantly dissimilar.

The following picture evolves from the discussion above: (i) there is no preferred adsorption site for the anionic hydrogen on Au_5 and (ii) high transition barriers prohibit the transition to lower-energy isomers. This means that the hydrogen is trapped at the site where it was originally adsorbed and the corresponding isomer gives finally rise to a signal in the photodetachment spectra explaining the multitude of signals for this cluster size.

The situation is slightly different for Au_4H^-. There are two low-lying structures for Au_4, the rhombus and the Y-structure. Only one of the possible Au_4H^- structure based on the rhombus is stable. This is isomer (4Hc) which is responsible for the first feature in the spectrum. Structure (4Hb) and (4Hf) are derived from the Y structure and are the only stable structures out of the six possible isomers. There is a strong intensity between 3.5 and 4.0 eV which agrees with the VDE of structure (4Ha) (3.84 eV). The stability of this isomer was checked in MD runs and it does not appear to undergo transformations up to 1000 K.

The spectra of the other cluster sizes (Fig.3.5) do not show additional peaks that could be interpreted as other isomers. This is in agreement with the data from the DFT calculations for n=2,3 and 6.

Both Au_2H^- and Au_6H^- have high-energy isomers [(2Hb) and (6Hg), respectively] with VDEs more than 0.5 eV lower than the experimental values but no intensity is observed at these energies. Au_2H^- with H bridging two gold atoms turned out to be very stable even at high temperatures. However, it is very unlikely that this cluster is formed from either Au_2 or AuH^-. The low-VDE isomer for Au_6H^- (g) transforms into (d) at $\sim$ 100 K. Note that many isomers of Au_6H^- have VDEs around 3.5 eV which is consistent with the shape of the peak in the PES spectrum.

For Au_3H^- the triangle as the ground state of Au_3 has to be considered. There are two possible adsorption sites on the triangle: the highly stable atomic site and the bridge site (ΔE=0.79 eV). The zig-zag-configuration Au_3H^-(c) which is only 0.08 eV higher in energy than the ground state dissociates a gold atom after less than 0.25 ns at 1000K. In contrast, the ground state Au_3H^-(a) remained stable over a period of half a nanosecond. The structure (3Hd) build from the Au_3 ground state, the triangle, with the hydrogen in bridge position has a barrier of only 0.01 eV to rearrange to isomer (3Ha) (Fig. 3.11) with the hydrogen at an atomic position. This explains why these structures do not contribute to the PES spectrum.

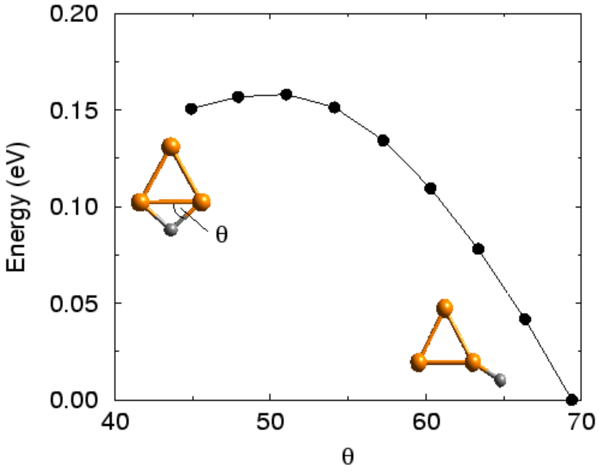

Figure 3.11: Energy profile for transition from Au_3H^-(d) to Au_3H^-(a) as a function of the reaction coordinate Θ which is defined as the Au centred angle. The energy barrier for hydrogen transition from bridge site to atomic site is only 0.01 eV.

The "parent-related" interpretation introduced is also consistent with the weak adiabatic effects for all cluster sizes noticeable in Fig. 3.5. This interpretation predicts Franck-Condon shifts of at most 0.3 eV in contrast to the thermodynamical interpretation that yields a strong size dependence and a shift of $\sim$0.8 eV for n=4 and 5.

At the end of this section some comments should be made on the different xc-functionals. As already discussed, the presented "parent-related" interpretation is not only valid in PBE (on which most of the discussion was based) but also for BLYP and LDA (Fig. 3.7). The findings are not an artefact caused by the choice of a specific functional. As shown in Tab. 3.3 the individual stability of the isomers depend on the functional but the conclusions are the same. BLYP prefers the more open structures, LDA the compact structures, whereas PBE's preference for structures is somewhere between BLYP and LDA. Concerning the VDEs in the xc-functionals there is also a trend observable. The VDE are in almost all cases (considering same structures) lowest in BLYP followed by PBE and LDA. On average the VDEs in PBE are about 0.05 eV and in LDA about 0.25 eV higher than in BLYP. Interestingly this does not apply for some Au_5H^- structures [(5Ha),(5He)] where almost no difference between the three functionals can be seen. The distribution of the differences in the VDEs between PBE and BLYP respectively PBE and LDA is shown in Fig. 3.12.

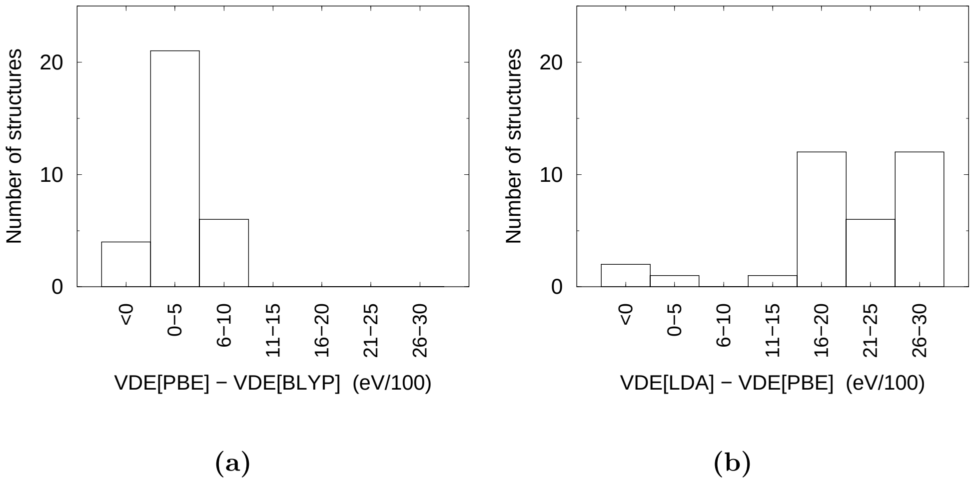

Figure 3.12: Comparison of the VDEs in the three functionals. The VDEs of all structures in Table 3.3 are considered and for each the difference in the vertical detachment energy between the different functionals is calculated. The histogram demonstrates that the VDEs for PBE are generally about 0.05 eV higher than in BLYP (see Fig. (a)) and around 0.25 eV lower than in LDA (see Fig. (b)).

3.3.4 How similar are Au_n and $Au_{n-1}H$?

The assignment of cluster isomers to the features in the photodetachment spectra presented in the preceding section makes it now possible to shed light on the surprising experimental results. As mentioned in the introduction, photoelectron spectroscopy revealed an evident similarity in the VDE between Au_n and $Au_{n-1}H$ for n >2 but it is not true for the dimers where the VDEs differ by 1 eV. Note, that in this section n indicates the total number of atoms in the cluster and not the number of gold atoms as in Section 3.3.1-3.3.3. This is because in the rest of the chapter often the properties of bare and hydrogenated gold clusters with the same number of atoms will be discussed.

The comparison of the experimental and calculated VDEs of the two cluster types are shown in Fig. 3.13. Most striking is the alternation in the VDEs for bare and hydrogenated species. Sizes with an even number of electrons have a much higher threshold energy than the clusters with an odd number of electrons. This phenomenon is typical for one-electron systems and can be understood in terms of a simple jellium model [34]. In this model it is assumed that one or more completely delocalized electrons per atom move in a spherical averaged potential of the positively charged cores.

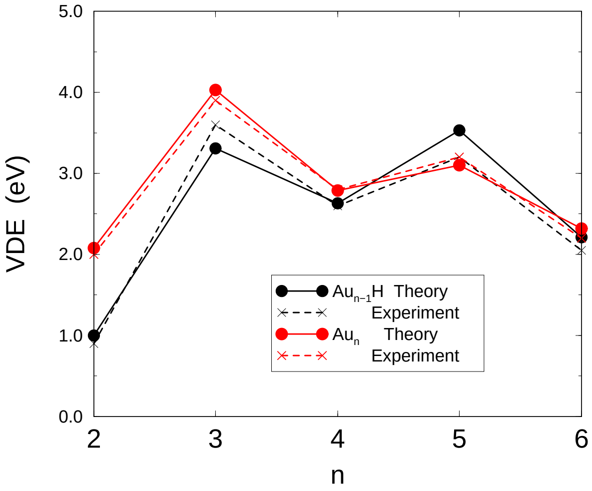

Figure 3.13: Overview of the measured and calculated VDEs for the bare (red) and hydrogenated (black) clusters. The experimental results are indicated by the dashed lines, the DFT results by the solid lines.

The energy levels of a system of non-interacting electrons in a model potential (e.g. Woods-Saxon potential) predict shell closings at certain number of electrons respectively cluster sizes (n=8,20,40,..). The jellium model is very successful for the alkalis where it predicts the experimentally observed [34] high stability of some cluster sizes which are due to these shell closing. However, following the Jahn-Teller-theorem the potential cannot be presumed to be spherical for clusters with partly filled shells. The Clemenger-Nilsson model [68] which is based on this theorem generalises the idea of the free electron gas to an elliptical potential.

In the case of gold, experiments [69] on a large size scale (n=2-70) revealed the validity of the shell model for $n \geq 8$ but the failure for small cluster sizes. This is not surprising since gold microclusters are planar and cannot be modelled as a sphere or an ellipsoid. The alternating VDEs observed at small cluster sizes is caused by a subshell closing, i.e. the pairing of two electrons.

The similarity between the VDEs of Au_n^- and $\mathrm{Au}_{n-1}\mathrm{H}^-$ is observed in experiment up to a cluster size of n=8. The maximum deviation occurs at n=3 where the VDEs differ by 0.3 eV. This is also the size with the worst agreement in the DFT results (Δ(VDE)=0.70 eV). The closest agreement is found for n=4 and 6 where both experiment (Δ(VDE)=0.2 eV and 0.15 eV) and theory (Δ(VDE)=0.16 eV and 0.11 eV) predict a strong similarity. Thus, the following analysis of the DFT results will focus on these cluster sizes though some analysis on the other cluster sizes will be presented as well.

There are three major questions to address:

- What effect has the cluster geometry on the similarity in the VDE ?
- Is a simple model valid that assumes that both atom types give one electron to the electron gas ?
- Does hydrogen behave like a gold atom in this chemical environment ?

Indeed a closer look at the cluster topologies immediately reveals interesting information. In Fig. 3.14 the ground state geometries of Au_n^- (for n=4 refer to the discussion in Section 3.3.2) are compared to the $Au_{n-1}H^-$ clusters according to the "parent-related" interpretation. There is an obvious structural similarity for n=3,4 and 6. For Au_2H^- and Au_3H^- the gold core remains almost unchanged. The structure (5He) suggested by the "parent-related" interpretation is the Au_5H^- isomer most similar to the Au_6^- ground state, but in opposition to Au_3H^- the hydrogen adsorption causes a strong relaxation in the gold core. At these cluster sizes the hydrogen replaces one gold atom in the cluster. For the pentamer the equivalent hydrogenated cluster would be the rhombus with the hydrogen in bridge position [(4Hg) in Fig. 3.3]. However, this structure is not stable in the anionic state in contrast to the case of the neutral clusters in which this isomer corresponds to the ground state. The discussion in this section does not include the seven-atom species but a few comments should be made. The VDE of the structure (6Hb) according to the "parent-related" interpretation is in very good agreement with the experimental value for Au_7^- (3.5 eV). The geometry of Au_7^- was very recently reported [56] to be an edge-capped square with a VDE of 3.46 eV. This geometry is similar to structure (6Hg) whose VDE is 3.13 eV.

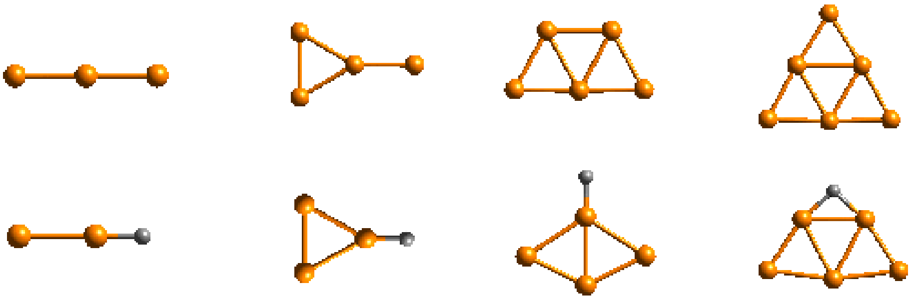

Figure 3.14: Structural comparison of Au_n^- and $Au_{n-1}H^-$ clusters. The thermodynamically most stable isomers are shown for Au_n^- (see comment on Au_4^- in the text) and the isomers according to the "parent-related" interpretation are given for the hydrogenated species.

The distribution of the VDEs of the other isomers gives further insight in the problem. The VDE of most of the isomers are not compatible with the bare clusters VDE. In almost all cases the calculated VDEs are higher than the experimental VDEs:

- n=3: The other stable trimer with hydrogen between the two gold atoms is much too high in VDE.
- n=4: The VDE of structure (3Hd) is close to experiment but it transforms into isomer (3Ha) immediately (see Fig.3.11).
- n=5: Besides (4Hb) there is only structure (4Hc) with a compatible VDE.
- n=6: All structures except (5Hd) are more than 0.5 eV too high in the VDE compared to Au_6.
- n=7: Many structures with compatible VDEs. All those structures are compact. The more open structure (6Hc) is about 0.3 eV higher. There is one structure

(6Hg) with low VDE but that transforms into isomer (6Hd) in molecular dynamics runs.

In conclusion, in most cases only those hydrogenated clusters that are structurally related to the bare clusters of the corresponding size are similar to the gold clusters in terms of the VDE. Topological considerations can provide some information but real understanding of the phenomenon demands for the investigation of electronic properties.

Considering the experimental results one is tempted to conclude at first sight that both atom types give one electron to a common electron gas as in the jellium model. This idea can easily be checked by analysing the electron transfer in the system upon formation of the bonds. To gain insight in the bonding of Au_nH clusters the difference in the density $\Delta\rho_{\mathrm{bond}}$ between the cluster and the sum of the neutral isolated atoms at their position in the cluster was calculated. In this way charge accumulation and depletion can be analysed. As an example structure (5He) in its neutral state was considered. In order to obtain the difference in the density according to

$$\Delta\rho_{\mathrm{bond}}(\mathrm{Au_5H}) = \rho(\mathrm{Au_5H}) - [\rho(\mathrm{H}) + \rho(\mathrm{Au}^1) + ... + \rho(\mathrm{Au}^5)] \tag{3.8}$$

the electronic density of the cluster, an isolated hydrogen atom and an isolated gold atom had to be calculated. In equation (3.8) $\rho(\mathrm{Au}^m)$ stands for the electronic density of the gold atom with the number m in its cluster position which was received by shifting the density of the isolated gold atom to that position. The result of this procedure is displayed in Fig. 3.15 where isosurfaces of depleted and accumulated regions are depicted. The blue region located around the hydrogen atoms indicates a clear charge transfer to the hydrogen whereas charge depletion (red isosurface) occurs around the neighbouring gold atoms. The depleted orbitals at the gold atoms are of p character. This result is in agreement with the very high (13.6 eV) ionisation potential of hydrogen which hampers charge transfer away from hydrogen. The plot at a lower isosurface value (on the left) shows additional charge between the gold atoms where the bonds are formed. A further analysis of the electron population revealed a net charge excess of $\sim$0.1 e on the hydrogen atom. These findings make clear that the hydrogen atom does definitely not act like a metallic atom in the sense of the jellium model.

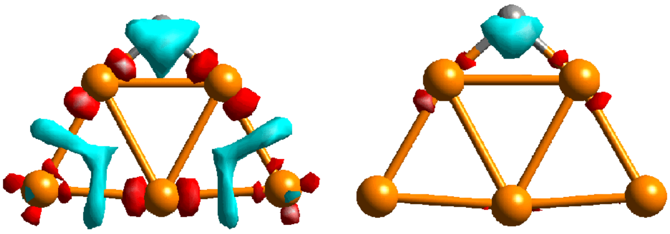

Figure 3.15: Plots of the difference in charge density between the Au_5H(e) cluster and the sum of the neutral atoms at their position in the cluster. On the left (right) a low (high) value for the isosurface of the charge density was chosen. Red indicates regions of charge depletion, blue stands for charge accumulation.

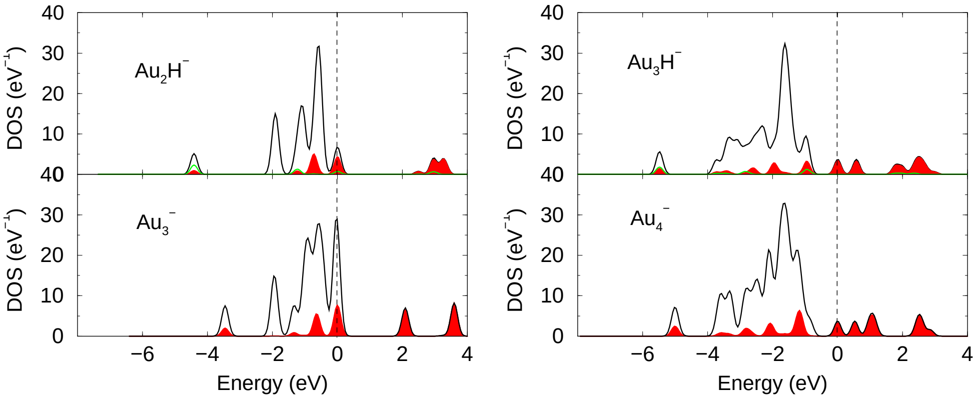

(a) 3 atoms **(b)** 4 atoms

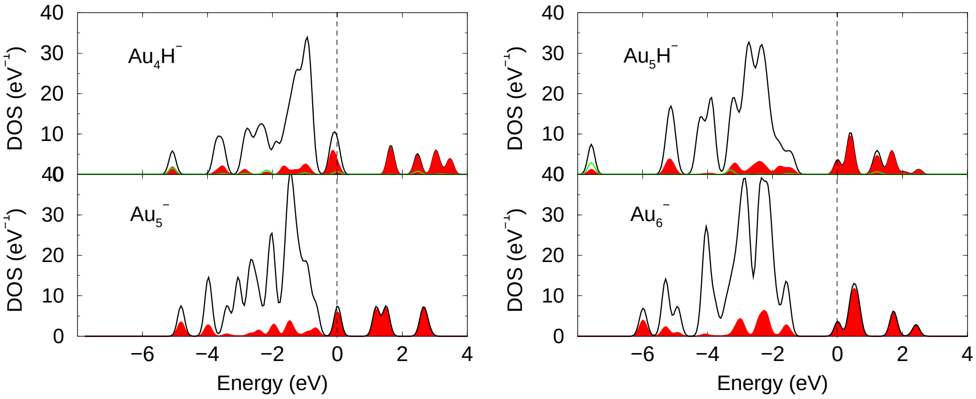

(c) 5 atoms **(d)** 6 atoms

Figure 3.16: The electronic density of states (EDOS) for the clusters shown in Fig. 3.14. The projection of the EDOS on the *sp*-states is in red, the projection on the hydrogen is in green. The spectra are shifted such that the highest occupied molecular orbital (HOMO) resides at 0 eV. The states at positive energies are unoccupied. The one-electron Kohn-Sham levels were broadened with a 0.1-eV Gaussian.

To get further insight into the electronic properties of bare and hydrogenated clusters the electronic density of states (EDOS) was calculated. In Fig. 3.16 the density of states is plotted for the structures shown in Fig. 3.14. Additionally the projection on the *sp*-states as well as on the hydrogen atom is shown. The spectra are shifted such that the highest occupied molecular orbital (HOMO) resides at 0 eV. The hydrogenated clusters have in common that the lowest-lying state is separated by 1.5-2.5 eV from the *d*-band which dominates the spectra. On this state most of the hydrogen wavefunction is localised. This underlines the strong bonding of the hydrogen to the gold cluster. The contribution of the hydrogen atom to the DOS is not delocalised as would be expected by a gold atom but rather localised on the lowest state. These findings indicate that the Au-H bond is of covalent type. Hence, the hydrogen atom does not act like a gold atom but is special in its character. For this reason the similarities in the VDE between Au_n^- and $Au_{n-1}H^-$ cannot be explained by the assumption that the hydrogen gives an electron to the sea of the delocalised electrons in analogy to the jellium model. Interestingly for all four- and six-atom cluster (those which have an unpaired electron in the HOMO) the HOMO is completely of *sp* character indicating a possible similarity of the bare and hydrogenated clusters at these sizes. This is not true for n=3 and 5 where the *sp* contributions to the HOMO are different for bare and hydrogenated species. The HOMO-LUMO (lowest unoccupied molecular orbital) gap is much larger for the odd-numbered clusters (Au_3^-, Au_5^-, Au_2H^-, Au_4H^-). It has almost identical size for Au_3H^- and Au_4^- respectively Au_5H^- and Au_6^-. The size of this gap may be one of the key features, clusters with a small difference in the VDE have in common. This idea is supported by the fact, that this gap is not present for $Au_5H(d)^-$ (not shown) where the VDE does not match the value of the bare gold cluster. The size of the HOMO-LUMO gaps will be discussed in more detail in Section 3.3.5. Finally, note that the unoccupied states are of *sp* character for all studied clusters.

For a detailed understanding of the similarities in the VDE the fate of the detached electron has to be addressed. In order to obtain more information about the detachment process the anionic state and the “VDE state” (neutral cluster in the geometry of the anion) have to be pulled together. The DOS of the “VDE state” is confronted with the anionic state in Fig. 3.17 for the case of the six-atom cluster. Neither the bare cluster nor the hydrogenated structure manifest significant changes in the shape of the DOS upon electron detachment. This is due to the unpaired electron in the HOMO at this cluster size and it is removed with little perturbation of the other electronic states. However, electron detachment causes a shift of roughly 1.8 eV of the DOS to higher energies (where the highest state is defined to reside at 0 eV). The gap between the HOMO and the *d*-band is reduced strongly after the electron detachment. But still, it is not clear what the origin of the surprising similarity in the VDEs is.

The property of importance when analysing electron detachment is the electronic difference between the anionic state in its equilibrium geometry and the neutral state in the same geometry. It is very instructive to have a look at the location of the detached electron and to check what type of orbital is related to it. In a simple approximation one can calculate the difference of the electronic density between these two states: $\Delta\rho = \rho(\text{Anion})\text{-}\rho(\text{Neutral})$. Note, that the integral over $\Delta\rho$ is always equal to one for this case.

In Fig. 3.18 $\Delta\rho$ is displayed for the three- and five-atom species for which the agreement in the VDEs in DFT is rather bad compared to n=4 and 6. The figure shows isosurfaces for regions with charge depletion (blue) and charge accumulation (red) upon electron detachment. On the top row Au_3^- and Au_2H^- are shown. One would expect from the similar topology of these clusters that some resemblance occurs, however the distribution of $\Delta\rho$ is completely different. For Au_3^- the extra electron is equally distributed over the gold atoms following the symmetry of the cluster. The replacement of a gold atom by a hydrogen atom leads to a breaking of the symmetry. The isosurface of $\Delta\rho$ on the left gold atom is ringlike, the $\Delta\rho$ on the right atom (H) is of *s*-type, both in contrast to Au_3^-. In the case of the five-atom clusters the geometries of the bare and hydrogenated species are not very closely related. Therefore, it is

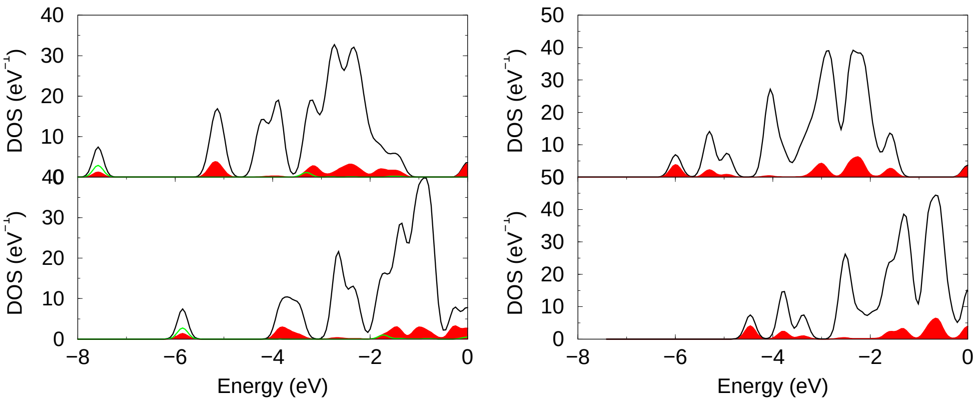

(a) Au$_5$H$^-$(c) **(b)** Au$_6^-$(a)

Figure 3.17: EDOS of Au$_5$H$^-$(e) and Au$_6^-$(a) before (top) and after (bottom) electron detachment. The projection of the EDOS on the *sp*-states is in red, the projection on the hydrogen is in green. The spectra are shifted such, that the highest occupied molecular orbital (HOMO) resides at 0 eV. The one-electron Kohn-Sham levels were broadened with a 0.1-eV Gaussian.

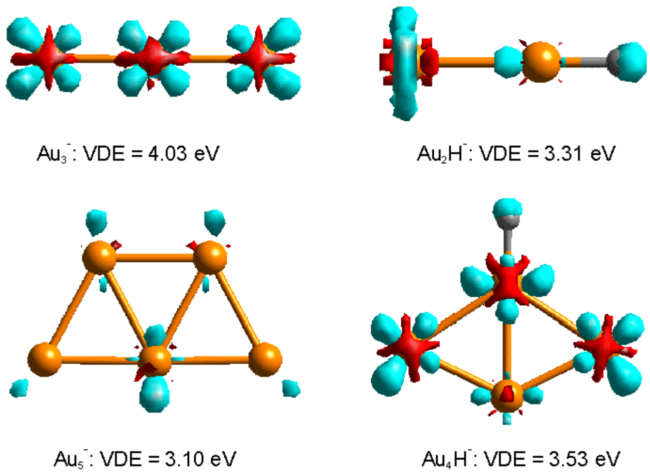

Figure 3.18: $\Delta\rho$ for the three- and five-atom species. On the left the bare clusters, on the right the hydrogenated clusters. Isosurfaces are shown for regions with charge depletion (blue) and charge accumulation (red). The integral over $\Delta\rho$ is equal to one. The isosurface values chosen are ± 0.005 e/Bohr^3 for n=3 and n=5.

not surprising that the distribution of $\Delta\rho$ differs significantly. The isosurface of the depleted charge reveals that the extra electron is mainly located in a *d*-like orbital on the central base atom of Au$_5^-$. For Au$_4$H$^-$ the $\Delta\rho$ is localised on the hydrogen atom and the upper three gold atoms.

This analysis demonstrates that for these cluster sizes bare and hydrogenated gold clusters are electronically dissimilar. The reasonable accordance of the VDEs found in experiment is fairly reproduced by DFT calculations but the deeper electronic analysis does not provide support to the idea that hydrogen acts as a gold atom.

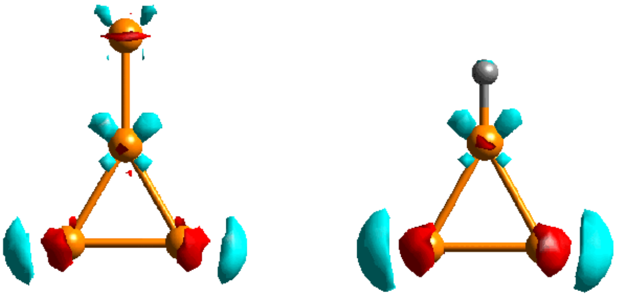

Au$_4^-$: VDE = 2.79 eV Au$_3$H$^-$: VDE = 2.63 eV

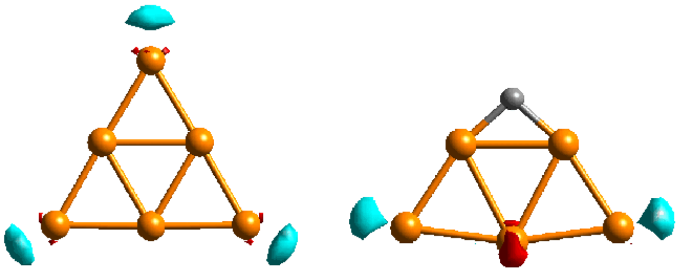

Au$_6^-$: VDE = 2.32 eV Au$_5$H$^-$: VDE = 2.21 eV

Figure 3.19: $\Delta\rho$ for the four- and six-atom species. On the left the bare clusters, on the right the hydrogenated clusters. Isosurfaces are shown for regions with charge depletion (blue) and charge accumulation (red). The isosurface values chosen are $\pm$ 0.0035 e/Bohr^3 for n=3 and 5.

The most promising candidates to understand the experimental results are the four and six-atom clusters. The $\Delta\rho$ of these clusters is given in Fig. 3.19. In opposition to the clusters discussed above there are clear similarities observable. For the clusters containing four atoms the exchange of the gold atom in the Y shaped gold cluster by a hydrogen does only slightly alter the distribution of $\Delta\rho$. This is because almost no density is located at these atoms. In Au$_4^-$ as well as Au$_3$H$^-$ most of the density is on the lower two gold atoms and some density in the shape of d orbitals is on the central gold atom. This means that the nature of the detached electron is very similar despite the fact that the stoichiometry of the cluster is different. These two clusters are electronically very closely related to each other and for this reason it is not surprising that the VDEs calculated in DFT differ only by 0.16 eV. The situation is comparable for Au$_6^-$ and Au$_5$H$^-$. The character of the $\Delta\rho$ distribution is the same for both clusters. The electron that is detached sits on the corners of the clusters with the difference that no density is observed on the hydrogen. In addition the shape of the densities is alike.

Motivated by the preceding results a deeper analysis at the cluster sizes n=4 and 6 was undertaken. So far only the difference of the electronic density caused by the detachment process was considered. To get access to the associated wavefunction a more sophisticated approach is needed. In the local spin density approximation (one electron per state) the number of states is $m + 1$ for the anion and m for the neutral cluster. Step one is to calculate the m Wannier orbitals of the “VDE state” what corresponds to a projection of the Kohn-Sham orbitals onto the atomic orbitals. To bring both systems to the same number of electrons an additional state is introduced (number $m+1$) and set to a constant. In the second step, the $m+1$ orbitals of the anionic state are rotated using unitary transformations in such a way that the overlap with the constructed "VDE state" is maximal. Then, per construction the lower m electronic states of the anionic cluster are identical (to be more precise: identical in the sense that optimal overlap was achieved) to those of the "VDE state". The wavefunction of the $m+1$th orbital (the additional electron) of the anionic state can then be interpreted as the wavefunction of the detached electron. Isosurfaces of the wavefunctions obtained in this way are given in Fig. 3.20.

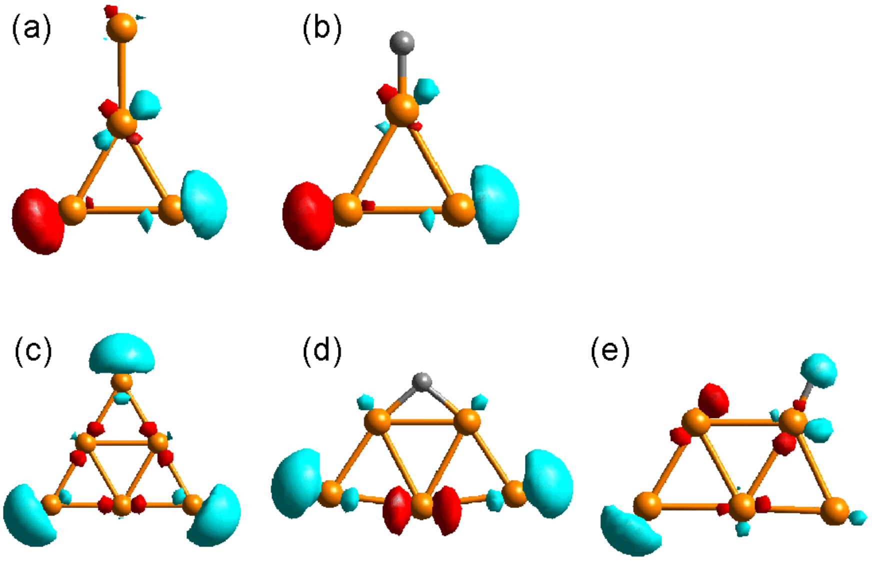

Figure 3.20: Wavefunction of the detached electron for the sizes n=4 (a,b) and 6 (c,d,e). The procedure explained in the text was applied to those clusters. Blue and red stand for isosurfaces with positive respectively negative value. The values are chosen such that the nature of the wavefunction becomes most evident. The same conclusion as for the analysis of the $\Delta\rho$ arise. Structure (e) (VDE=2.71 eV) is shown to illustrate the importance of similar geometries between Au_n^- and $\mathrm{Au}_{n-1}\mathrm{H}^-$. Here, the wavefunction of the detached electron is completely different from Au_6^-.

The analysis of the wavefunction of the detached electron reveals a picture similar to the one obtained on the base of $\Delta\rho$. The localisation of the state of the detached electron gives the answer why the VDE of $\mathrm{Au}_3\mathrm{H}^-$(2.63 eV) and Au_4^-(2.79 eV) are so similar (Fig. 3.20(a) and (b)). The wavefunction is located mainly on the bottom two gold atoms for both, the bare *and* the hydrogenated system. There is no contribution from the top gold atom and neither from the hydrogen atom. Furthermore, the symmetry of the wavefunction is identical. For this reason the VDE is not altered significantly when the gold atom is replaced by a hydrogen.

The situation for the six-atom cluster is slightly different. Also here the symmetry is the same if the "parent-related isomer" is considered, however the bulk of the wavefunction is distributed uniformly on the three atoms at the corner of the Au_6^-

cluster, whereas no wavefunction appears on the hydrogen atom of Au_5H^-(e) (Fig. 3.20(c) and (d)). Nevertheless the VDEs are very close (2.32 eV (bare) and 2.21 eV (hydrogenated)). To illustrate in which way the cluster geometry effects the VDE an additional six-atom isomer (5Hc) was considered which has the same geometry as the one according to the "parent-related" interpretation (5He) but the hydrogen atom is not in bridge but in the neighbouring atomic site. However, its VDE (2.71 eV) is far away from the experimental value (2.05 eV). The wavefunction of the detached electron shows clearly the reason for this disagreement (Fig. 3.20(e)). Due to the different adsorption site the symmetry of the cluster changes and thus the wavefunction is completely different from the bare gold cluster.

In this section the surprising similarity in the vertical detachment energies between Au_n^- and $Au_{n-1}H^-$ was discussed. In the first part the importance of structural resemblance between bare gold clusters and hydrogenated clusters was outlined. An investigation of the charge transfer in the system demonstrated that the hydrogen atom attracts electrons from the gold atoms rather than donating its electron to a common electron gas. Therefore the idea of a metallic hydrogen in Au_nH clusters is not valid. For the cluster sizes with the most similar geometries the analysis of the wavefunction of the detached electron revealed a striking resemblance explaining the match in the VDE.

3.3.5 Electronic properties

In the preceding sections a series of electronic properties was already studied. Different formation channels of Au_nH^- were discussed in Section 3.3.3 and displayed in Fig. 3.8. The electronic density of states of Au_n^- and Au_nH^- clusters (Fig. 3.16) was of interest in the previous section. The nature of the hydrogen adsorption on small gold clusters was presented in Fig. 3.15 in terms of charge transfer. In this section the focus will be on other properties like the cohesive energy, the strength of the Au-H bond and the size of the HOMO-LUMO gap.

The cohesive energy gives information on the strength of the chemical bonds in the cluster as a whole. For a Au_nH cluster it is defined as (total energies of the clusters are negative corresponding to a bonded state)

$$E_{\mathrm{coh}} = -\left[\frac{1}{n+1}\left(E(\mathrm{Au_nH}) - \{\mathrm{n}\cdot\mathrm{E(Au)} + \mathrm{E(H)}\}\right)\right] \tag{3.9}$$

and thus equal to the binding energy per atom. The cohesive energies of the homogeneous and heterogeneous clusters in their neutral state are displayed in Fig. 3.21 as a function of the number of atoms for the three xc-functionals. For the bare gold clusters E_{coh} increases from n=2 to 6 with the exception of BLYP which predicts a slightly lower cohesive energy for the trimer than for the dimer. This dip in the curve at n=3 (corresponding to Au_2H) is also present for the hydrogenated species for all functionals. Apart from this, there is also a decrease in the cohesive energy present when going from Au_5H to Au_6H. Interestingly, the replacement of a gold atom by a hydrogen atom leads to a stabilisation of the cluster. The cohesive energy is higher for Au_nH compared to Au_n for all cluster sizes (except n=5 in LDA). This is especially

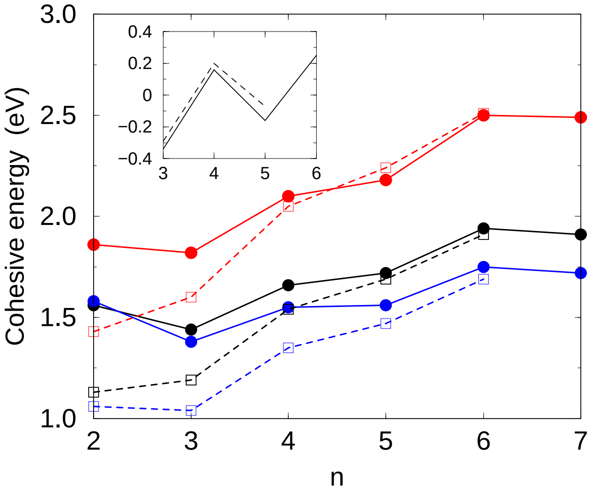

Figure 3.21: Cohesive energies for $Au_{n-1}H$ (solid lines, filled circles) and Au_n (dashed lines, open squares) in the three functionals: LDA (red), PBE (black) and BLYP (blue). All energies are calculated using the ground state energies. The cohesive energy of the hydrogenated cluster is higher for all cluster sizes in PBE and BLYP. Cohesive energies are about 0.5 eV higher in LDA and 0.1 eV lower in BLYP in comparison to PBE. In the inset the second derivative of the energy is plotted (only PBE). Pronounced maxima for n=4 and 6 indicate high stability for these cluster sizes.

striking for the dimers and trimers, where the substitution of a gold atom by a hydrogen atom leads to an enhanced bonding in the order of 0.2 eV or more. The effect is smaller for the tetramers and for n=5 and 6 where the cohesive energies are almost identical. One can conclude that the strength of the Au-H bond is of the order of a Au-Au bond or even stronger. A comparison of the cohesive energies in the different functional shows that PBE and BLYP yield similar results, with slightly higher values (less than 0.2 eV) in PBE. The strongest chemical bonds are suggested in the LDA functional where the cohesive energies are estimated to be up to 0.7 eV higher than in PBE.

In order to get an idea, if there are cluster with an enhanced stability, the second derivative of the energy $\Delta^2 E$ was calculated using the formula

$$\Delta^2 E_{\text{coh}}(n) = E_{\text{coh}}(n+1) - 2E_{\text{coh}}(n) + E_{\text{coh}}(n-1)\,, \tag{3.10}$$

with n as the number of atoms in the cluster. If the cohesive energy at a certain cluster size is particularly high in comparison to the neighbouring cluster sizes, $\Delta^2 E$ takes a high value, indicating a high stability for this cluster. In the inset of Fig. 3.21 pronounced maxima of $\Delta^2 E$ occur at n=4 and 6 revealing the high stability of Au_4, Au_3H and Au_5H. For the neutral clusters an even number of atoms is synonymous with an even number of electrons and therefore the observed maxima are a consequence of spin-pairing.

The strong gold-hydrogen binding can also de deduced from the dissociation energies. The dissociation energy corresponding to fragmentation with loss of a monomer is defined as follows

$$E_{\mathrm{D}}(n) = E(n) - [E(n-1) + E(1)] \tag{3.11}$$

with $E(n)$ as the energy of the n-atom cluster. Fig. 3.22 shows the dissociation energies of the neutral ground states of Au$_n$H clusters with respect to loss of a hydrogen atom respectively gold atom. As can be seen, it takes significantly more energy to dissociate a hydrogen atom than a gold atom from the cluster. For Au$_2$H and Au$_3$H the difference is around 1 eV. At larger cluster sizes the difference is reduced to $\sim$0.25 eV but does also depend on the functional. The dissociation energies exhibit a pronounced odd-even alternation as observed for bare gold clusters [49]. The highest values for E_{D} occur for n=3 and 5. The dissociation of a hydrogen atom takes $\sim$3 eV in the PBE functional at these cluster sizes. In these cases all electrons are paired what hampers the separation of the hydrogen atoms. The dissociation energies for n=2,4 and 6 are also remarkably high with E$_{\mathrm{D}}$ $\sim$2.5 eV in PBE. The data in the BLYP and PBE functional is almost identical for Au$_n$H, except for fragmentation of a gold atom where the curve is shifted by about 0.3 eV. Without gradient-corrections (LDA) the dissociation energies are more than 0.5 eV higher. The conclusions drawn do not depend on the choice of the functional. The different functionals mainly result in a vertical shift of the curves.

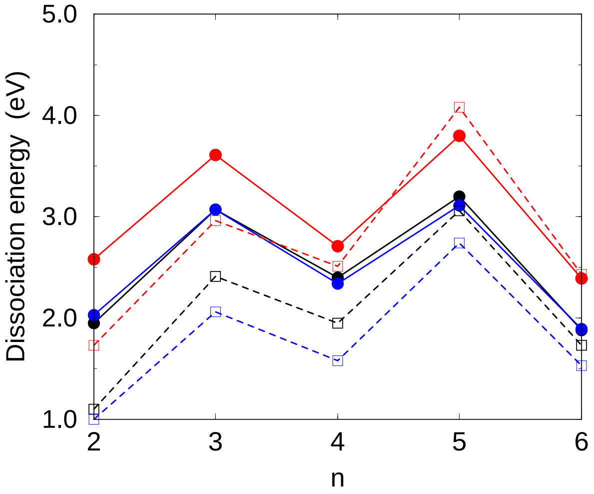

Figure 3.22: Dissociation energies of the neutral Au$_n$H clusters in the ground state with respect to loss of a hydrogen atom (solid lines, filled circles) respectively gold atom (dashed line, open squares). LDA in red colour, PBE in black, BLYP in blue.

From the electronic density of states shown in Fig. 3.16 one can extract the size of the HOMO-LUMO gap in the PBE functional. It is defined as the energy difference of the highest occupied molecular orbital (HOMO) with respect to the lowest unoccupied molecular orbital (LUMO). Generally, the sizes with an even number of electrons have larger HOMO-LUMO gaps. This is due to the spin-pairing effect that stabilises the clusters. The largest gap occurs in the Au$_2$H$^-$ cluster with 2.5 eV, the smallest for

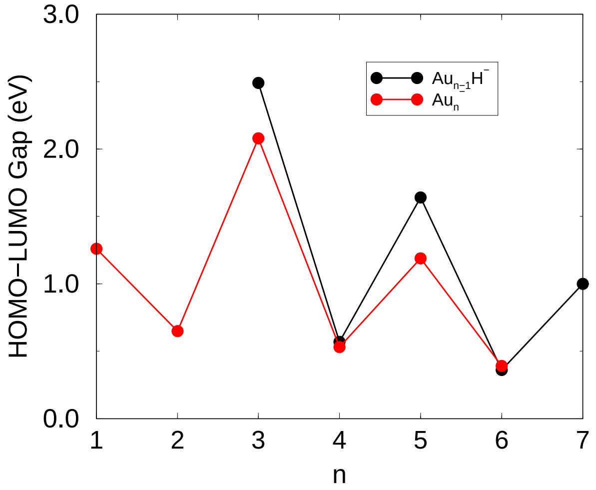

Figure 3.23: The HOMO-LUMO gaps for $Au_{n-1}H^-$ and Au_n^- in the PBE functional extracted from Fig. 3.16.

Au_5H^- (0.5 eV). For n=4 and 6 the HOMO-LUMO gap is nearly identical for the bare and hydrogenated clusters and amounts to ∼0.5 eV. It is significantly larger for the three- and five-atom species. Here the gap is 2.5 eV respectively 1.5 eV for the hydrogenated species whereas the gap for the bare gold clusters is about 0.5 eV smaller. The larger gaps for Au_nH^- indicate enhanced stability relative to their bare counterparts. The size of the HOMO-LUMO gap is an indicator for the chemical reactivity. To activate a reaction it is necessary to extract electrons from a low lying HOMO or to add them to a high lying LUMO which is energetically unfavourable in the case of a large HOMO-LUMO gap.

The most important conclusions from this section are the following: (i) the hydrogen bond in Au_nH clusters is strong (comparable to a Au-Au bond or even stronger), (ii) many properties presented are subject to an odd-even alternation caused by the spin-pairing effect. It is also worth to comment another time on the performance of the different xc-functionals. As discussed in Section 3.3.2, PBE and LDA predicts the same equilibrium structure for all neutral and anionic clusters, whereas BLYP tends to prefer the more open structures. The analysis of cohesive and dissociation energies showed that PBE and BLYP yield very similar values, in opposition to the LDA functional for which a much stronger binding is obtained.

3.3.6 Vibrational properties

At the end of this chapter, the vibrational properties of Au_nH clusters are discussed. In order to determine the vibrations of hydrogenated gold clusters the potential energy surface was analysed. Using finite differences the curvature of the potential energy surface was calculated in the vicinity of the locally minimised geometries. In this way the stability of all anionic isomers in the PBE functional was checked and those were discarded with negative eigenfrequencies since they indicate that the atomic configuration does not correspond to a minimum on the potential energy surface.

The fact that vibrational spectra are sensitive to atomic configurations makes them a useful tool for the determination of cluster geometries. This was demonstrated by Xu *et al.* [70] that combined vibrationally resolved PES spectra with *ab initio* calculations to identify the geometry of small silicon cluster anions. However, PES spectra with such a high resolution are difficult to obtain and are usually only available for cluster systems that are easy to handle in experiment like silicon clusters. The resolution of inhomogeneous cluster systems like the hydrogenated gold clusters is generally lower and it is not possible to deduce vibrational properties from Fig. 3.5. Nevertheless the vibrational analysis presented here gives an interesting insight into the eigenmodes of Au_nH^- clusters and may be compared to experimental data in the future when higher resolved data may be available.

The frequencies of the "parent-related" Au_nH^- clusters span the range ~30-1800 cm^{-1}. As an example for the distribution of the vibrational density of states (VDOS) the spectra of Au_3H^- and Au_5H^- are shown in Fig. 3.24. All eigenmodes of the smaller cluster and some example eigenmodes of Au_5H^-(e) are illustrated in Fig. 3.25. The highest frequency that occurs in the anionic hydrogenated clusters is at around 1800 cm^{-1} (a) and corresponds to a hydrogen in-plane stretch mode. Also the other high frequency modes involve the hydrogen atom. It is an out-of-plane mode at ~ 340 cm^{-1} (b) and an in-plane wave mode at ~ 210-260 cm^{-1} (c) (not observed for Au_2H^-(c)). This is true for all clusters discussed except for Au_5H^-(e) where the bridge position of the hydrogen atom changes the ordering of the eigenmodes. For this structure the hydrogen in-plane stretch mode lies at 1200 cm^{-1} and the other in-plane mode has a much higher frequency (800 cm^{-1}) than for the other structures. In contrast, the hydrogen out-of-plane mode is about at the same frequency for all clusters. There are other common features in the vibrational spectra. The breath mode is located at about ~ 125 cm^{-1} [(d) and (i)], also squeeze-modes (e) and wiggle-modes (f) are

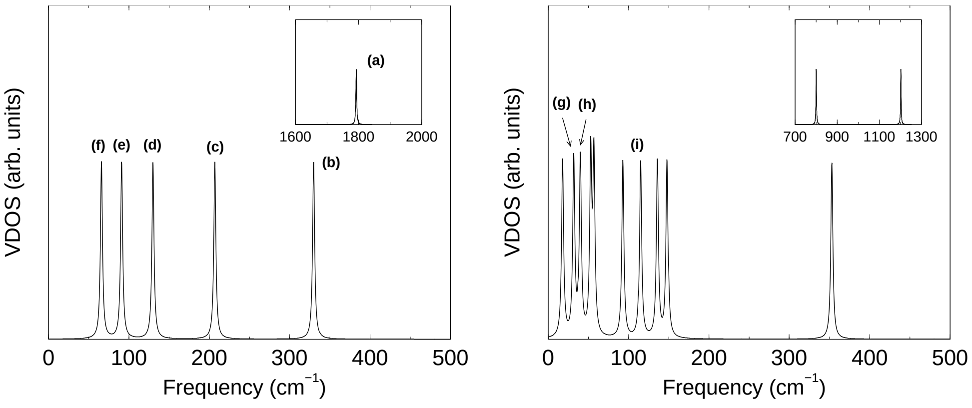

(a) $Au_3H^-(a)$ **(b)** $Au_5H^-(e)$

Figure 3.24: Vibrational spectra for Au_3H^-(a) and Au_5H^-(e). The frequencies have been broadened by a 3 cm^{-1} Lorentzian. In the inset the position of the high-frequency mode is shown. The numbering (a)-(i) indicate the eigenmodes displayed in Fig. 3.25.

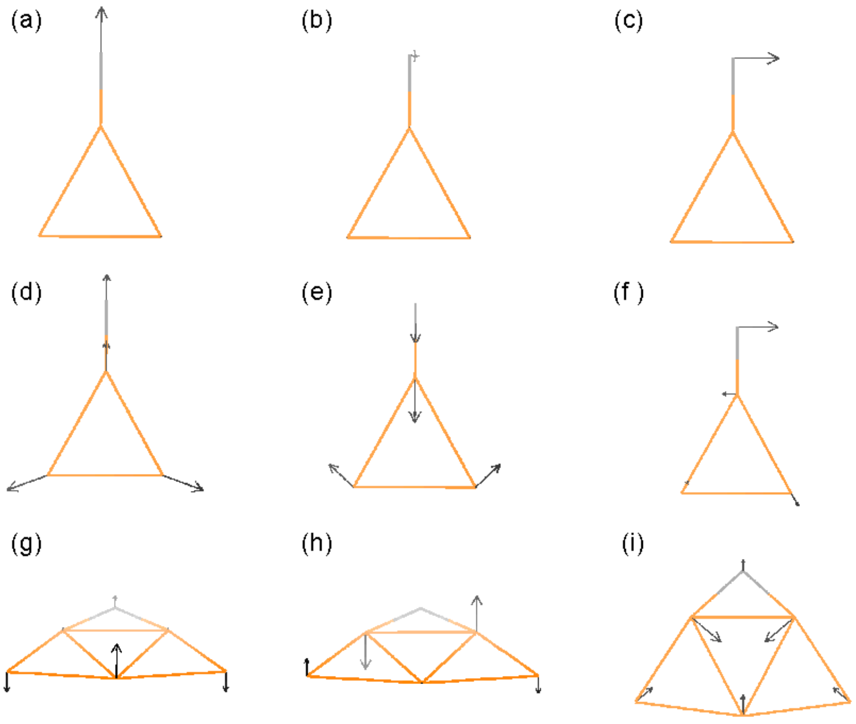

Figure 3.25: Eigenmodes of selected Au_nH^- clusters: Figure (a)-(f) show all eigenmodes of Au_3H^-, (g)-(i) show some exemplary eigenmodes of Au_5H^-.

observed at similar wavenumbers for different structures. In the low frequency region butterfly modes occur for the larger clusters ($n \geq 4$) where the atoms oscillate in three dimensions (out-of-plane). Besides the hydrogen out-of-plane mode these are the only vibrations with an atomic movement out of the cluster plane. One can distinguish between symmetrical (g) and asymmetrical (h) butterfly vibrations. Both types have frequencies around ~ 30 cm^{-1}. There is one butterfly-mode for Au_4H^-, two for Au_5H^- and three for Au_6H^-.

Note, that the potential energy surfaces of the gold cluster and hydrogenated gold cluster systems are very shallow and special care was needed to obtain reliable results for the vibrational spectra.

3.4 Summary

In the first part of this chapter a large number of stable bare and hydrogenated clusters both in the neutral and anionic state were presented. The comparison of VDEs obtained from photoelectron detachment experiments to *ab initio* calculations allowed us to determine the structures of the hydrogenated gold clusters. It turned out that the standard interpretation namely associating the lowest-energy isomer with the one detected in the cluster beam does not yield satisfactory results. An alternative approach to the analysis of photodetachment experiments was presented that gave excellent agreement to experiment. It is based on the fact that chemisorbed cluster systems as $\mathrm{Au}_n\mathrm{H}$ are considerably more complex than bare clusters since the process of the cluster generation has also to be taken into account. This interpretation gave excellent agreement with experiment. Using this interpretation it was even possible to understand complex photodetachment spectra that exhibit a variety of peaks.

In the next part the surprising similarity in the VDE of Au_n^- and $\mathrm{Au}_{n-1}\mathrm{H}^-$, as measured in experiment, was investigated theoretically. An analysis of cluster geometries and VDEs revealed that this effect can only be expected when Au_n^- and $\mathrm{Au}_{n-1}\mathrm{H}^-$ geometries are similar. The tempting idea that the hydrogen atom acts like a gold atom, giving away its electron to a common electron gas was excluded on the base of a charge transfer analysis. The discussion of the electronic density of states yield first hints how this phenomenon can be explained. The HOMO of the four- and six-atom clusters revealed the same character for bare and hydrogenated clusters. For these cluster sizes the analysis of the wavefunction of the detached electron gave the answer why the VDE is so similar. The detached electron is to a large extent localised in the same regions of the bare and hydrogenated cluster. This explains why the VDE is not altered significantly when the gold atom is replaced by a hydrogen.

The investigation of the electronic properties demonstrated the high stability of small hydrogenated gold clusters. The Au-H bond proved to be at least as strong as a Au-Au bond in the cluster. The HOMO-LUMO gaps of $\mathrm{Au}_{n-1}\mathrm{H}^-$ were as large as for Au_n^- and even larger for n=3 and 5. Furthermore a strong dependence on the number of electrons in the system was observed for the dissociation energy and the HOMO-LUMO gap. This is caused by a strong spin-pairing effect stabilising the species with an even number of electrons.

In the last section the frequency range of $\mathrm{Au}_n\mathrm{H}^-$ clusters was determined to be $\sim$ 30-1800 cm^{-1}. The lowest frequencies were assigned to butterfly modes involving an out of plane movement, the highest frequency corresponds to an in-plane hydrogen stretch.

Chapter 4

Deposited Si_4 Clusters

4.1 Introduction

One of the main goals of nanotechnology is the arrangement of atomic-scale building blocks into technologically useful shapes. Promising candidates as building blocks are the so-called "magic clusters". These clusters possess an extraordinary stability which is caused by special electronic (shell closings) or geometric (high-symmetrical structure) properties. The most prominent example are the fullerens with the famous soccer ball-like C_{60} cluster. The idea is that these building blocks self-assemble in a reasonable fashion or alternatively a method is found that allows to deposit clusters in exact positions. Such arrays of nanoclusters may be useful for electronic devices, data storage or as catalysts for chemical reactions.

It is already possible to arrange single clusters on a surface using the tip of a Scanning Tunneling Microscope (STM) but this method is limited to a few species. Very recently the spontaneous assembly of a large (10^{11} clusters), perfectly ordered nanocluster array of indium clusters on a silicon crystal was reported [71]. In this experiment evaporated metal atoms self-assembled on the surface forming regularly arranged In_6 clusters. An alternative approach is to generate first the clusters in the gas phase, to choose a cluster size by using mass-separation in the second step and finally deposit these species on the surface. Since cluster properties do strongly depend on the number of atoms n this approach has the advantage that clusters of a well-defined size n ("monodisperse") can be used to be deposited on the surface. In the process of deposition it is crucial that clusters are landed with low kinetic energy ("soft-landed") on the substrate to avoid fragmentations upon impact. It depends on the choice of the substrate and the cluster material if the clusters diffuse on the surface, form islands or coalesce to larger particles. Furthermore it is of great interest how the surface-cluster interaction alters the electronic end geometric properties of the deposited clusters.

The question arises which properties make a cluster (defined by the chemical element and its size) a suitable building block in a new cluster material. Such building blocks can be condensed into bulk materials while keeping their individual identity, if the intra-cluster covalent bonding is stronger than the van-der-Waals cluster-cluster bonding. This is, e.g., the case for two C_{60} clusters: C_{120} is much more stable than two weakly interacting C_{60} [72], but the two C_{60} clusters do not fuse at room temperature because a considerable energy barrier to spontaneous coalescence exists. If this barrier is too small the clusters might merge into amorphous bulk material even at low temperatures. It is therefore clear that the relative stability cannot be the only criterion making a "magic" cluster to a candidate as building block for a new cluster material. Instead, the interaction between neighbouring clusters must be considered and studied in detail.

In this work the results from *ab initio* calculations are combined with experimental data to get insight into the interaction between neighbouring "magic" clusters. As a first example magic Si_4 clusters are selected which were found [73, 74] to be very stable in the gas phase. Using DFT the behaviour of Si_4 clusters on two different substrates was studied: (i) on a reactive Au(111) surface and (ii) on an inert surface like e.g. graphite. The latter system was investigated experimentally by Martin Grass and Gerd Ganteför [75] at the University of Konstanz. The data from XPS (X-ray Photoelectron Spectroscopy) measurements will be discussed in context with the results from the simulations.

4.2 Methods

For the study of silicon clusters as presented in this chapter the pseudopotential created by Wanda Andreoni was used. The pseudopotential, that accounts for the interaction of the four valence electrons of Si (electronic configuration: [Ne] $3s^2$ $3p^2$) with the core, was constructed following the scheme of Troullier-Martins [26]. The cutoff radii for the s and p channels in the pseudopotential were chosen to be 1.7 Bohr and the s component was used as the local part of the pseudopotential. For gold the pseudopotential described in Section 3.2 was applied.

For the simulations involving only silicon atoms the valence wavefunction was expanded in a plane wave basis set up to a kinetic energy cutoff of 20 Rydberg. The calculation were performed using a cubic cell free of periodic boundary conditions with an extension of 40 Bohr in each direction.

In the study of silicon clusters adsorbed on the gold surface the cutoff had to be increased to 50 Rydberg due to the presence of the gold atoms. In the optimisations all degrees of freedom were free to relax except the atoms of the bottommost layer of the surface which were kept fixed in their bulk position.

All calculations presented in this chapter use the PBE functional [18]. This is because the description of the Au(111) surface considered here is the best in this functional (see also Section 5.4.1). Moreover, the properties of silicon clusters in the gas phase are well reproduced in the PBE functional. In Table 4.1 the experimental values for the binding energy, the bonding distance and the vibrational stretch of the silicon dimer are compared to the PBE results. All studied properties of Si_2 are in close agreement to experiment confirming the validity of the computational approach.

Note, that the numbers given in the table correspond to the triplet configuration of Si_2 which is the ground state configuration. It is 0.85 eV lower in energy than Si_2 in

	d(Å)	E_B (eV)	$\omega(cm^{-1})$
PBE	2.28	3.57	481
Exp.	2.25	3.76	509

Table 4.1: Characteristics of Si_2: the bond length d, the binding energy E_B and the frequency of the vibrational stretch ω in the PBE xc-functional is compared to experimental data (d and E_B from Ref. [76], ω from Ref. [77]).

the singlet configuration. The ground state of the silicon atom is also the triplet state being 1.46 eV favoured over the singlet state.

4.3 Results and Discussion

4.3.1 Si_4 in the gas phase

It is well established [78, 79] that the equilibrium structure of the Si_4 cluster is rhombic. The structure obtained from DFT calculations including the bonding distances is shown in Fig. 4.1(a). Four equivalent bonds of the length 2.42 Å are formed and one shorter bond of 2.32 Å. The shape of the cluster in the anionic state tends to be slightly more quadratic. The formerly shortest bond elongates to 2.36 Å whereas the equivalent bonds shorten to 2.33 Å. The calculated vertical detachment energy (VDE) of Si_4 in the PBE functional is 2.21 eV in excellent agreement to the experiment value of 2.1 eV (taken from S. Burkart's PhD thesis [41]). On the right hand side of Fig. 4.1 the electronic density of states of the occupied and some unoccupied states is displayed. There is a distinct gap between the highest occupied molecular orbital (HOMO) and the lowest unoccupied molecular orbital (LUMO). The large size of the HOMO-LUMO gap (E_gap=1.1 eV) indicates the high stability of this cluster. The correlation between the size of the HOMO-LUMO gap and the cluster stability was demonstrated by Kietzmann *et al.* [80]. In this work the electronic structure of small fullerenes was investigated theoretically and experimentally. The fullerenes with a large HOMO-LUMO gap like C_{60} (E_gap=1.6 eV) and C_{32} (E_gap=1.3 eV) proved to be much more stable with respect to fragmentation than clusters with a small gap. This is an agreement with the general assumption that low chemical reactivity is associated with a large E_gap, because it is energetically unfavourable to extract electrons from a low lying HOMO or to add them to a high lying LUMO, which would be necessary to activate a reaction. In the case of small silicon clusters highly stable sizes were suggested to be n=4, 7 and 10 on the base of monomer separation energies that showed local maxima at these sizes [78].

These findings advise that Si_4 is a promising candidate as a building block. The question, if a cluster material formed by Si_4 species can exist will be addressed in the following sections.

4.3.2 Si_4 on Au(111)

One of the proposed substrates for the deposition of Si_4 clusters is the gold surface. In this part of the study it was investigated using *ab initio* methods if this surface

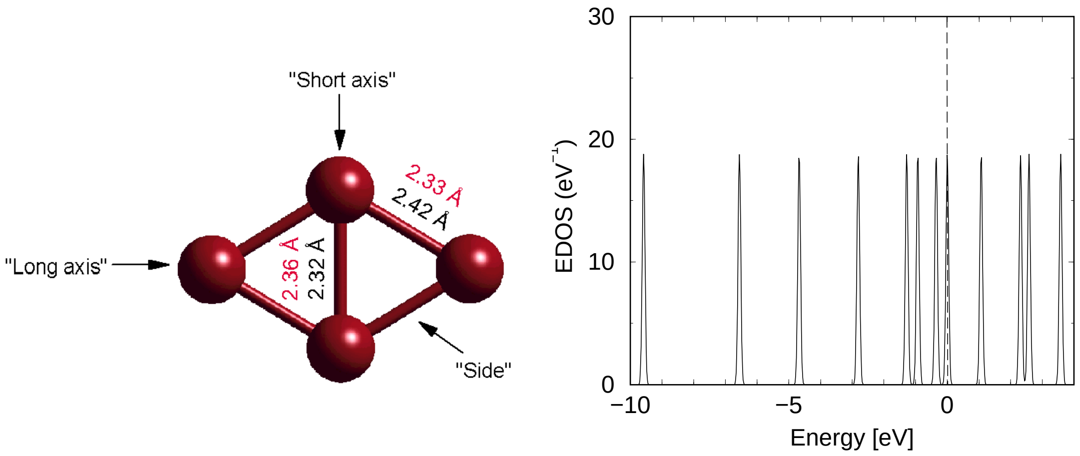

(a) Structure of Si$_4$

(b) EDOS of Si$_4$

Figure 4.1: In (a) the rhombic structure of Si$_4$ is shown including the bonding distances in the neutral (black) and anionic (red) state. The arrows denoted “long axis”, “short axis” and “side” indicate the different direction of approach as studied in Section 4.3.3. In (b) the electronic density of states for Si$_4$ is displayed. The highest occupied molecular orbital (HOMO) was shifted to 0 eV. The states at positive energies (on the right of the dashed line) are unoccupied. Note the large HOMO-LUMO gap between the highest occupied and the lowest unoccupied state of 1.1 eV.

is a suitable substrate for the deposition of silicon clusters. For the modelling of the surface a slab containing four layers of 25 atoms each, was used to study the adsorption of neutral Si$_4$. This slab was taken from a work by Grönbeck *et al.* [43] that studied methanethiol and dimethyl disulfide adsorption on Au(111) (see also Section 5.3).

Three different Si$_4$/Au(111) systems were considered: two configurations in which the cluster lies flat on the surface and one configuration in which the cluster stands upright (see Fig. 4.2). It has to be mentioned that the purpose of this investigation is to get insight in the nature of the adsorption of Si$_4$ on gold rather than determining the equilibrium structure. The configuration chosen are likely to be very close to the real ground state but considering the large number of possible configurations of a four-atomic cluster on a surface one cannot expect to find the ground state without taking more topologies into account.

The optimisation of the geometries revealed that the adsorption in the upright position is not stable. During the optimisation process the cluster rearranged to end up lying flat on the surface. A top and a side view of the topologies corresponding to a local minimum on the potential energy surface are shown in Fig. 4.3 (a) and (b). In both structures the cluster is parallel to the surface, however the configurations differ in the adsorption sites of the silicon atoms. In structure (a) two atoms are located in bridge positions and hollow positions respectively (for the definition of these positions see Fig. 5.3). This gives rise to four equivalent Si-Si bonds of 2.47 Å and one bond of 2.81 Å. Configuration (b) arises from (a) when the cluster is shifted by $\sim$0.5 Å along the next-nearest neighbour direction of the surface. This leads to a less symmetric

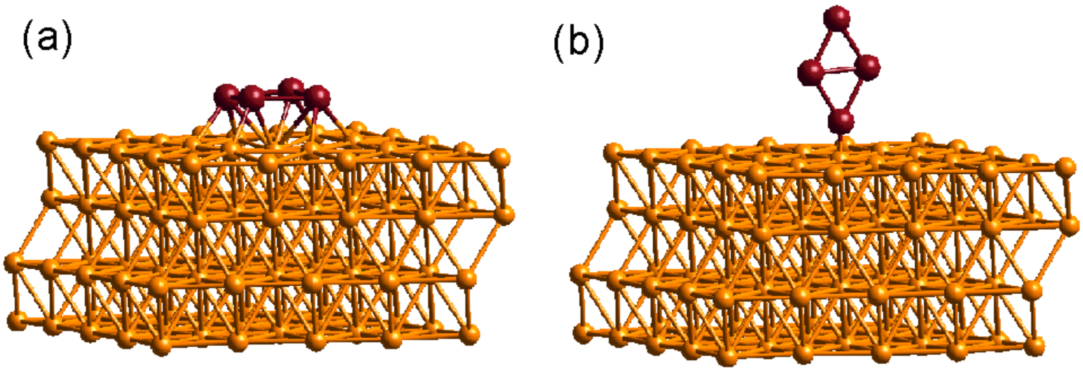

Figure 4.2: The supercell used for the simulation of Si_4 adsorption on Au(111). The surface is modelled as a slab of four layers containing 25 atoms each. Two types of adsorption were considered: (a) Si_4 flat on the surface and (b) Si_4 standing upright on the surface.

geometry in which all silicon atoms are close to hollow sites resulting in more Si-Au bonds than in configuration (a). The formerly equivalent bonds have now different length scattered in the range of 2.57-2.67 Å whereas the other bond is shortened to 2.61 Å.

Comparing these bonding distances to the case of Si_4 in the gas phase (four 2.42 Å bonds and one 2.32 Å bond), it is evident that the adsorption results in a significant relaxation of the silicon cluster. The elongation of the Si-Si bonds relative to the isolated, fully relaxed cluster amounts to 2-21% for structure (a) and 5-13% for structure (b). This change in the geometry of the cluster is caused by the larger Au-Au distances (2.93 Å in PBE) in the Au(111) surface. For an optimum substrate-cluster interaction the cluster has to deform in order to match to the underlying substrate. The large magnitude of the structural relaxation is caused by the considerable mismatch between the Au-Au (in Au(111)) and Si-Si (in Si_4) bonds.

As can be seen in Tab. 4.2 the strong Au-Si interaction is also portrayed by the binding energy which is defined as (the total energy of the systems are negative corresponding to bonded states)

$$E_{\mathrm{B}} = -\left[E(\mathrm{Au}(111)/\mathrm{Si}_4) - \{E(\mathrm{Au}(111) + E(\mathrm{Si}_4)\}\right] . \tag{4.1}$$

The adsorption of Si_4 on a gold surface is strong with a binding energy of roughly 1.55 eV per silicon atom. Configuration (b) turns out to be the more stable structure being favoured by 0.16 eV over configuration (a). This is probably due to the larger number of Au-Si bonds in structure (b) than in structure (a) (12 respectively 10 bonds). In structure (a) six out of ten bonds to the surface are in the range of 2.47-2.49 Å. The other bonding distances are either 2.60 or 2.89 Å. In structure (b) there are four bonds of $\sim$2.5 Å, six of $\sim$2.6 Å and two of $\sim$2.65 Å. The adsorption in hollow sites causes shorter bonding distances than the adsorption in bridge site.

The analysis of the average height of the cluster over the surface Δz(Si-Au) reveals the same trend. Configuration (b) in which adsorption in hollow sites occurs is closer to the surface (Δz=1.90 Å) than configuration (a) (Δz=2.00 Å). Besides the relaxation of

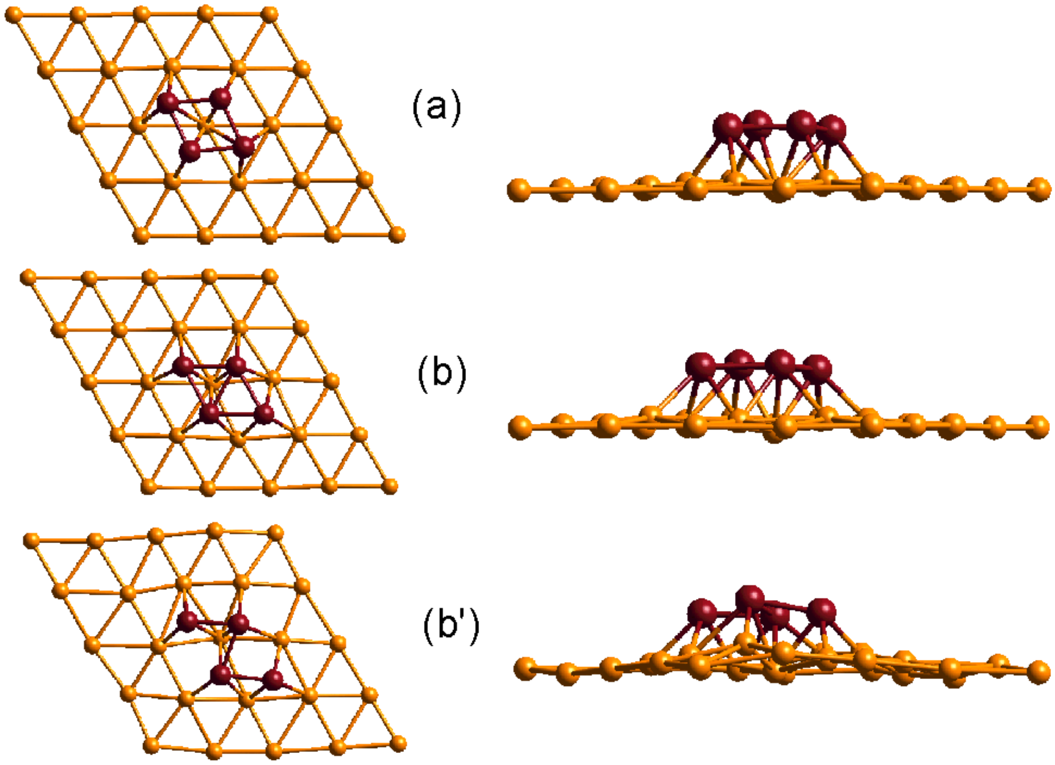

Figure 4.3: Side and top view of a Si$_4$ cluster adsorbed on Au(111): the configurations in (a) and (b) correspond to local minima on the potential energy surface (T=0 K). The structure shown in (b') is the result of a molecular dynamics simulation at 300 K (after ∼ 0.08 ns) with configuration (b) as initial geometry. Note, that it depends on the settings of the graphics program if a bond between two atoms is drawn or not. Beyond a certain cutoff it is assumed that no chemical bond exists between the atoms.

the silicon cluster upon adsorption there is also a relaxation in the surface observable. All Au-Au distances in the vicinity of the cluster are enlarged due to the adsorption. In case (a) the Au-Au bond length elongated to 3.05-3.13 Å, in (b) up to 3.38 Å corresponding to a stretch of 15% relative to the bare surface.

	E_B (eV)	E_B / n (eV)	Δz(Si-Au)
Configuration (a)	6.33	1.58	2.00
Configuration (b)	6.17	1.54	1.90

Table 4.2: Energetics and structure of Si$_4$ on Au(111). The total binding energy E_B, the binding energy per cluster atom E_B/n and the average height of the cluster over the surface Δz(Si-Au) are given.

In order to study the behaviour of deposited species at room temperature Car-Parrinello molecular dynamics [32] (see also Chapter 2) simulations in the microcanonical ensemble were performed. The temperature was initially set to 300 K and during the evolution of the simulation the temperature was set back to this value each time it left the range of 250-350 K. This procedure involves a change of the total energy of the system. After some time the temperature oscillated around the desired 300 K. Note, that the purpose of this approach is not to obtain meaningful statistical averages but rather to obtain some qualitative information about the influence of temperature on the silicon cluster structure.

The initial configuration used in the MD simulations is the one denoted as configuration (b) in Fig. 4.3. Molecular dynamics simulations of these system sizes are computationally expensive and so the time of observation was limited to $\sim$0.1 ns at a time step of 0.125 fs and a fictitious electron mass of 500 atomic units. However this short time scale already revealed interesting information on the room temperature properties of the adsorbed system. A snapshot of a configuration after $\sim$0.08 ns is shown in Fig. 4.3(b'). Even after such a short time period the cluster is heavily distorted. The distance between the two Si atoms on the right is 3.19 Å meaning that the Si-Si bond does not exist anymore. Strong relaxation in the gold surface can be seen in the horizontal and vertical direction. In the direction of the surface normal the lowest and highest gold atom are separated by more then 1 Å.

For a better understanding of the effect of temperature on the cluster geometry it is useful to monitor the position of the Si atoms during the time of the simulation. In Fig. 4.4(a) the trajectory of the four silicon atoms are drawn, in (b) the Si-Si distances for different bonds are given as a function of time. One can see in subfigure (a) that

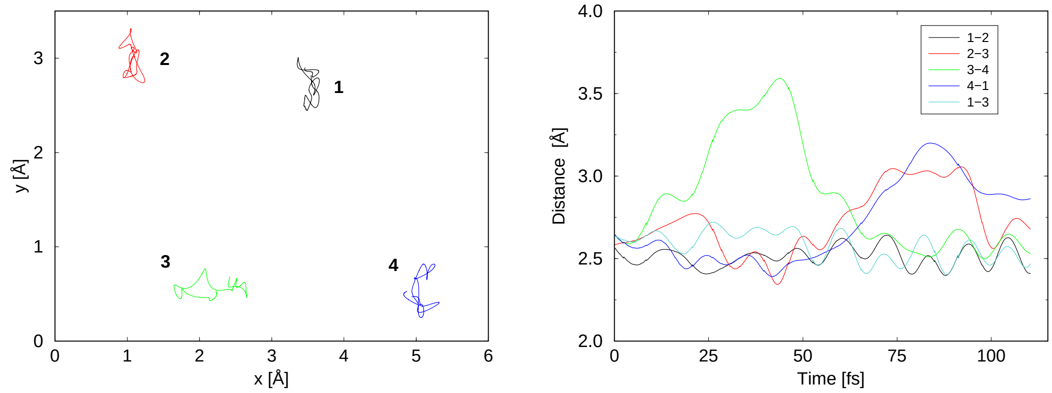

(a) Trajectory of Si atoms

(b) Evolution of Si-Si bonds

Figure 4.4: Analysis of an MD simulation of Si_4 on Au(111) at 300 K: In Fig. (a) the trajectories of the silicon atoms are shown, in Fig. (b) the distances between the Si atoms during the simulation are monitored. The numbering of the silicon atoms is indicated in (a).

the silicon atoms are displaced by significant distances during the MD-simulation. For example atom number three takes positions in x-direction in a range of about 1 Å. This trend becomes even more apparent when the Si-Si distances are analysed (Fig. 4.4(b)). The average Si-Si distance is about 2.5 Å and some bonds actually oscillate around this value. However, at some points in time the distance between silicon atoms exceeds by far the average Si-Si bond length. After only 40 fs atoms 3 and 4 are separated by more than 3.5 Å but also atoms 1 and 4 respectively 2 and 3 are sometimes more than 3 Å apart. In theses situations intra-cluster bonds are broken. Interestingly, during the course of the MD simulation the silicon rearrange such that the bonds regain their standard length (e.g. after 100 fs when all bonds but one are around 2.5 Å).

In conclusion, these simulations clearly demonstrated that the gold surface does not fulfil the desired requirements that are needed as a substrate for depositing Si$_4$ clusters. The substrate-cluster interaction is too strong and leads to a heavy deformation of the silicon cluster even at 0 K. The strong interaction in conjunction with the large lattice mismatch (Si bonds in Si$_4$ vs. Au bonds in Au(111)) causes a significant elongation of the bonds in the cluster and the surface. Due to the high binding energy the mobility of Si$_4$ on Au(111) is probably very low prohibiting any self-assembling process on the surface.

4.3.3 Si$_4$ on graphite

After the discussion of Si$_4$ adsorption on a Au(111) surface in the preceding section, the focus will now be on a graphite surface. These surfaces are known to be inert and interactions with adsorbants are weak. In this part of the study it is therefore assumed that the interaction of Si$_4$ clusters with the substrate is weak and no change of the geometric and electronic structure upon deposition of the Si$_4$ species is to be expected. This means that instead of explicitly including a graphite surface in the simulation the interaction of Si$_4$ clusters in the gas phase was studied. This is clearly an approximation but considering the problems that arise in the modelling of a graphite surface in DFT it is likely to be the more reliable approach. For an appropriate modelling of a graphite surfaces an accurate description of van-der-Waals forces is needed since the interaction of the graphene sheets in governed by forces of this type. As will be discussed in more detail in Section 5.4, DFT fails to reproduce lattice constants and bulk moduli of other materials dominated by van-der-Waals forces.

To account for cluster adsorption on a surface, the silicon clusters are constrained to a two-dimensional movement in the computer simulations. This is only a minor approximation because it is probable that the clusters lie flat on the surface.

For an investigation of energy barriers to spontaneous coalescence the approach of two Si$_4$ clusters was simulated. According to the rhombic symmetry of the silicon tetramer there are various channels of approach thinkable. In Fig. 4.1 three directions relative to the geometry of Si$_4$ are indicated. Approach along the "long" axis, the "short" axis and the "side" of the Si$_4$ cluster. In total there are nine different reaction channels: "long-long", "long-short", "long-side", "short-short", etc. Only for three of these channels a stable Si$_8$ cluster emerged. These configurations are shown in Fig. 4.5(a),(c) and (d) corresponding to the approaches "long-long", "side-long" and "side-side" following the terminology introduced above. The binding energy of a Si$_8$ cluster with respect to two isolated Si$_4$ is defined as

$$E_\mathrm{B} = -\left[E(\mathrm{Si}_8) - 2 \cdot E(\mathrm{Si}_4)\right] . \tag{4.2}$$

The binding energies of configuration (a),(c) and (d) are 1.34, 1.15 and 0.77 eV respectively. At this point, it is interesting to draw a comparison to the stability of three-dimensional structures of Si$_8$. The equilibrium structure of Si$_8$ (see e.g. [78, 79]) is the bicapped distorted octahedron (Fig. 4.5(e)). Its binding energy is 3.97 eV and thus by far more stable than than the two-dimensional structures. Another 3D structure considered is shown in Fig. 4.5(f). Also this cube-like topology is thermodynamically clearly favoured (E_{B}=2.60 eV) over the structures (a), (c) and (d). From theses

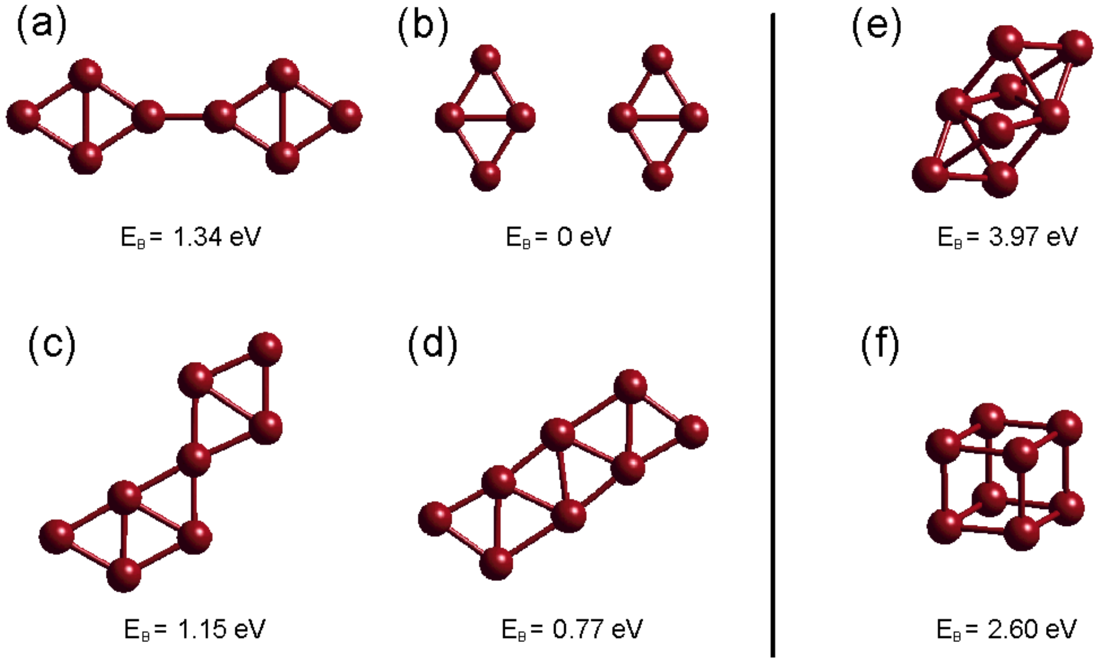

Figure 4.5: Optimised geometries of neutral, flat (a)-(d) and three-dimensional (e)-(f) Si_8 clusters in the PBE functional. The structures on the left side give an impression how two rhombic Si_4 clusters can coagulate to a flat Si_8 cluster corresponding to the situation on an inert surface. The three-dimensional structures on the right side are shown for the sake of comparison 2D↔3D. The stability of the 3D structures is much higher, with (e) as the ground state structure of Si_8. The binding energies E_{B} given, correspond to the energy gained due to the formation of the Si_8 cluster from two Si_4 clusters (see also equation 4.2).

calculations it can be concluded that a planar arrangement of eight silicon cluster is unfavourable. This already indicates that a “simple” coalescence in which two planer Si_4 clusters fuse to a planar Si_8 cluster is energetically disadvantageous compared to the formation of a three-dimensional Si_8 for which much more energy is gained.

These results give only an impression how likely it is that two Si_4 clusters fuse to a Si_8 cluster. However, the question of real interest is, if a barrier exists that prevents coalescence at room temperature. To address this question the potential energy surface was calculated for two different reaction channels namely the approaches corresponding to geometries (a) and (b) from Fig. 4.5. For each point on the potential curve the distance between the closest silicon atoms (see inset in Fig. 4.6) was fixed at a value R and full structural relaxation of the clusters in three spatial dimensions was allowed. This procedure defines R as the reaction coordinate of the system. In Fig. 4.6 the potential energy of the two reactions is shown as a function of R. The introduction of an additional variable is not necessary since the clusters remained in their two-dimensional shape during the optimisation process. No rearrangement out of the plane in which the clusters were initially located was observed. As already discussed the

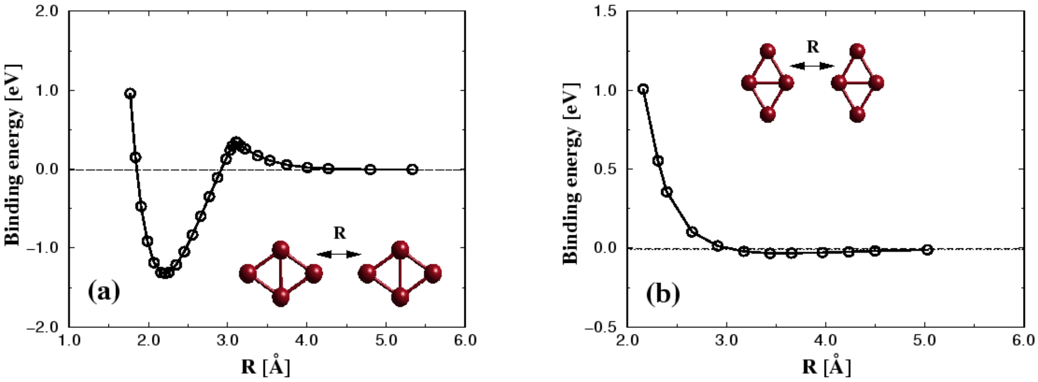

Figure 4.6: Calculated potential energy curves for two neutral interacting Si$_4$ clusters. Two different reaction channels have been calculated: the two tetramers approaching each other with the long axis (a) and the short axis (b) ahead. In case (a) a bond is formed while (b) is repulsive. In (a) an energy barrier is observed at a distance of 3.1 Å and a height of 0.3 eV. The binding energy is calculated as the energy difference between the reacting system and two isolated Si$_4$ cluster.

approach along the long axis (Fig. 4.6(a)) leads to a formation of a bond resulting in a binding energy of 1.34 eV. The reaction creating a Si$_8$ cluster causes a relaxation of the original cluster geometries. The four equivalent bonds in the Si$_4$ cluster which are 2.32 Å in the gas phase shorten slightly to 2.29 Å whereas the length of the remaining bond increases from 2.42 to 2.52 Å. The bond connecting the clusters is rather short with 2.20 Å. For values of R smaller than 1.8 Å the cluster-cluster interaction becomes repulsive. The most important feature in the potential curve is the energy barrier at a distance of 3.1 Å. This barrier is 0.3 eV high and, therefore, it might not be overcome at kinetic energies corresponding to room temperature.

For the geometry displayed in Fig. 4.6(b) the potential energy increases monotonously with decreasing distance corresponding to a repulsive interaction. The two clusters do not fuse and no bond between the clusters is formed.

The large differences between the two geometries discussed might be explained by the different coordination of the Si atoms which are involved. In structure (b) the Si atoms at the acute end of the cluster approach which already have three bonds formed within the clusters, while in (a) the reacting Si atoms have a lower coordination. Accordingly, for the latter case a bond is formed.

There are another two two-dimensional isomers of Si$_8$ remaining (Fig. 4.6(c),(d)). In these cases the definition of a reaction coordinate is not as obvious as for the geometries discussed. The approach does not take place along one of the principal axis therefore the distance between the centre of geometries of the clusters was introduced as a reaction coordinate. However, it turned out that after fixing R to a certain value the topology did not remain similar to the initial geometry but the clusters had the tendency to rearrange to a configuration similar to the one in Fig. 4.6(a). For this reason the reaction channel (a) can be considered as the only one which may result in the coalescence of Si_4 clusters on an inert surface.

In conclusion, the calculations revealed a repulsive interaction between Si_4 clusters constrained to a surface at low temperatures. The theoretical results presented here suggest that a new bulk of pure Si consisting of Si_4 clusters may be existing. In the following section the results from density functional theory are brought into conjunction with experimental data from XPS measurements of deposited silicon clusters on graphite.

Experimental data

The discussion in this section is based on an experimental study by Martin Grass and Gerd Ganteför [75]. In this experiment the clusters were mass-selected and soft landed (E_{kin}=1.2 eV per silicon atom) on a highly oriented pyrolytic graphite (HOPG) which is known to be an inert van-der-Waals surface [81]. The silicon clusters are probably highly mobile on this surface at room temperature and would immediately form large islands of bulk Si if there was no barrier against fusion [82,83]. The number of deposited clusters corresponds to a coverage of about 2% of a Si atom monolayer (ML). There is no generation of surface defects at this relatively low kinetic energy as examined using scanning tunnelling microscopy [81–83]. Fragmentation can not be totally excluded but seems unlikely at this low kinetic energy compared to the binding energy of the clusters [81, 83].

The samples were studied using XPS and only the peak corresponding to the 2p core level of Si is examined in detail (see Fig.4.7). The area of this feature corresponds to the amount of Si deposited on the HOPG. For clean bulk Si an almost symmetric peak centred at a binding energy of 99.4 eV is observed (Fig. 4.7, left (c)). For the deposition of Si atom ions on HOPG (Fig. 4.7, left (b)) a similar peak is observed with a shoulder corresponding to an unresolved feature at 101 eV binding energy. For Si_4 clusters deposited on HOPG (Fig. 4.7, left (a)) a shift of the main peak of 0.5 eV towards higher binding energy and a slightly more intense shoulder corresponding to a broad peak around 102 eV is observed. The small features at binding energies around 101-102 eV are assigned to Si atoms bound to carbon atoms. The chemical shift depends on the coordination number (e.g., Si_2-C, Si-C or Si-C_2). Some atoms and clusters migrate to mono-atomic steps and defects on the HOPG surface and form a covalent bond with carbon atoms there. The main peak corresponds to Si atoms bound to Si atoms. The observed shift of 0.5 eV between the deposited clusters and the deposited atoms is essential. This shift can be explained by a lower average coordination number of the Si atoms in clusters. Similar shifts have been observed in XPS spectra of various mass-selected deposited clusters [82, 85, 86]. In these experiments the clusters are not mobile on the surface [85,86] or, if the clusters can diffuse, the shift vanishes with time due to the formation of large bulk like islands [82]. In our case the clusters are mobile on the surface [81,82] but the shift does not vanish with time. In case of the deposited atoms there is no such shift with respect to the bulk reference sample corresponding to the formation of large bulk-like islands. These findings indicate that deposited Si_4 clusters do not form larger islands but remain as individual clusters on the surface.

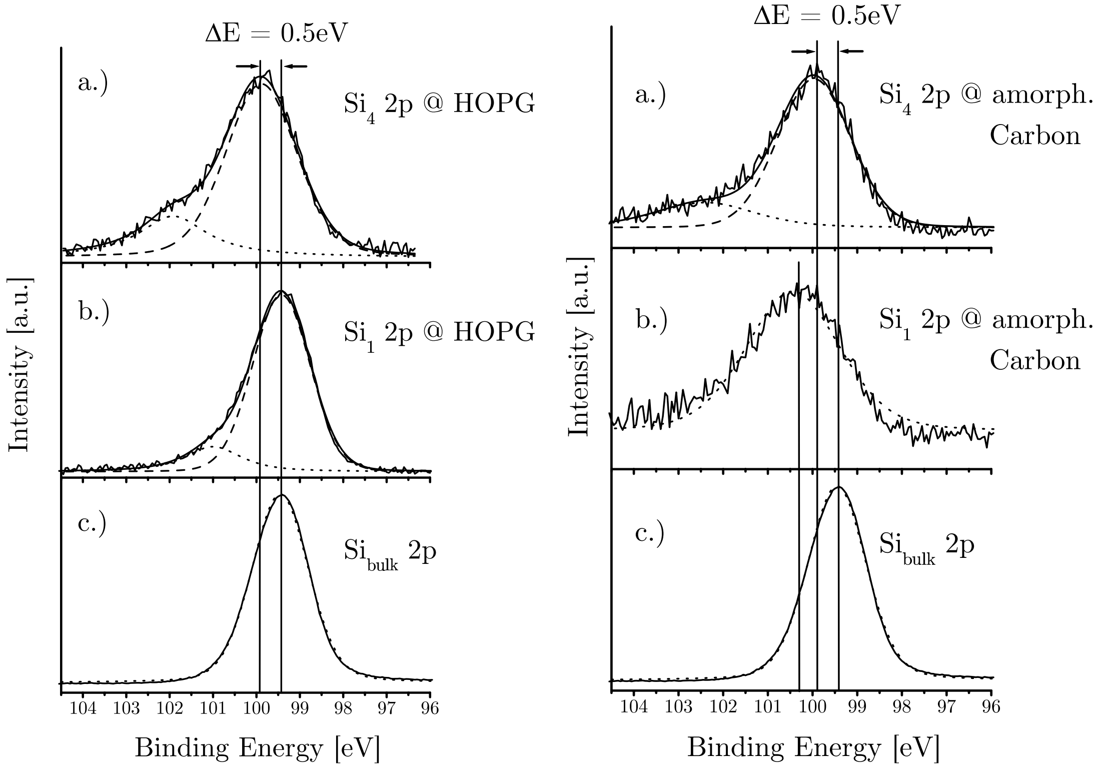

Figure 4.7: On the *left*: XPS spectra of the Si 2p peak recorded for (a) Si$_4$ clusters deposited at 5eV onto HOPG (2% coverage), (b) positively charged Si atoms deposited at 5eV onto HOPG (2% coverage) and (c) for a Si bulk reference sample. On the *right*: XPS spectra of the Si 2p feature recorded for (a) Si$_4$ clusters deposited at 5eV onto amorphous carbon (4% coverage), (b) positively charged Si atoms deposited at 5eV onto amorphous carbon (3% coverage) and (c) for a Si bulk reverence sample. Fits of the experimental data are also displayed in the graphs (Figure taken from [84]).

To support these results the above experiments were repeated with a different sample: amorphous carbon. This surface consists of very small graphitic sheets with no ordering and the number of dangling carbon bonds is extremely high. It is more reactive than HOPG and might bind adsorbates easily. In the right hand side of Fig. 4.7 the corresponding XPS data in comparison with the Si 2p bulk feature is displayed. As expected, for the deposition of Si atom ions (Fig. 4.7, right (b)) at low coverages of up to 4% ML almost no pure Si-Si bonds but only Si atoms bound to carbon are found. No Si islands are formed but the Si atoms are trapped at surface defects. In contrast, the XPS feature corresponding to the soft landed Si$_4$ cluster ions (Fig. 4.7, right (a)) does not exhibit a difference to the case of the HOPG surface (same figure on the left (a)). The tetramers do not react with defect sites of the amorphous carbon and do not coalesce as to be expected for "magic" clusters. Again, these finding support the hypothesis, that Si$_4$ clusters are suitable as building blocks for a cluster material.

4.4 Summary

The main goal of this chapter was to investigate the possible use of “magic” Si_4 clusters as a building block in a new cluster material. In the first part the adsorption of Si_4 on a Au(111) surface was studied. The results of DFT calculations clearly demonstrated that a gold surface is not suitable as a substrate for silicon cluster deposition. The strong cluster-substrate interaction caused a heavy deformation of Si_4 due to the adsorption on the surface. The large mismatch of Si-Si and Au-Au bonds implicated dramatic relaxation in the cluster and the surface. This effect became even more evident when the system was studied at room temperature in an MD-simulation. Here, the cluster occasionally lost completely its original shape due to the cleavage of intra-cluster bonds. These observations are in contrast to the desired properties of the substrate namely a weak cluster-substrate interaction synonymous with a high mobility of the deposited species.

Such a behaviour can be expected of Si_4 clusters on an inert graphite surface. Assuming weak interactions between cluster and graphite surface the interaction between neighbouring Si_4 species was studied. In the calculations a repulsive barrier was found in the interaction potential, which blocks spontaneous fusion of clusters at sufficiently low temperature. This result from *ab initio* simulations suggests that Si_4 may serve as a stable building block.

Indeed it was found in experiment that Si_4 clusters deposited on an inert surface at room temperature show no tendency to form larger islands of bulk Si. XPS data indicated that the clusters do not fuse to Si islands but survive as individuals.

Both sets of data support the idea, that this “magic” silicon cluster is suitable as a building block for a new cluster material consisting of pure silicon. The experimental and the theoretical data on its own can not be considered as a prove of the hypothesis. However, there is a considerable agreement between these first theoretical and experimental results.

These encouraging findings for Si_4 stimulate additional theoretical and experimental studies of other “magic” clusters. If it will finally turn out to be really possible to synthesise such a material this will open a door to a whole new world of material science based on the many magic clusters already found in the gas phase.

Chapter 5

Self-assembled Monolayers on Au(111)

5.1 Introduction

In 1983 Nuzzo and Allara [5] discovered that when a gold surface is exposed to a dilute organo-sulfur solution a self-assembled monolayer (SAM) is spontaneously formed. Over the last twenty years SAMs attracted much interest from both the experimental and theoretical community [87]. Meanwhile the variety of SAMs has grown dramatically. Besides the original substrate of gold, it has been demonstrated that SAMs can also be grown on silver, platinum, copper or palladium. Furthermore, one is not restricted to the simple adsorbant used by Nuzzo, namely alkanethiols ($HS(CH_2)_{n-1}CH_3$), but instead either the headgroup (the group anchoring to the surface) and tail group (the unit furthest away from the surface) of the organic chains can be substituted. This is an extremely attractive feature that allows to tailor SAMs with specific properties. In this way, a small microscopic change in the structure, can alter macroscopic properties of the monolayer like friction, adhesion or corrosion. This enables SAMs to be used in a wide range of applications such as microcontact printing [88], corrosion inhibition [89, 90], molecular recognition [91] or as lubricant [92].

In the vast field of organic monolayers those grown from alkanethiols on gold are probably the best characterised system due to its easy preparation and the high stability of the monolayer. In recent years this has become the model system for the study of ultrathin organic films. This system was studied at various chain lengths n and monolayer coverages Θ. In particular at least four different phases were observed during the growth process corresponding to different coverages. In the early stages of the monolayer formation process the chains are lying flat on the surface bonded through van-der-Waals interactions [93]. At the end of the growth process, at full coverage, the chains are standing upright, tilted by $\sim 30^\circ$ away from the surface normal. The system at full coverage is the most interesting since it allows the efficient functionalisation of the surface. Also, most experimental information is available for this coverage regime (at n=6-18). However, two important questions are still unsolved: What is the adsorption state of the sulfur atoms on the surface and is there a dependence on chain length or coverage? An answer to these questions and a thorough understanding of the headgroup-gold interaction is crucial for an optimal tailoring of SAMs to fulfil specific demands for technological applications.

In this study monolayers at full coverage consisting of n=4 and n=10 carbon units were investigated. The system at n=10 is of special interest because a study at this chains length [94] created the unsolved puzzle of the sulfur adsorption state on the surface. By comparing the data sets for short (n=4) and long (n=10) chains the influence of the chain length on the monolayer structure can be understood.

In the next two sections an overview is given on the current research situation up to date. First of all a selection of the most important experiments are presented and different models of the headgroup structure are discussed. Then the focus is on the theoretical approaches taken so far, which include classical (MM = "molecular mechanics") and quantum mechanical (QM) studies. The advantages and failures of the two methods are contrasted and a new approach that combines QM methods with MM methods is presented in Section 5.4. The application of this approach and the results are discussed elaborately in Section 5.5, where topics ranging from energetics to structure to electronic properties are covered. The comparison of data from the simulations to experimental data will play an important role in the discussions. Throughout the whole chapter the dependence of physical properties on chain length and monolayer coverage will be discussed.

Note, that in this chapter the energy unit "kcal/mol" will be used because the results in most publications on this field are given in this unit. In appendix A the conversion factors between different energy units are listed.

5.2 Experimental situation

The aim of this chapter is to illustrate what is already known about alkanethiol monolayers on gold and what still has to be understood. In the following the notation Cn/Au(111) (n denoting the number of C atoms per chain) will be used corresponding to a monolayer formed by adsorption of RSH (R=$CH_3(CH_2)_{n-1}$) chains on the Au(111) surface. It is remarkable that growth from RSSR leads to monolayers indistinguishable from a monolayer formed by RSH adsorption. Note, that all experiments reported in this section were performed in the full coverage regime.

One of the first steps in the characterisation of a surface system is the determination of the periodicity of the crystalline structure (unit cell). Early electron diffraction studies of monolayers of alkanethiolates on Au(111) surfaces revealed that the symmetry of sulfur atoms is hexagonal with an S-S spacing of 4.97 Å [95, 96]. This means that the monolayer forms a $\sqrt{3} \times \sqrt{3}R30°$ unit cell that contains one molecule per unit cell (one sulfur per three gold atoms). It implies that all sulfur atoms in the system are equivalent. The unit cell is sketched in Fig. 5.1(a). Therefore, it was believed for a long time that alkanethiols bind as thiolates ($S(CH_2)_{n-1}CH_3$) to the surface

$$\mathrm{CH_3(CH_2)_{n-1}SH + Au \longrightarrow CH_3(CH_2)_{n-1}S - Au + 1/2H_2} \tag{5.1}$$

forming a $\sqrt{3} \times \sqrt{3}R30°$ structure. This picture of sulfur adsorption is known as "standard model" or "thiolate model". It involves a cleavage of the S-H bond in

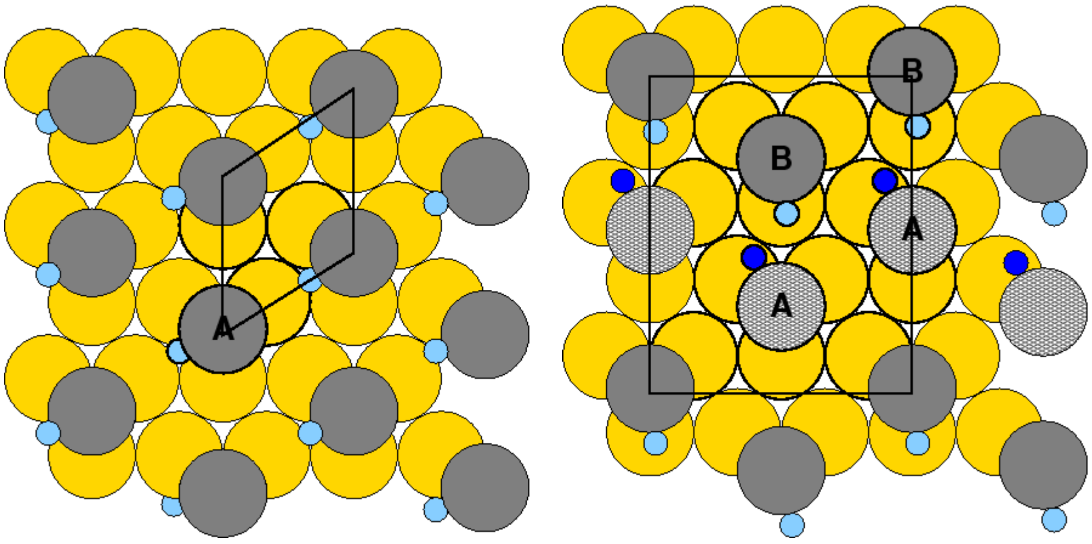

(a) $\sqrt{3}\times\sqrt{3}R30^\circ$ **(b)** $c(4\times 2)$

Figure 5.1: Proposed unit cells in which SAMs on Au(111) were observed in experiment. Yellow disks stand for gold atoms in the first layer, the hydrocarbon chains are in gray, and the sulfur atoms in blue. On the left (a) the smaller $\sqrt{3}\times\sqrt{3}R30^\circ$ unit cell with one chain per cell, on the right the corresponding $c(4\times 2)$ superstructure consisting of four chains per cell. The letters A and B indicate different types of hydrocarbon chains, differing in the adsorption site of the sulfur atoms or the chain orientation. This model with only two instead of four non-equivalent chains was proposed in Ref. [94].

the thiol upon adsorption. One speculates that the hydrogen atoms desorb form the surface as H_2, since no evidence exist for atomic hydrogen on the surface that may hinder further adsorption of sulfides. Moreover, H_2 is known to readily desorb from Au(111) [42]. However, no clear evidences for H_2 production upon film growth of thiol molecules seem to exist. The adsorption as thiolates takes place in the all-trans configuration of the chain as illustrated in Fig. 5.2. In this configuration all CH_2 units have the same orientation equivalent to identical dihedral angles over the whole chain. Later a two chain per unit cell model was proposed [97] before Camillone *et al.* [98] reported a unit mesh containing four distinct hydrocarbon chains in a unit cell of dimension 8.68×10.02Å. This packing arrangement found in a low temperature helium diffraction study can be described as a $c(4\times 2)$ superlattice of the simple hexagonal $\sqrt{3}\times\sqrt{3}R30^\circ$ unit cell. This observation was confirmed by X-ray diffraction [99, 100] and STM measurements [101]. The $c(4\times 2)$ superstructure gives in principle space for four non-equivalent molecules in the unit cell.

In 1994 a study by Fenter *et al.* [94] created a still unresolved puzzle. Their grazing incidence X-ray diffraction data turned out to be incompatible with any kind of thiolate model. Instead, they suggested a model that assumes a dimerisation of the sulfur head groups upon adsorption ("disulfide model" or "sulfur-pairing model") with two different types of sulfur atoms in the $c(4\times 2)$ structure (Fig. 5.1(b)). In their model the S atoms are separated by only 2.2 Å and form a chemical bond. One of the S atoms is bond to the surface, the other is slightly further away from the surface and not bound to it. This picture was extracted from X-ray data in two steps: in the first step, it was concluded from the absence of some peaks in the diffraction pattern that there are not four but only two non-equivalent sulfur atoms in the unit cell (see Fig. 5.1(b)). A further analysis, namely trying to fit existing models to the data, revealed that the molecules can not be in the all-trans configuration. The only interpretation for this is a sulfur dimerisation and a formation of a gauche defect at the first S-C group (Fig. 5.2). It is important to note, that the first conclusion does not contradict the idea of adsorption as thiolates. For this reason, one thiolate structure that is compatible with these findings was taken into account in the simulations. This study at a chain length of n=10 which provides X-ray diffraction pattern will be the main reference for the comparison of the numerical results to the experiment (Section 5.5.2).

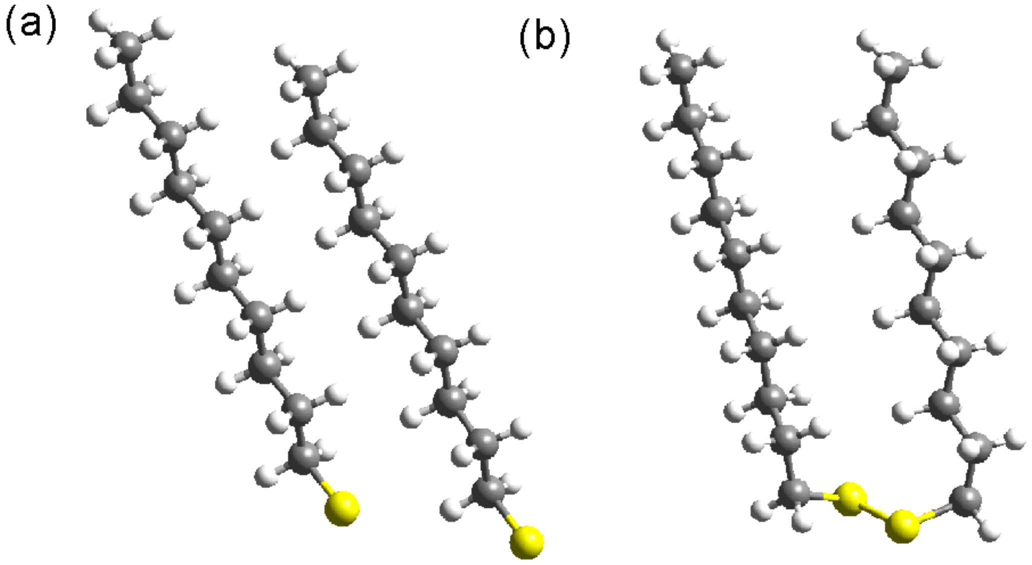

Figure 5.2: Configuration of the chains in the two structural models: In (a) “all-trans” configuration as present in the thiolate model and in (b) “gauche” configuration as in the sulfur-pairing model. The sulfur dimerisations leads to a gauche defect at the S-C bond (apparent in the orientation of the lowest CH_2 group). This ensures an optimal chain packing under the constraint of the small S-S distance.

In the following years the disulfide model was further supported by an X-ray standing waves study from the same group [102] and HREEL (High Resolution Electron Energy Loss) experiments by Kluth *et al.* [103]. In the latter work a vibration at 530 cm^{-1} was observed after annealing of the probe to 375 K. This frequency is very close to the sulfur stretch in liquid dimethyl disulfide at 510 cm^{-1} and it was assigned to a S-S stretch after ruling out other possible stretches (e.g. from hydrocarbons or a combination of gold, sulfur and carbon atoms). At lower annealing temperatures this feature did not appear in the spectra. The interpretation of the authors is that at room temperature the chains adsorb in a non-equilibrium configuration, probably as thiolates. At this point the formation of a gauche defect is energetically unfavourable. Further annealing leads to partial desorption of the chains and thus steric restraints to gauche defect formation are reduced. Annealing to 375 K is needed to overcome the activation barrier to formation of gauche defects and sulfur dimerisation. However, another explanation could be, that before complete desorption there are still some desorbed chains that couple and cause this feature in the spectrum.

Coexistently, there is also strong experimental support for the thiolate model. Already in 1987 Nuzzo *et al.* [96] concluded the dissociation of the S-S bond in adsorbed dimethyl disulfide based on the large core level shift (2.1 eV) in XPS (X-ray Photoelectron Spectroscopy) and the lack of a clear evidence for a disulfide stretch in HREELS. An XPS study at high resolution on the sulfur 2p core level by Heister *et al.* [104] confirmed the existence of only one sulfur species. Interestingly, the data also indicated a small non-equivalence of the adsorption sites what makes the findings consistent with the $c(4 \times 2)$ unit mesh.

Ishida *et al.* [105] provided an evidence for the cleavage of disulfides on Au(111). They synthesised an asymmetric disulfide with hydrocarbon and fluorocarbon chains and observed phase separated domains. The phase separation shows the cleavage of the S-S bond of the disulfide in the film. However, the effect of the introduction of fluorocarbon chains in the monolayer is not clear. The substitution of hydrogen by fluor leads to a chain-chain interaction different from the one in the system of interest (C10/Au(111)) and may lead to results that cannot be generalised.

Last year a measurement of the conductivity through alkanethiol chains yield the same intensity over thousands of molecules [106]. This contradicts obviously the idea of having two chemically different sulfur species in the system.

Very recent an instructive HREELS study examining SAMs of different chain length (n=2-18) was published [107]. Multiple Au-S stretching modes were observed for several alkanethiol SAMs indicating multiple adsorption sites. The authors propose a more complex structure of the interface, also depending on the chain length, than generally believed. For the discussion of the adsorption state even more important, no S-S stretching mode was observed in any spectra what strongly indicates that the S-S bond in not stable on Au surfaces.

Further interesting information for the discussion of thiolate vs. disulfide adsorption was provided by the following studies. In a recent STM study [108] it was reported that the $\sqrt{3} \times \sqrt{3}R30°$ and the $c(4 \times 2)$ structure can coexist.

An SFG (Sum-Frequency-Generation) study by Yeganeh *et al.* [109] yield that the sulfur atoms cannot be situated at sites of a single type. Instead they have to be located e.g. at two different hollow or bridge sites or in a mixed arrangement. Furthermore they reported that the known $\sqrt{3} \times 23$ reconstruction of the Au(111) surface [110] disappears upon alkanethiol adsorption.

Zerulla *et al.* [111] performed XPS measurements to study the X-ray induced damage of SAMs. With increasing exposure to X-ray an additional peak structure appeared on the high binding energy side of the common S 2p doublet. This was considered to be evidence for the appearance of another sulfur species due to X-ray exposure. Further analysis revealed the disulfidic character of that species. It was concluded that the disulfide component appears as a result of radiation induced effects only and was not present on the surface before X-ray exposure. Moreover, it is stated that the way Fenter *et al.* [94,102] ruled out radiation damage is not valid or must at least be reconsidered.

There is some information on the chain length dependence of the structure. Besides the data from HREELS [107] already discussed, an X-ray study by Fenter *et al.* [100] reported distinct short ($n \leq$14) and long ($n \geq$16) chain-length regimes. An extensive study by the same authors including n-alkyl thiol molecules from n=10-30 showed distinct differences of the tilt angle (33° respectively 31°) and the precession angle (15 respectively 8°) between the short chain and the long-chain regime [112]. The longer the chains, the closer the SAM structure is to the bulk alkane structure.

There may be several reasons for the contradicting experimental results. Generally the adsorption state is difficult to investigate since there is no direct access to the headgroup due to the presence of the hydrocarbon chains. In addition, results may be crucially influenced by the quality of the monolayers, the use of different solvents and the way the annealing was realised.

In conclusion, despite a large number of experiments and a wide range of techniques used, there is still no agreement on the adsorption state. As discussed, the interpretation of experimental data is delicate and may be biased by various factors. Considering this experimental situation the subject is a challenging and well-defined problem for theoretical investigations.

5.3 Previous Theoretical Studies

The theoretical studies carried out up to the present can be divided into two classes. On the one hand there are the classical simulations which have the advantage that large parts of the configurational space are accessible but they are lacking the accuracy that is necessary to make statements on the energetical ordering of different monolayer configurations. On the other hand a series of *ab initio* calculations were performed where up to now only SAMs at short chain length were studied.

For a better understanding of the theoretical results presented here it is useful to clarify the terms used to describe the sulfur adsorption site on the Au(111) surface. The terms "atop" site, "bridge" site and fcc respectively hcp "hollow" sites are explained in Fig. 5.3.

One of the first theoretical approaches [113] to the system under consideration is the work by Hautman and Klein. In a very simple model the hydrocarbon groups are represented by single interaction sites ("united atom model"). The bonding distances (S-C and C-C) were constrained to a constant value. In addition bending and torsional potentials were introduced. Long-range interactions are described by Lennard-Jones potentials with parameters taken from Jorgensen [114]. For the S-S interactions larger core sizes were chosen to restrict the lateral mobility of the sulfur atoms and therefore approximate the effect of chemisorption to a fixed surface site. For the modelling of the molecule-surface-potential $V(z)$ a 12-3 form form was applied for the CH_2-surface and sulfur-surface interactions. For the sulfur binding energy an estimate was made from thermal desorption measurements for dimethyl disulfides on Au(111) which yield a heat of adsorption of 28 kcal/mol. The curvature at the potential minimum was adjusted to the 235 cm^{-1} peak observed in electron energy loss spectroscopy that is attributed to the Au-S stretch from the surface thiolate. The position of the minimum was set

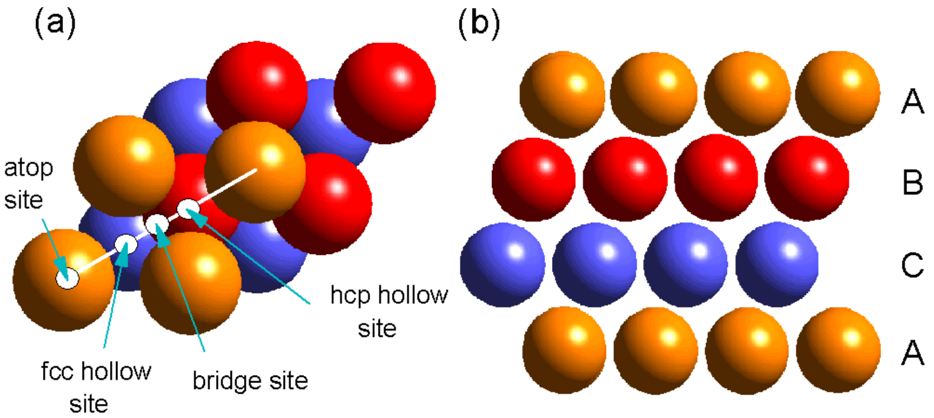

Figure 5.3: Illustration of different adsorption sites on the Au(111) surface. In (a) the atop site (atop of an Au atom in the top layer), the hcp and fcc hollow sites (above an Au atom of the second respectively third Au layer) and the bridge site (between two Au atoms of the top layer) is indicated. In (b) the ABCA stacking of the gold surface is displayed.

.

to 2.4 Å which is a typical length for sulfur-metal bonds in molecules. In this model the angle of the S-C-bond relative to the surface model is unrestricted. In a second model an additional bending potential was introduced that causes the S-C bond to lie roughly in the plane of the surface.

In a subsequent study by Mar and Klein [115] the model was refined and a full atomic representation of methyl and methylene groups was used. In addition a lateral corrugation potential with a large diffusion barrier was used to restrict the atoms to 3-fold-hollow sites. The magnitude of this corrugation was chosen more or less arbitrarily, so that the barrier was 30% of the adsorption well depth. No explicit surface relaxation was allowed in the model. Molecular dynamics simulations of alkanethiol chains of the length n=16 were carried out with 90 respectively 100 chains in the simulation cell. Different properties like the gauche defect concentration as a function of bond number, density profiles, tilt angles (decreases to about 10° at 400K), twist angle distributions and rotational correlation functions were monitored (for the explanation of these angles see Section 5.5.2). A schematic phase diagram was suggested with the system in the crystalline phase below 300 K, a gradual untilt between 300 and 370 K and free rotating chains above 370 K with gauche defects formed throughout the film. As the most favourable structure they found a herringbone structure with two molecules per unit cell. The structure of the SAMs showed a tilt in the next-nearest-neighbour direction, an average twist angle of 50° and a tilt angle of about 30° at room temperature. All structures consisting of four chains per unit cell considered were at least 1 kcal/mol higher in energy. In conclusion the authors suggest that "more work needs to be done in refining the treatment of the substrate".

A different approach that in contrast to the work by Klein lay stress on the mobility of the sulfur headgroups and a non-rigid gold surface was taken by Bhatia *et al.* [116]. In this study the surface was modelled by eight layers of Au atoms of which the first three layers were allowed to move according to Newton's equations of motions and the bottom-most layer was kept fixed. The intermediate layer are treated as heat bath using the generalised Langevin equations so the whole system could be maintained at desired temperatures. The Au atoms are described by many-body effective medium potentials. The CH_x units were treated within the united-atom model and the same parameters as in the first work by Klein were used. For the Au-S a Morse potential was applied deduced from the QM calculations by Sellers [117], for the Au-CH_x interactions a Lennard-Jones potential was used. A systematic study of the phase-space of the orientations of the chain backbones and their tilt was performed. Three criteria were applied to decide whether a structure is a good candidate for the $c(4\times2)$ superstructure. The obtained structures were compared to STM [101], and X-ray diffraction [94] data and as the third criterion the relative energy of the configuration was checked. In total four structures for short (n=4,6) and long (n=12) chains were proposed of which all satisfied the X-ray criterion but only two showed the correct height profile compared to the STM measurements.

Pertsin *et al.* [118] focused completely on static calculations since they believed that the role of thermal effects in the monolayer is insignificant. This idea is based on the findings of Camillone *et al.* [98,99] that did not observe a structural transition on cooling down to at least 30 K. The same potentials and parameters as in the second Klein study were used whereby additional variants for the sulfur-gold interaction were tried (resulting in four sets of parameters). The configurational space was systematically searched by combining the methods of global stochastic search and local minimisation. The result of this study is that the alkanethiol gold monolayer system is much richer in low-energy minima than found in previous computer simulations. Depending on the force field a total number of up to 22 configurations was found in a 1 kcal/mol window. However, neither of the four force fields predicted a four-chain unit cell structure.

The work of Gerdy *et al.* is special since they assumed that the sulfur headgroups exist as dimers on the surface. The S-S dihedral potential was taken from a QM study of diethyl disulfide. Furthermore, they expected the S atoms to bind to 3 fold-hollow sites on the surface which was incorporated by using a bond interaction from each sulfur atom to a gold atom one layer down from the surface. The X-ray diffraction pattern of the optimised structure was calculated and compared to the experimental data from [94]. The calculated intensities are in very good agreement with experiment. However, the tilt angle of the alkanethiols in the simulation is 28° what differs significantly from the experimental value (see Tab. 5.4).

In summary, the classical simulations carried out so far suggest that a large number of low-energy configurations exist but none of the studies was able to present a structure that is in full agreement with experiment. A major problem of some of the studies presented, is the use of force field parameters of doubtable quality. In particular the parameters provided by Sellers *et al.* [117] are most likely to be wrong as will be discussed in the following.

The first quantum mechanical studies were based on very simple cluster models [117, 119]. Here, two-layer clusters were used to represent the gold surface with the atoms fixed in the positions of the bulk atoms. In Sellers work [117] the gold cluster consisted of 17 atoms, of which eight were treated quantum mechanically and the others were classical objects. The method used was Hartree-Fock plus correlation treated at the second order of perturbation theory.

In Ref. [119] the two-layer cluster consisted also of 17 atoms (10+7), SCH_3 was kept in the gas-phase geometry of $HSCH_3$, but the S-Au distance and the C-S-Au angle were varied. The failure of these approaches was demonstrated [120] by comparing more sophisticated surface models to the oversimplified cluster models. The limitation of these calculations is that of not allowing the surface to relax as a consequence of adsorption.

In the last two years a series of density functional theory based studies [43,121–124] were published that used a slab of gold atoms to model the surface. The first of these studies was the one by Grönbeck and co-workers [43] in which the adsorption of methanethiol and dimethyl disulfide on Au(111) at low coverage ($\Theta = 0.24$) was studied (see Fig. 5.4). The surface was modelled as a slab consisting of four 5×5 layers (further details in Section 5.4). It was found that thiolate adsorption is favoured over disulfide adsorption by 11 kcal/mol per chain. The preferential site of the sulfur atoms is the fcc hollow site (see Fig. 5.3). Another important result of this study

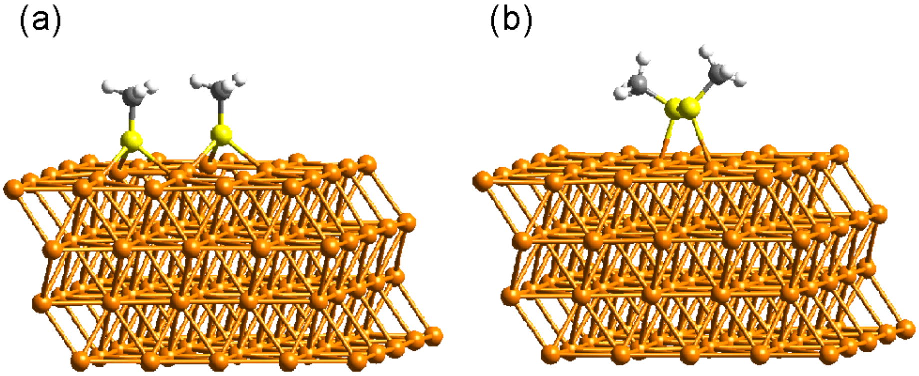

Figure 5.4: Side view of equilibrium structures at low coverage and short chain length: (a) 2 CH_3S/Au(111), (b) H_3CSSCH_3. Au atoms are shown in orange, C atoms in white, S atoms in yellow, H atoms in grey. The geometries are taken from [43]

.

was the evaluation of the performance of different exchange-correlation functionals (PBE [18], BLYP [19,20] and LDA [16,17]). Comparisons to experimental data of the bare gold surface and organic molecules demonstrated that the PBE functional is best suited for the investigation of self-assembled monolayers. This chapter of the thesis can be considered as the continuation of this work, extending the system to the full coverage regime and longer hydrocarbon chains. Some methods were adopted from that work, others were added (see Section 5.4 to account for the change in coverage and chain length).

Vargas *et al.* [121] studied the same system (n=1) as a function of coverage Θ. The PW91 functional was used and the slab contained four layers of gold atoms. They report higher stability for thiolates than for disulfides with the bridge site to be the most stable at all coverages. At full coverage, simulations of the $\sqrt{3} \times \sqrt{3}R30°$ and the $c(4 \times 2)$ structures resulted in similar energies.

In the study by Hayashi *et al.* [123] three different coverage regimes were simulated (n=1) with a four-layer slab in the PBE functional. They conclude that the S-S bond dimethyl disulfide is cleaved in the most stable adsorption site and adsorption as thiolates takes place at bridge sites slightly off-centred to the hollow site. This structural model agrees well with experimental HREEL spectra.

A first step regarding the influence of the chain length was taken by Yourdshahyan *et al.* [122]. Here, investigations of chain length (n=1,2,3,7) and coverage showed that the fcc site is more stable than the hcp site in all cases and the bridge site being even higher in energy. However, this approach to treat the whole hydrocarbon chain in DFT is highly doubtable. The interaction between the hydrocarbon chains are governed by van-der-Waals interaction and the deficiencies of DFT to describe these interactions are well known (see e.g. [125], [126], more details in Section 5.4). It can therefore not be expected that these results are reliable.

The clear drawback of quantum simulations is the lack of DFT to describe van-der-Waals interactions accurately. Hence, an appropriate description of the important chain-chain interactions is missing. This restricts QM simulations of SAMs to very short chains (n=1) where van-der-Waals interactions are weak. On the other hand classical simulations provide a good implementation of this force type but lack an accurate modelling of the formation of chemical bonds, as in the sulfur adsorption on gold since they depend on empirical parameters.

In conclusion, no study exists with an appropriate description of adsorbate-surface and chain-chain interactions at the same time. Therefore there is a clear lack of information concerning the preference of thiolate or disulfide adsorption in the long chain regime. There seems to be urgent need for a new theoretical approach to self-assembled monolayers.

5.4 Methods

The overview of recent theoretical works gives a strong motivation to develop new methods to tackle the problem of thiolate vs. disulfide adsorption. For the best possible modelling of an organo-sulfur monolayer it is indispensable to exploit techniques from the classical and the quantum world. The idea is to combine classical and quantum methods and apply each of them to the part of the system where it ensures a reliable modelling.

In this chapter a combined QM / MM approach ("hybrid approach") is presented that exploits DFT and classical force fields at the same time. It is the first approach to self-assembled monolayers of this kind and it satisfies all requirements to obtain meaningful results.

The purpose of of combined QM/MM study is usually to reduce computational cost but still remaining on a high level of accuracy. On the one hand the quantum part should be chosen as large as possible for the sake of accuracy on the other hand the computational effort in DFT scales by roughly N^3 (N number of electrons) in the standard implementation that limits DFT calculations to systems of about ~ 1000 atoms. A compromise has to be found to satisfy both requirements.

For the system of self-assembled monolayers the situation is different. In this case a significant contribution to the total energy is caused by dispersive forces between the hydrocarbon chains. Hydrocarbons do do not posses permanent electric dipole moments and therefore electrostatic interactions are negligible. Still, there is an attractive force between the molecules that is caused by the induction of dipoles in non-polar molecules due to the presence of other molecules. Since these forces depend on the atomic polarisabilities they are referred to as dispersive van-der-Waals forces. The description of this type of interaction is problematic in DFT. For shorter distances the description of van-der-Waals forces is still satisfying but it fails for larger distances. The problem is that a local xc-functional is not capable of describing the attraction due to dispersion, because this interaction is a long-range non-local correlation effect.

There are popular examples that illustrate the deficiencies in the description of condensed soft matter. The performance of DFT for crystalline polyethylene was studied by Montanari *et al.* [125]. No exchange-correlation functional was able to produce satisfying results. In LDA the strength of the intermolecular bonds was overestimated whereas in PBE the interchain separation was 12% greater than in experiment. In another study Meijer *et al.* [126] found no cohesion for bulk benzene in gradient-corrected xc-functionals. Even after adding dispersion energy from an empirical model the error in the cohesive energy and the bulk modulus was still 25%.

It is therefore not advisable to treat the complete system including the chains in DFT and would lead to wrong results. The solution to this problem is to separate the system into a quantum and a classical fragment. The headgroup-surface interaction is treated in DFT and the chain-chain interactions are modelled using a classical force field that allows the accurate calculation of interchain forces.

The division of the system into a quantum and a classical region is illustrated in Fig. 5.5(a). The best position for the separation is after the first CH_2 unit of the alkanethiol chains. A cleavage directly after the sulfur atom would lead to unphysical results since the carbon atom closest to the surface (and its bonded hydrogen atoms) play a significant role in the surface-adsorbate interaction. If more hydrocarbon units were considered in the QM part the problems discussed above would arise and accuracy would be lost. Therefore only the gold surface and the sulfur-headgroup (SCH_3) are treated in DFT.

The detailed modelling of the quantum region will be explained in Section 5.4.1. The implementation of the classical interaction and the coupling between the QM and MM fragments will be described in Section 5.4.2 respectively 5.4.3.

5.4.1 The quantum part

As mentioned in Section 5.3 this study of the full-coverage regime is based on the low-coverage study by Grönbeck *et al.* [43]. It provides useful information about the surface modelling and the choice of the exchange-correlation functional.

However, the different coverage regime under study calls for a different surface model. The gold surface is now described as a slab consisting of four layers with 48 atoms per layer (6×8) in an orthorhombic supercell, corresponding to a total number of 192 gold atoms. This size of the supercell corresponds to 16 $\sqrt{3} \times \sqrt{3}R30^\circ$ unit

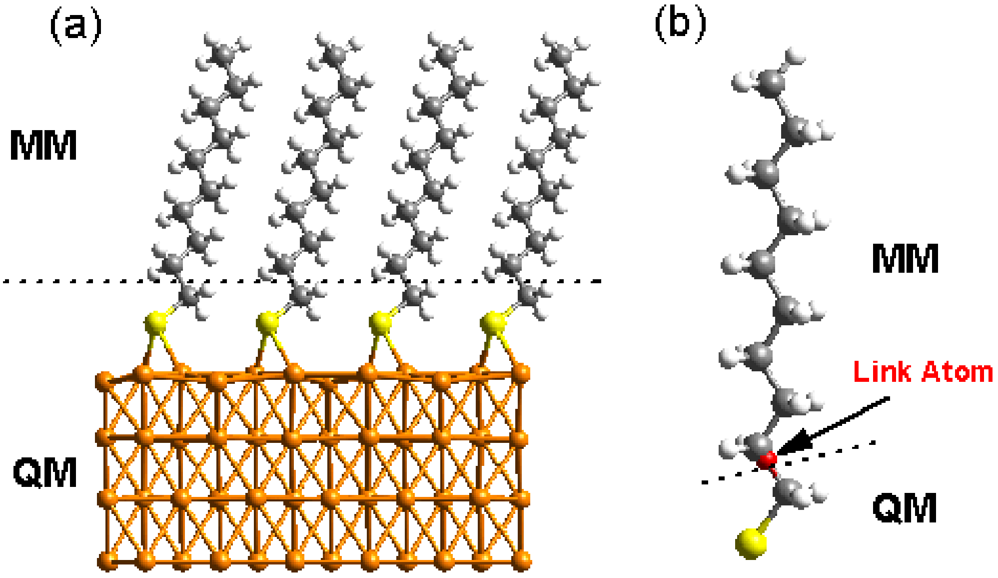

Figure 5.5: Illustration of the QM/MM approach. In (a) the separation of the system into a quantum (QM) and classical (MM) fragment is shown. In Figure (b) the position of the link atom (red) is marked. It is treated quantum mechanically as the surface and the first CH_2 group.

cells or four $c(4 \times 2)$ unit cells (cf. Fig. 5.1.) In Grönbecks work the supercell was chosen to be hexagonal as the original symmetry of the Au(111) surface. However, the symmetry of the experimentally observed $c(4 \times 2)$ supercell at full coverage made it necessary to change to an orthogonal supercell. The $c(4 \times 2)$ cell is a superstructure of the $\sqrt{3} \times \sqrt{3}R30^\circ$ and thus both systems can be studied in this supercell. Note that the large size of the supercell is important because only in this way relaxations in the surface upon adsorption can be described. The lattice constant used in the simulations was taken from a gold bulk calculation [43] in the PBE functional (d = 4.15Å). It agrees reasonably well with the experimental value d_{exp} = 4.06Å. The surface modelling as described here does not account for the known $\sqrt{3} \times 23$ reconstruction of the Au(111) surface. However, it was reported [109] that the reconstruction disappears upon alkanethiol adsorption. In the optimisation of the adsorbate-metal complex the atoms of the alkanethiol chains and the top three layers of the Au surface are free to relax whereas the fourth layer atoms are kept fixed in their bulk positions. Since periodic boundary conditions are applied, a vacuum space of ∼ 12 Å is introduced in z-direction (direction of surface normal) to avoid interactions of the system with its periodic images in this direction. The exact dimensions of the supercell are $17.62 \times 20.35 \times 19.21$Å. The reliability of the slab model was checked against experiment in terms of surface energy and the position of the surface states in the electronic density of states [120].

The choice of the exchange-correlation functional is crucial since the quality of the results can depend strongly on the functional. Generally, the BLYP approximation is known to provide a good description of molecular systems, whereas PBE is expected to account better for systems in which homogenous and dishomogenous electron densities coexist. This trend was confirmed [127] in test calculations that revealed slightly better performance for organic molecules in BLYP but on the other side, PBE proved to reproduce the properties of the bare and adsorbed gold surface much better. That work showed that the PBE functional [18] is suited the best for an appropriate modelling of CH_3 adsorption on gold.

The pseudopotential for Au and H is the same as in the study of Au_nH (for details see Section 3.2). For sulfur, the cut-off radii were chosen to 1.5 Bohr for the *s*, *p* and *d* potentials. The ground state configuration (s^2p^4) was used for *s* and *p* potentials, and for the *d*-potential $s^1p^{2.75}d^{0.25}$ was used. For carbon *s* and *p* potentials were generated at the ground state electronic configuration (s^2p^2) with a cut-off radii of 1.2 Bohr for both channels. The quality of the pseudopotentials used here was checked carefully in the former studies [43, 49]. The valence wave functions are expanded in plane waves up to a kinetic energy cutoff of 50 Rydberg.

5.4.2 The classical part

For an accurate modelling of the interchain forces a reliable force field is needed that can account for the special chemical environment of the system. In the case of organic monolayers force field parameters are desirable that were obtained on the basis of condensed organic materials. The force field developed by Goddard [128], is based on data for C_4H_{10} (valence interactions) and the polyethylene crystal (non-bond interactions) and provides parameters for carbon and hydrogen atoms. It ensures an excellent description of the chain-chain interactions as it was shown in [129] where the application of this force field reproduced the properties of the polyethylene crystal accurately. The energy expression involves valence (E_{val}) and non-bond (E_{nb}) interactions

$$E = E_{\mathrm{val}} + E_{\mathrm{nb}} \,. \tag{5.2}$$

The valence interactions include the terms arising from covalent bond formation, including bond stretch E_{b}, angle bend E_{a} and dihedral angle torsion E_{t}:

$$E_{\mathrm{val}} = E_{\mathrm{b}} + E_{\mathrm{a}} + E_{\mathrm{t}} \,. \tag{5.3}$$

The non-bond interactions consist of van-der-Waals (E_{vdW}) and electrostatic forces (E_{Q}).

$$E_{\mathrm{nb}} = E_{\mathrm{vdW}} + E_{\mathrm{Q}} \,. \tag{5.4}$$

The bonded interactions are described by using the following expressions:

$$\text{Morse terms: } E_{\mathrm{IJ}} = D_{\mathrm{b}}[e^{-\alpha_{\mathrm{b}}(R-R_{\mathrm{b}})} - 1]^2 \,, \tag{5.5}$$

where R is the length of bond IJ, R_{b} and D_{b} are the position and depth of the well, and $k_{\mathrm{b}} = 2D_{\mathrm{b}}\alpha_{\mathrm{b}}^2$ is the force constant,

$$\text{Cosine angle-bond terms: } E_{\mathrm{a}} = 1/2C[\cos\Theta - \cos\Theta_{\mathrm{a}}]^2 \,, \tag{5.6}$$

where Θ is the angle between bonds IJ and JK, Θ_{a} is the equilibrium angle, and $k_\Theta = C\sin^2\Theta_{\mathrm{a}}$ is the diagonal force constant,

$$\text{Threefold torsion terms: } E_{\mathrm{t}} = 1/2V_{\mathrm{t}}(1 + \cos 3\phi) \,, \tag{5.7}$$

where ϕ is the torsional angle for bonds IJ, JK, and KL and V_t is the barrier.

The van-der-Waals part of the non-bond interaction for atoms I and J is described by using the exponential-6 potential:

$$E_\mathrm{vdW} = Ae^{-BR_{IJ}} - \frac{C}{R_{IJ}^6} = \frac{D_\mathrm{v}}{\xi - 6}\left[6e^{\xi(1-\rho)} - \xi\rho^{-6}\right] . \tag{5.8}$$

where $\rho = R_{IJ}/R_\mathrm{v}$. For the interactions involving sulfur atoms the DREIDING force field [130] was used. This is a more general but well-tested force field in contrast to the specialised force field used for the hydrocarbon interactions. The non-bond interactions between nearest and next-nearest neighbours were excluded as it is a common practice. This means that for a contribution to the non-bond energy the two interacting atoms must be separated by at least two bonds. The contribution of electrostatic interactions to the total energy is negligible due to the small dipole moments of the participating atoms (see also [129]) and therefore E_Q was set to zero. Using this approximation the force field takes the same form as the one used by Gerdy *et al.* [129] applied in a fully classical study on the structure of SAMs.

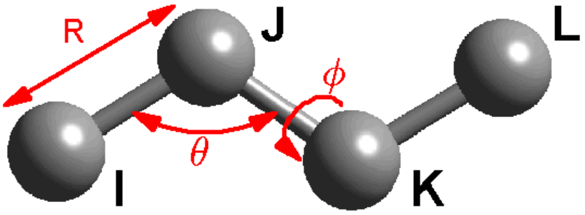

Figure 5.6: Illustration of the parameters as used in the force field: the length R of bond IJ, the angle Θ between bonds IJ and JK and the torsional angle ϕ for bonds IJ, JK, and KL.

5.4.3 QM / MM coupling

In the last two sections the modelling of the quantum and the classical part was discussed. In the following, it will be explained how these fragments are matched and how they are coupled to each other.

As shown in Fig. 5.5(a), the separation of the system in a QM and MM region necessitates the cleavage of chemical bonds. The cleavage of C-C bonds in hydrocarbon chains is rather straight forward because it is an unpolar bonds and therefore Coulomb interactions between the fragments are small. However, it leads to a dangling bond that has to be saturated in a sensible manner. Probably the most widely used technique is the introduction of an additional hydrogen atom in the system that is bonded to the carbon atom treated in DFT (for a comparison of different techniques see e.g. [131]). This atom (also called “link atom”) links the QM and the MM fragments. Since it is introduced artificially into the system care must be taken to minimise artefacts. A sophisticated solution to this problem was used to ensure this goal. In this approach the link atom is constrained on the line connecting the DFT carbon atom and the first carbon atom of the classical part (see Fig. 5.5(b)). Beyond this common level of QM/MM coupling ("mechanical coupling") the distance of the link atom to the quantum carbon atom r_{CH} is scaled such that the stretching force of the C-H bond closely approximates that of the C-C bond between the quantum carbon atom and the first classical carbon atom:

$$r_{\mathrm{CH}} = r^0_{\mathrm{CH}} + \frac{k_{\mathrm{CC}}}{k_{\mathrm{CH}}}(r_{\mathrm{CC}} - r^0_{\mathrm{CC}}) \,, \tag{5.9}$$

where r^0_{CH} and r^0_{CC} are the equilibrium C-H respectively C-C bond length, and k_{CC} and k_{CH} are force constants of the corresponding bond stretches. This approach is known as SPLAM ("Scaled Position Link Atom Method") method and was suggested by Eichinger *et al.* [132]. One of its main advantages is that it allows the classical part to couple to the wavefunction of the QM part. This is in contrast to the method used widely where the $\mathrm{C_{QM}}$-$\mathrm{H_{LinkAtom}}$ distance is kept fixed at the equilibrium C-H distance during the simulation. In the study presented here, the equilibrium bond length were taken from a DFT calculation of $\mathrm{HSC_3H_7}$ and the force constants from the DREIDING force field [130].

In addition to this coupling interactions between atoms from the QM and MM part are implemented using the classical force field discussed in Section 5.4.2. It includes all the interactions where at least one atom from each segment is involved. The interactions between the classical atoms and the gold surface were neglected. This interaction would become of interest in the low coverage regime at long chain lengths. Under these conditions experiments showed that the chains do not stand upright but lie flat on the surface stabilised by van-der-Waals forces between the gold atoms and the hydrocarbon chain. For the scenario studied here this interaction is not of importance.

In order to apply the presented QM/MM approach to self-assembled monolayers, it was necessary to implement the classical force field and the coupling between the quantum and the classical atoms into the existing DFT code [21]. The code is now able to handle organosulfur chains of varying length n in the full coverage regime. A range of alkanethiol configurations at different chain lengths was setup and searches for minima of the potential energy were performed. These geometry optimisations therefore correspond to 0 K simulations. The structures were considered to be in a minimum of the potential energy surface when the highest gradient on any degree of freedom was less than 5×10^{-4} Hartree/Bohr. A very efficient optimisation was achieved due to the application of a recently developed linear scaling optimisation scheme [133].

5.5 Results and Discussion

The goal of the first part of the study was to get insight into the puzzle of the adsorption state in a self-assembled monolayer of decanethiol (n=10) at full coverage. For this purpose in total four different configurations were setup and local geometry optimisations performed on these systems. Three thiolate configurations and one disulfide configuration were taken into account. Two of the thiolate configurations were consistent with the $\sqrt{3} \times \sqrt{3}R30^\circ$ unit mesh (1 chain per unit cell). The sulfur atoms were located in fcc respectively hcp hollow sites bonded to three gold atoms of the first layer. This initial configuration was chosen based on the results at low coverage (n=1) that revealed adsorption in the hollow site (see Fig. 5.4(a)). The difference between the fcc and the hcp configuration is that the sulfur atoms are located atop of a gold atom of the third respectively second layer (see Fig. 5.3). The third thiolate configuration consists of four chains per unit cell and is consistent with the $c(4 \times 2)$ unit mesh. The initial sulfur atom positions for the disulfide system correspond to the structure suggested by Fenter *et al.* [102].

The optimisation of the atomic configuration during the search for a local minimum on the potential energy surface resulted in a significant rearrangement of the sulfur atoms and the hydrocarbon chains. The sulfur atoms in both thiolate configurations (fcc and hcp) with one chain per unit cell moved to the bridge position (Fig. 5.7(a)). For this reason there will be no distinction between fcc and hcp structure in the following and the configuration will be referred to as thiolate "1 chain model". A close inspection of the geometry reveals that the S atoms do not sit in the ideal bridge position. Instead they are slightly off-centred by Δs=0.30 Å (see Tab. 5.1) towards the hollow site.

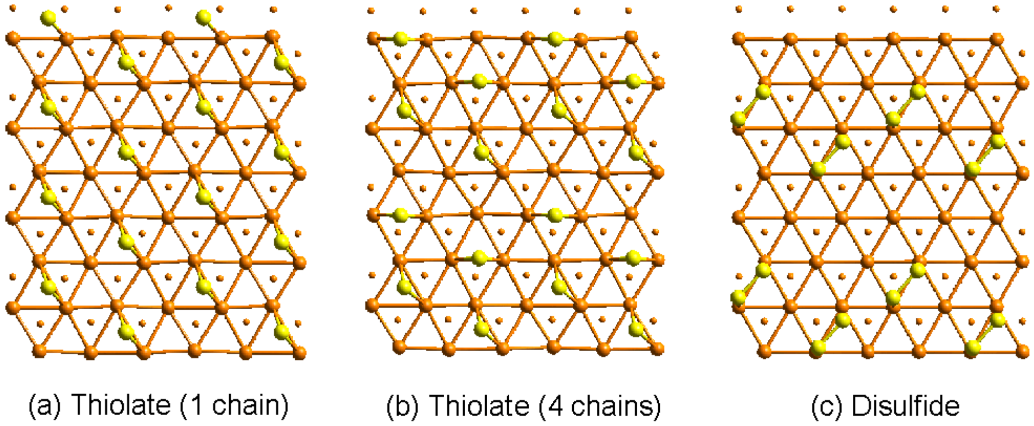
(a) Thiolate (1 chain) (b) Thiolate (4 chains) (c) Disulfide

Figure 5.7: Optimised geometries for different C10/Au(111) configurations: Top view of the thiolate "1 chain" ($\sqrt{3} \times \sqrt{3}R30°$ unit cell) and "4 chain" ($c(4 \times 2)$ unit cell) model, and the disulfide model in their optimised geometries. Only the position of the sulfur (yellow) and the top two layers (big and small orange balls) of the gold surface are drawn.

In the thiolate "4 chain model" the sulfur atoms occupy non-equivalent sites. Two of the four sulfur atoms in the unit cell are located in ideal bridge position, the two others are rather off-centred towards the fcc hollow site. Note that in the initial configuration all sulfur species were setup in equivalent positions only differing in the chain orientation. The exact sulfur positions as given in Tab. 5.1 reveal that strictly speaking all S are non-equivalent. The atoms in "ideal" bridge position are slightly off-centred by 0.03 respectively 0.11 Å, the two other S atoms are off-centred by 0.47 respectively 0.54 Å.

The sulfur atoms reside ∼2.05 Å above the gold surface in the "1 chain model" whereas in the "4 chain model" the sulfurs are slightly further apart from the surface with Δz ranging from 2.06-2.13 Å.

Also in the disulfide model a significant movement away from the initial geometry was observed. The system was setup with two sulfur atoms closer to the surface in atop position and two situated between atop and fcc hollow site, further away from the surface. This configuration corresponds to the structural model as suggested in Ref. [102]. During the course of the geometry optimisation the atoms closer to the surface relaxed to a position 0.28 respectively 0.54 Å off the atop site. One of the two other sulfur species is close to the hollow site (Δs=0.78 Å), whereas the other is closer to the atop site (Δs=0.51 Å). The adsorption in atop site causes a much larger sulfur-surface distance Δz, namely 2.80 respectively 2.88 Å, compared to the adsorption in bridge site (Δz$\sim$ 2.05 Å).

Model	n	S1		S2		S3		S4	
		Δz	Δs	Δz	Δs	Δz	Δs	Δz	Δs
Thiolate (1 chain)	10	2.04	0.30B	2.04	0.30B	2.06	0.30B	2.06	0.30B
Thiolate (4 chains)	10	2.06	0.03B	2.08	0.54B	2.08	0.47B	2.13	0.11B
Disulfide	10	2.80	0.54A	2.88	0.28A	3.00	0.51A	3.06	0.78A
Thiolate (1 chain)	4	2.04	0.29B	2.04	0.29B	2.06	0.29B	2.06	0.29B
Thiolate (4 chains)	4	2.03	0.03B	2.00	0.55B	2.09	0.44B	2.12	0.09B
Disulfide	4	2.76	0.51A	2.89	0.23A	2.94	0.54A	2.98	0.79A

Table 5.1: Detailed position of adsorbed sulfur atoms (S1-S4) for all models at chain lengths of n=4 and 10. Δz is the difference in the z-coordinate (direction of surface normal) between the sulfur atom and the average of the first layer gold atoms. Moreover the distances Δs from the S positions relative to the ideal bridge (B) and atop (A) are given in Å. For example, "0.30B" stands for a sulfur atom at the bridge site off-centred by 0.30 Å towards the hollow site. Δz and Δs are given in Å.

After the completion of the calculations at n=10 subsequent calculations at shorter chain length (n=4, butanethiol) were performed in order to illuminate the influence of the chain length on the monolayer structure. As initial geometries the optimised geometries of the previous calculations were taken with the chains shortened to four carbon atoms. To accelerate the finding of a local minimum the structures were preoptimised by fixing the quantum part and relaxing the classical part of the system only. In the thiolate model the structure of the QM part remained in a geometry very similar to the one found at n=10. Almost no relaxations occurred for the "1 chain" model and only small changes in the structure emerged in the "4 chain" model (see Tab. 5.1). A larger relaxation was observed for the disulfide model that resulted in a slightly closer contact ($\sim$ 0.05 Å) of the sulfur species to the surface.

A side view of the optimised geometries for selected systems at n=4 and 10 is shown in Fig. 5.8. The unequal adsorption sites as well as the different chain orientations can be clearly seen. A close look at the gold atoms in the first gold layer even reveals the much more corrugated surface upon thiolate adsorption than for disulfide adsorption. The different degrees of structural relaxation in the two models will be discussed later in this chapter.

In the following three sections an in-depth analysis of the numerical results is presented. In the next section the thiolate and the disulfide model will be compared in terms of the thermodynamical stability. In Section 5.5.2 the structure of the monolayer

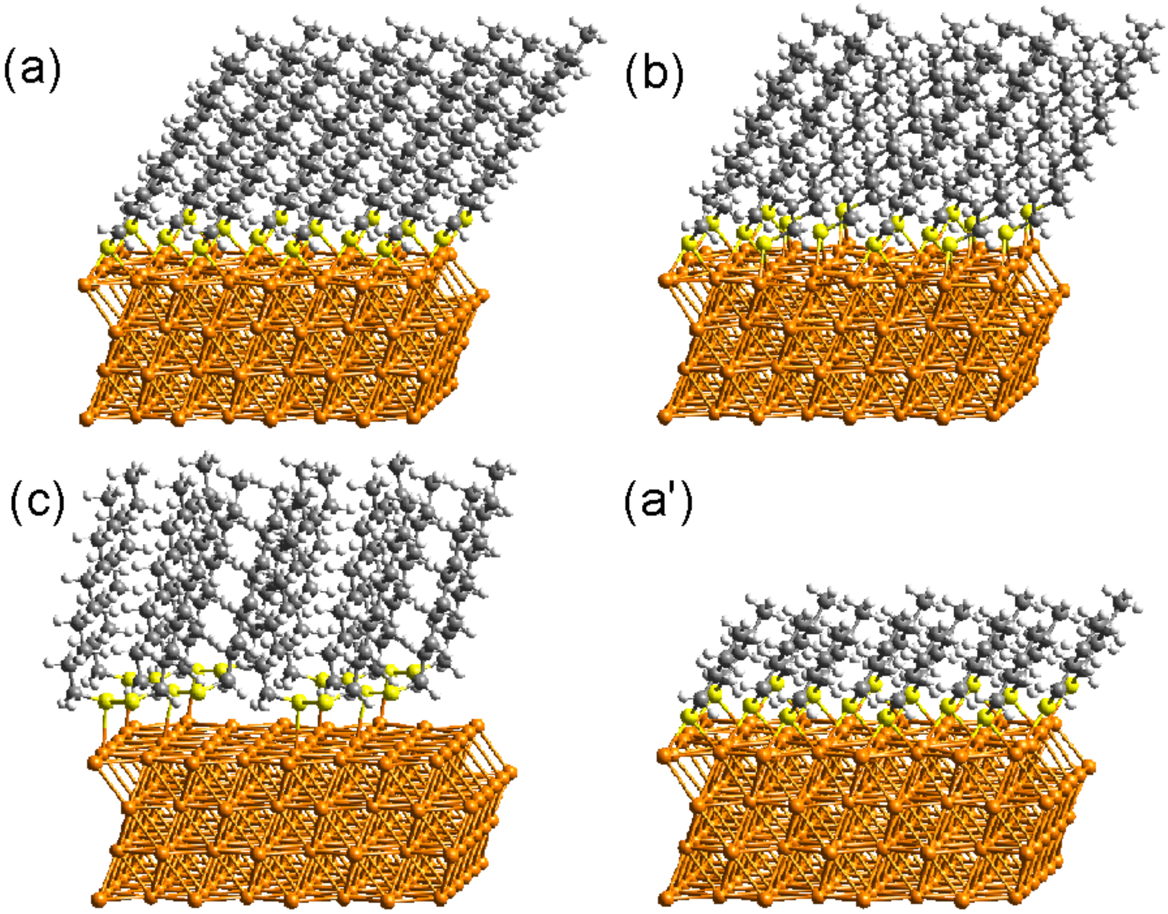

Figure 5.8: Side view of equilibrium structures: (a) Thiolate (1 chain), n=10, (b) Thiolate (4 chains), n=10, (c) Disulfide, n=10 and (a') Thiolate (1 chain), n=4. All atoms included in the simulation are shown (704 atoms at n=10 and 416 atoms at n=4).

will be discussed elaborately. In particular, the data from the QM/MM simulations will be compared to structural information determined experimentally. From the geometries obtained in the simulations the X-ray diffraction patterns and approximate STM images are calculated and compared to the experimental results. Finally, some information on the electronic properties of the system will be given.

5.5.1 Energetics

In this section the energetics of the thiolate model and the disulfide model will be presented in terms of chain length and coverage. In the first part the focus will be on the relative stabilities of the models, in the second part absolute adsorption and cohesive energies will be given.

Relative stabilities

The results of the calculations for n=4 and n=10 in terms of the potential energy E_{tot} are reported in Tab. 5.2. The energy differences per chain relative to the structure with the lowest energy are listed and split into the contribution from the quantum part E_{QM} and the classical part E_{MM}. The latter includes also the energy contribution from the QM/MM coupling. For the sake of comparison the results at low coverage and short chain length from Ref. [43] are given, too. To clarify the sign of the energy differences given, note that the total energies of the different models are negative (corresponding to a bonded state). The energy difference ΔE was calculated according to the formula

$$\Delta E = -(E_{\mathrm{ref}} - E_{\mathrm{model}}) \tag{5.10}$$

with E_{ref} as the energy of the reference model (the model with the lowest energy) and E_{model} as the energy of another model.

Model	n	ΔE_{QM}	ΔE_{MM}	ΔE_{tot}
Thiolate (1 chain)	10	0	0	0
Thiolate (4 chains)	10	1.3	0	1.3
Disulfide	10	5.2	2.8	8.0
Thiolate (1 chain)	4	0	0	0
Thiolate (4 chains)	4	0.6	0	0.6
Disulfide	4	4.8	1.0	5.8
Thiolate (fcc, low cov.)	1	0	-	0
Thiolate (hcp, low cov.)	1	8	-	8
Disulfide (low cov.)	1	11	-	11

Table 5.2: Potential energy of different models with length $n = 10$ and $n = 4$. The energies are in kcal/mol per chain and relative to the structure with the lowest energy. The contributions of the classical and quantum parts are listed separately ($\Delta E_{\mathrm{tot}} = \Delta E_{\mathrm{QM}} + \Delta E_{\mathrm{MM}}$. Adsorption as thiolates is favoured at full coverage for short ($n = 4$) and long ($n = 10$) chains as well as in the low coverage regime ($n = 1$) [43].

The comparison of the energies obtained for the thiolate and the disulfide model reveals that the thiolate model is favoured in terms of the quantum and the classical contribution. The thiolate "1 chain model" is the most favourable configuration. At n=10 it is favoured by ~ 5 kcal/mol per chain in the quantum part and ~ 3 kcal/mol in the classical part summing up to a total energy difference of ~ 8 kcal/mol relative to the disulfide model. This is a considerable energy difference (cf. k_BT(300K)~ 0.5 kcal/mol) and gives strong support to the thiolate model. Entropy effects are expected to be small in highly ordered SAMs and are unlikely to alter these findings. The other thiolate model ("4 chain model") which is consistent with the experimentally observed $c(4 \times 2)$ unit mesh is only slightly higher in energy than the "1 chain model". There is no difference in the classical part and only a slight advantage of ~ 1.3 kcal/mol for the "1 chain model" in the QM part. This small total energy difference is comparable to the accuracy of the DFT method of about 1 kcal/mol. Thus the method applied can not distinguish between the "1 chain" and "4 chain" thiolate model as the ground state. However, this result is in agreement with experimental observations. Firstly, these findings imply a shallow potential energy surface (PES). Considering the formation of SAMs it is clear that a shallow PES is necessary to obtain such perfectly ordered systems. If there was a strong corrugation of the PES the sulfur species would be trapped at their first adsorption site on the surface and result in a monolayer of low order. For the formation of well-ordered monolayers the alkanethiol chains have to be able to hop over the surface until all chains have reached the hexagonal formation with a chain-chain distance of $\sim$ 5 Å. Secondly, STM images [108] revealed the coexistence of $\sqrt{3}\times\sqrt{3}R30°$ and the $c(4\times2)$ phases. This agrees well with the two nearly degenerate structures found here.

The altering of the chain length to n=4 has an impact on the relative stability of the two models. Adsorption as thiolates is still energetically preferred but the disulfide model gained 2 kcal/mol relative to the thiolate model. This is illustrated in Fig. 5.9 in which the thiolate "1 chain" model is compared to the disulfide model. Going from n=10 to n=4 the energy difference is reduced from $\sim$8 kcal/mol to 6 kcal/mol. There is only a slight change in the QM part (red line in Fig. 5.9) which is reasonable since the shortening of the chains leaves the atomic structure at the interface nearly unchanged (Tab. 5.1). The somewhat larger relaxation in the disulfide model may explain the small gain in the QM energy relative to the thiolate model (ΔE_{QM} reduced from 5.2 to 4.8 kcal/mol). More significant is the change in ΔE_{MM}. Still, the formation of the chains in the thiolate model is more favourable than the disulfide model in terms of the chain-chain interactions, but at n=4 the energy difference is reduced to only $\sim$ 1 kcal/mol. To illuminate the chain length dependence further values for ΔE_{MM} were calculated at n=4,6 and 8 with the quantum part fixed in the geometry of n=10 and full relaxation of the classical part. Following this procedure the value found at n=4

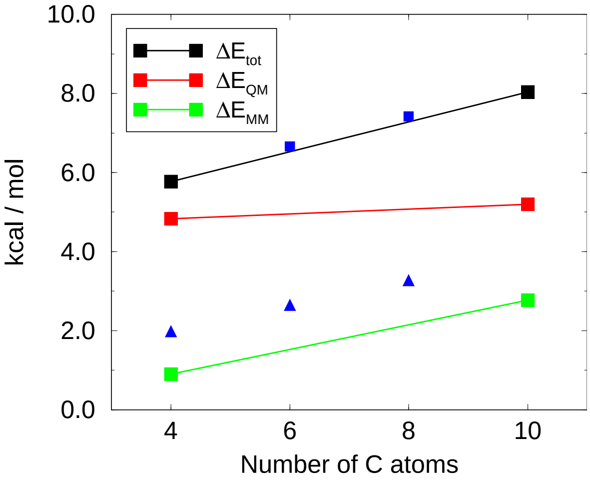

Figure 5.9: Comparison of the thermodynamical stability between the thiolate "1 chain" and the disulfide model in terms of chain length. The total energy difference ΔE = E(Thiolate) − E(Disulfide) is given. Additionally the classical and quantum mechanical contributions of $\Delta E_{\mathrm{tot}} = \Delta E_{\mathrm{QM}} + \Delta E_{\mathrm{MM}}$ are plotted. The blue triangles indicate ΔE_{MM} at n=4,6 and 8 with the quantum part in the geometry of n=10. Based on this data and accounting for geometry relaxation by using the values calculated explicitly at n=4 the blue squares indicate the extrapolated ΔE_{tot} at intermediate chain lengths n=6 and 8.

indicates a 1 kcal/mol larger energy difference (2 kcal/mol vs. 1 kcal/mol) than for the case when the QM part is also allowed to relax as in the QM/MM calculations. This means that though the relaxation in the QM part is not large the correct results is not obtained if one assumes that the QM geometry does not change at all at varying chain lengths. The effect of surface relaxation calculated explicitly at n=4 can be used to give an estimate for ΔE_{tot} at n=6 and 8. As can be seen by the position of blue squares in Fig. 5.9 ΔE scales nearly linear with the chain length in this approximation.

The comparison of the two thiolate models shows an even smaller energy separation in the short chain regime than at n=10. As for the longer chains the classical energy is identical but in the QM part the "1 chain" model is favoured by only 0.6 kcal/mol.

Even though a comparison to the low coverage regime is not perfect because of the differing chain lengths it still gives some interesting information. First of all, in the low coverage regime at n=1, adsorption in the fcc and hcp hollow sites was found to be stable in contrast to the results at full coverage (n=10). The bridge position as observed for the full coverage regime is not stable. The thiolate model in fcc configuration is separated by 11 kcal/mol from the disulfide model. This is about twice the difference in adsorption energy compared to full coverage at n=10. One reason for this large difference lies in the relaxation of the gold surface which is much stronger at low coverage (see Section 5.5.2).

Adsorption and cohesive energies

In order to get an idea about the stability of the monolayer it is instructive to calculate the strength of the headgroup-gold interaction and the packing energy of the hydrocarbon chains. Note, that the data presented here has only qualitative character since the QM/MM approach prohibits the accurate determination of adsorption and packing energies.

The standard procedure to obtain adsorption energies is to calculate the energy difference between the studied system and the original fragments of the system:

$$E_{\mathrm{ads}} = -\left[E_{\mathrm{QM}}(\mathrm{Monolayer}) - \{E(\mathrm{Au}(111)) + 8 \cdot E(\mathrm{RSSR})\}\right] . \qquad (5.11)$$

Here E_{QM}(Monolayer) is the energy of the quantum part in system, E(Au(111)) the energy of the bare surface and E(RSSR) the energy of an isolated H_3CSSCH_3 molecule. In the QM/MM approach, as presented in Section 5.4, E_{QM}(Monolayer) corresponds to 16 adsorbed SCH_3 molecules on a Au(111) surface. However, it cannot be expected that in a QM/MM calculation this procedure gives numbers of the same accuracy as in a fully QM study. The reason for this is the introduction of the artificial link atom into the system and the coupling of the classical part to the quantum part. Nevertheless it provides at least a qualitative information on the strength of the alkanethiol adsorption.

The calculation of the hydrocarbon chain packing energy is similar:

$$E_{\mathrm{coh}} = -\left[E_{\mathrm{MM}}(\mathrm{Monolayer}) - 16 \cdot E(\mathrm{S(CH_2)_{n-1}CH_3})\right] , \qquad (5.12)$$

where the alkanethiol chains are considered to be in the gas phase, isolated and fully relaxed. In the calculation of the classical energy the QM atoms are kept frozen and do not interact with each other because this part is governed by DFT in this implementation. The cohesive energy E_{coh} is mainly determined by the van-der-Waals interactions but takes also the internal structure of the chains (e.g. gauche defects) into account.

The adsorption and cohesive energies are given in Tab.5.3. At a chain length of n=10 the contribution of the chain-chain interactions is considerably higher than the adsorption energy. For the thiolates the classical cohesive energy amounts to $\sim$16 kcal/mol compared to the adsorption energy of only $\sim$4 kcal/mol. This energy difference almost disappears for shorter chain lengths (n=4). In the disulfide model the adsorption energy is negative at both chain length. It demonstrates that the expected gain in energy due to the sulfur dimerisation does not compensate the lower number of sulfur bonds to the gold surface compared to the thiolate model. In this scenario the stabilisation of the monolayer is governed completely by the chain packing.

Model	n	$E_{\mathrm{ads,QM}}$	$E_{\mathrm{coh,MM}}$	E_{tot}
Thiolate (1 chain)	10	4.3	15.9	20.2
Thiolate (4 chains)	10	3.1	15.9	19.0
Disulfide	10	-0.9	13.1	12.2
Thiolate (1 chain)	4	4.4	4.8	9.2
Thiolate (4 chains)	4	3.8	4.8	8.6
Disulfide	4	-0.4	3.9	3.5
Thiolate (fcc, low cov.)	1	19	-	19
Thiolate (hcp, low cov.)	1	16	-	16
Disulfide (low cov.)	1	8	-	8

Table 5.3: Adsorption energies $E_{\mathrm{ads,QM}}$, classical cohesive energy $E_{\mathrm{coh,MM}}$ and $E_{\mathrm{tot}} = E_{\mathrm{ads,QM}} + E_{\mathrm{coh,MM}}$. The energies are in kcal/mol. See text for more details.

The shortening of the chains to n=4 leads to slightly increased adsorption energies for thiolates and disulfides (0.1 resp 0.5 kcal/mol). This indicates that the longer the chains, the stronger the constraint is on the interface due to the chain-chain interaction. In a simplified picture one could say that the headgroup has more freedom to get into its optimum position. Thus, the headgroup formation depends in some way on the chain length. For a closer study of this effect further calculations with varying chain length would be necessary. However, these findings show that information gained from simulations of SCH_3 (n=1) are limited and can not be transferred to monolayers of longer chain length. Interestingly in the disulfide model the gain in energy is considerably higher than for the thiolate model. This might be explained by the lower symmetry of the disulfide configuration which causes a higher strain in the hydrocarbon layer which is partly resolved for the shorter chains.

In comparison to the low coverage regime the adsorption energy decreases dramatically. The binding energy of a thiolate molecule is reduced from 19 kcal/mol at low coverage to about 4 kcal/mol at high coverage. The same trend is observed for the disulfide species where the adsorption energy becomes even negative. However, as mentioned above these numbers have to be taken with caution. The adsorption at high coverage and low coverage differs considerably in terms of the preferred adsorption site, the orientation of the headgroup and the relaxation of the gold surface. This will be discussed in more detail in the next section.

The cohesive energy for the thiolate "1 chain" and "4 chain" model is $\sim$ 16 kcal/mol at the chain length n=10. This is in qualitative agreement to Mar *et al.* [115] that found a chain-chain interaction of 20 kcal/mol for the C15 system. Experiments predicted an energy contribution of 1.5 kcal/mol [134] per CH_2 group in an alkanethiol monolayer. The experimental value for the cohesive energy of a polyethylene crystal is 2.02 kcal/mol [128]. Obviously, the packing of the hydrocarbon chains on the gold surface can not be as efficient as for the hydrocarbon crystal because the adsorption underlies the periodicity of the gold surface. Hence, the lower value for the cohesive energy found here is not surprising.

Upon shortening of the chain length to n=4 the cohesive energy is reduced to 4.9 respectively 3.8 kcal/mol for thiolate and disulfide. It seems that the packing for the shorter chains, particularly in the thiolate model, is not as good as for the longer chains. Probably this is due to the restraint caused by the periodicity of the gold surface which effects all CH_2 in the shorter chains but just a fraction in the long chains.

The elucidations in this section demonstrated the importance of both interactions for the formation of SAMs:

- the headgroup-gold interaction makes the chains "stick" to the surface
- the chain-chain interactions forces the chains to assemble in an ordered formation and stabilises the monolayer

Molecular dynamics simulations where also kinetic effects are included would be extremely useful for the understanding of the formation process. However, the results presented here give strong support to the thiolate model since for the first time both forces types that control the self-assembly of the monolayer were taken into account.

5.5.2 Structure

After the discussion of the energetics that demonstrated that adsorption as thiolates is more favourable than adsorption as disulfides, this section will concentrate on the structure of organic monolayers. The structure gives valuable information on the origin of the energy differences between thiolate and disulfide model. In the following the structure of the monolayer, the headgroup-gold interface and the gold surface will be discussed.

The monolayer

It is common to describe the orientation of the ordered alkanethiol chains using three angles. The orientation of the molecules are defined by

- the molecular tilt ψ_{m} with respect to the surface normal

- the angle of precession about the surface normal χ away from the next nearest neighbour direction
- the angle of rotation (twist) of the C-C-C planes about the molecular axis Φ_t

The molecular tilt and the twist angle are sketched in Fig. 5.10(a) and the angle of precession in (b). Different experimental techniques were applied to gain information on the monolayer structure. Using grazing incidence X-ray experiments one can determine the tilt angle and the precession from the peak position in rod scan data (for more details see [94,100,135]). Infrared reflection absorption experiments spectroscopy (IRRAS) [97,136] provides information on the tilt angle and the twist angle. Alternative approaches to get access to the tilt angle are surface plasmon spectroscopy [137] or near edge x-ray absorption fine structure spectroscopy (NEXAFS) [138].

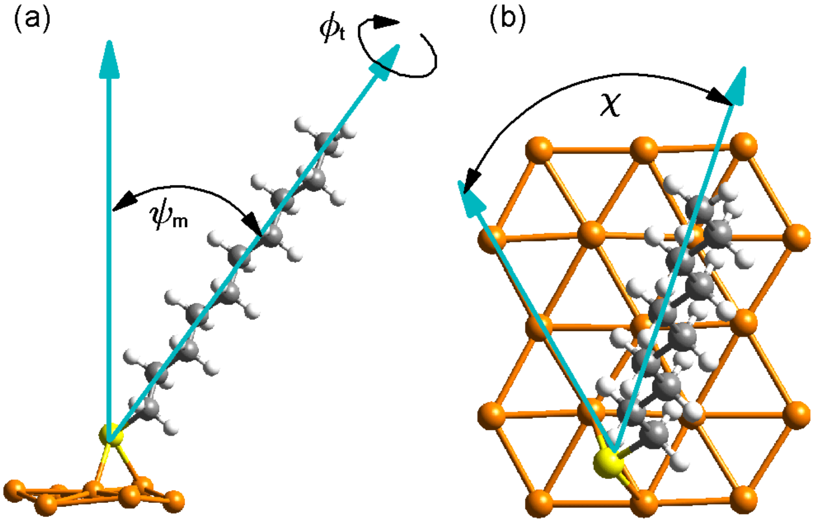

Figure 5.10: Illustration of angles used to define the chain orientation. In (a) the tilt angle ψ_m and the twist angle Φ_t are defined. The tilt angle is measured relative to the surface normal (vertical arrow). The twist angle is defined by the angle made by the chain plane and the plane perpendicular to the surface containing the chain axis. In (b) the precession χ is illustrated. It is defined as the angle between the projection of the chain backbone on the surface and the next nearest neighbour direction of the monolayer. This direction is equivalent to the nearest neighbour (NN) direction of the surface. The left arrow in (b) indicates one of the six NN directions of the Au(111) surface. In the example (Thiolate 1 chain model) the angle between the arrows is ~50° corresponding to an angle of ~10° (60°-50°) to the closest NN-direction.

Generally the problem is that the assignment of structural properties from experiment always relies on a structural model. In some cases parameters were used (e.g. in Ref. [137]) that were taken from theoretical studies of doubtable accuracy (see discussion of Ref. [117] in Section 5.3). Finally, note that experimental results on the chain structure are always averages over the whole sample.

From the theoretical side, the structural analysis of the equilibrium structures was performed on the base of a straight line connecting the last carbon atom and the carbon atom four (n=10) respectively two (n=1) CH_2 units further down in the chain. Taking this line the angles as defined above were calculated and summarised together with the experimental data in Tab. 5.4.

There is agreement in the experiments that the alkanethiol chains are tilted away from the surface normal. However, the values proposed in the literature lie in a wide range from ∼ 24°- 40°. Recently [139], it was argued that the determination of orientational parameters by means of IRRAS is more complex than the procedure applied in [136] and [97]. Therefore the values for ψ_{m}=24° and 40° from these experiments have to be taken with caution. The analysis of the tilt angle gives further support to the thiolate model. The most reliable data seems to be from X-ray diffraction and NEXAFS that suggest a tilt of ∼ 33°- 37°, which is in much better accordance with the numerical result for the thiolate model (35.6° resp. 37.0°) than for the disulfide model (28.0°).

The situation is less clear for the precession χ. Here, the experimental data varies from 14° to 22°. From the QM/MM calculations values of 10.9° ("1 chain") and 2.2° ("4 chain") were obtained for the thiolate model and 20.5° for the disulfide model. There is a slightly better agreement for the disulfide model than for the thiolate "1 chain model" whereas the data for the "4 chain model" contradicts experimental observations. Taking into account that per definition χ is limited to $0° \leq \chi < 30°$ and considering the wide spread of the experimental results (∼ 8°) experimental data appears to be quite uncontrolled. Still, these findings may speak for a coexistence of thiolates and disulfides.

For the twist angle of the chains there is only little data available [97, 136] and as mentioned above the reliability of this data is questionable. But even under the assumption that the error in Φ_{t} is large and the chain length in experiment was n=18 instead of n=10, the values still tend to speak in favour of the thiolate model. The twist observed after adsorption as thiolates ($\Phi_{\mathrm{t}} \sim$ 49°- 65°) is by far closer to experiment ($\Phi_{\mathrm{t}} \sim 50°$) than for the disulfide model ($\Phi_{\mathrm{t}} \sim 17°$).

There is some experimental information on the dependence of these angles on the chain length. In [135] there is a slight increase in the tilt angle reported going from n=10 to n=18. This is contrast to the findings from the simulations. It was found that the short chains (n=4) are more upright by ∼ 5° than the longer chains (n=10) in the thiolate model. In the disulfide model the canting of the chains was found to be constant.

The surface

As mentioned before the relaxation of the gold surface upon adsorption plays an important role in the monolayer formation. There are large differences in the degree of surface relaxation between the different coverage regimes and the different adsorption models. A good indicator for the strength of surface relaxations is the root mean square deviation (RMSD) σ of the gold surface atoms after adsorption compared to the gold

Model	n	Tilt ψ_{m}	Precession χ	Twist Φ_{t}
Thiolate (1 chain)	10	37.0	10.9	64.8
Thiolate (4 chains)	10	35.6	2.2	48.9
Disulfide	10	28.0	20.5	16.7
Thiolate (1 chain)	4	33.2	14.5	70.4
Thiolate (4 chains)	4	29.1	8.6	63.7
Disulfide	4	28.3	19.9	12.6
Experiment , Ref. [94]	10	37.0±0.5	21.8±0.6	-
Experiment , Ref. [100]	12	32.5±1	13.8±2	-
Experiment , Ref. [135]	10	32.9±1	16.4±2	-
Experiment , Ref. [136]	18	24	-	46
Experiment , Ref. [97]	16	40	-	50
Experiment , Ref. [137]	12	45±4	-	-
Experiment , Ref. [138]	12	37.5±2.5	-	-

Table 5.4: Structural analysis of monolayer. The values from simulation for the tilt angle, precession and twist angle are compared to experimental data. The methods applied are X-ray diffraction [94, 100, 135], IR absorption spectroscopy [97, 136], surface plasmon spectroscopy [137] and NEXAFS [138].

atom positions before adsorption. The RMSD of a specific layer in the gold atom is then defined as:

$$\sigma = \sqrt{\sum_{1}^{m} \frac{1}{m} |\vec{r}_{\mathrm{ads}} - \vec{r}_{\mathrm{bare}}|}\,, \tag{5.13}$$

where $|\vec{r}_{\mathrm{ads}} - \vec{r}_{\mathrm{bare}}|$ is the displacement of a gold atom after adsorption relative to its position in the bare surface and m (here m=48) is the number of atoms per layer.

In Tab. 5.5 the surface relaxations for different chain length and coverages are reported. As it would be expected the relaxations are most intense in the top layer of the surface. Going from the first to the second layer the magnitude of the relaxations is reduced by roughly 30% or more. There are only minimal changes between butanethiol and decanethiol. The relaxation in the low coverage regime appear to be in the same magnitude or even weaker. However, the number of adsorbed sulfur atoms is lower than in the high coverage regime and therefore relaxational effects are actually much stronger at low coverage. For example, the average elongation of Au-Au bonds around the adsorption sites is 18% for the thiolates at low coverage vs. 4% at high coverage. These effects are less important for disulfide adsorption where the gold bond elongation is only 6% respectively 2%. A better understanding of this phenomenon is provided by Fig. 5.11. It shows a side view of the equilibrium structure of the thiolate "4 chain" model and the disulfide model. In the former adsorption model the strongest relaxations occur in the class of the decanethiol. The gold relaxations for this system

Model	n	Layer 1	Layer 2	Layer 3
Thiolate (1 chain)	10	0.19	0.12	0.07
Thiolate (4 chains)	10	0.29	0.18	0.09
Disulfide	10	0.12	0.09	0.04
Thiolate (1 chain)	4	0.19	0.12	0.07
Disulfide	4	0.12	0.08	0.04
Thiolate (fcc, low cov.)	1	0.17	0.07	0.03
Disulfide (low cov.)	1	0.06	0.03	0.01

Table 5.5: Structural analysis of the surface. Root mean square deviations (RMSD) in Å of the gold atoms upon adsorption in comparison to the atom positions of the bare surface.

are about three times as strong as for disulfide adsorption. After formation of disulfides the gold surface still looks rather flat contrary to the thiolate adsorption in the $c(4\times2)$ phase. The different degrees of relaxation are caused by unequal adsorption sites. Obviously, adsorption in atop position as for the disulfides does not have such a large effect on the surface than adsorption in bridge position as in the case of thiolates. In the former case only a single gold atom is involved in the binding, in the latter two gold atoms are involved and their distance can change dramatically upon adsorption. The adsorption in bridge position causes a vertical lifting of the gold atoms bonded to the sulfur atom. The maximum vertical distance of two gold atoms in the first layer is $\Delta z_{\mathrm{max}} = 0.44$Å in this model. In the disulfide model this effect is much weaker with $\Delta z_{\mathrm{max}} = 0.10$Å.

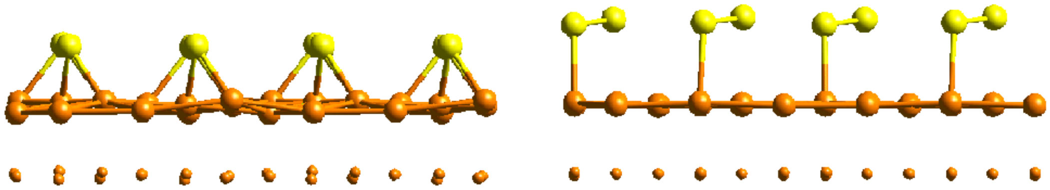

Figure 5.11: Side view of the optimised geometries of the thiolate $c(4\times2)$ model (on the left) and the disulfide model (on the right). Sulfur atoms are yellow, gold atoms of the first layer (big balls) and the second layer (small balls) are orange.

The interface

The former discussion demonstrated the differences in the surface relaxation between thiolate and disulfide adsorption. The surface relaxation is closely linked to the adsorption geometry of the sulfur headgroup. It rationalises the results of Section 5.5.1 where the headgroup-surface binding was found to be much stronger at low coverage (see also Tab. 5.3). The reason for the very strong binding at low coverage seems to be the large relaxation of the gold surface around the adsorption site. At high coverage the gold atoms cannot relax as much as in the low coverage since the number of adsorption sites is higher so that the relaxations "overlap" and cancel each other.

It should be noted again that the chain length in these two coverage regimes differs and as mentioned earlier this has an influence on the headgroup structure. However, the relaxational effects are so large that these findings are likely to be unbiased by the different chain lengths. In Tab. 5.5.2 the angle of the S-C bond with respect to the surface normal α(S-C), the bonding distances d(Au-S) and for the disulfides the length of the S-S bond are given.

Model	n	α(S-C)	d(Au-S)	d(S-S)
Thiolate (1 chain)	10	56.3	2.50	-
Thiolate (4 chains)	10	59.3	2.51	-
Disulfide	10	73.2	2.81 , 3.06	2.10
Thiolate (1 chain)	4	56.1	2.50	-
Thiolate (4 chains)	4	55.7	2.49	-
Disulfide	4	71.5	2.79 , 3.00	2.09
Thiolate (fcc, low cov.)	1	3.1	2.46	-
Disulfide (low cov.)	1	49.3	2.50 , 2.73	2.09

Table 5.6: Structural analysis of headgroup-surface interface. Given are the S-C bond angle α with respect to the surface normal, the Au-S bonding distance d and for the disulfides the length of the S-S bond. All distances are averages over the whole system and given in Å.

The adsorption as thiolates in bridge position leads to an S-C bond of $\alpha \sim 57°$ with respect to the surface normal. At n=4 the bond angle changes slightly but the nature of the bond is unchanged. Remarkable is the completely different S-C binding angle at full coverage relative to the low coverage regime. At low coverage the S-C bond is fully upright whereas at full coverage this bond is rather parallel than orthogonal to the surface. Probably this is not an effect of the chain length because in another study [123] a similar binding angle was reported at full coverage and n=1. The presence of neighbouring SCH_3 groups makes the upright configuration unfavourable and shifts the preferred adsorption site from hollow to bridge. The trend towards more upright S-C bonds is also observed for the disulfides where α is increased from 49° to 72°.

The Au-S bond for all thiolates at high coverage is constant at 2.50 Å and only slightly shorter at low coverage (2.46 Å). This bond is significantly longer than for the case of disulfide adsorption. Here, the adsorption takes place in atop position where bonds are generally longer than in bridge position. The distance from the two non-equivalent sulfur species to the next gold atom are 2.79 Å respectively 3.00 Å at full coverage and n=10. The Au-S bond length is slightly shorter for the butanethiol than for the decanethiol indicating a structural rearrangement. At low coverage the sulfur atoms are even much closer to the next gold atom (2.50 Å respectively 2.73 Å) and both species create a bond to the gold surface. This more favourable sulfur configuration (cf. adsorption energies in Tab. 5.3) is prohibited at high coverage due to steric restraints caused by the higher density of the adsorbant and the longer chains.

The length of the S-S bond is $\sim$2.10 Å, independent of chain length and coverage. The DFT result (PBE functional) for the S-S bond in the H_3CSSCH_3 molecule (gas phase) is 2.04 Å (Experiment: 2.03 Å [76]).

Comparison between thiolate and disulfide model

The preceding discussion of monolayer, interface and surface structure provides the information needed to understand why thiolate adsorption is favoured over disulfide adsorption.

The different structural models considered in this study give rise to completely different packings of the hydrocarbon chains. This can be clearly seen in Fig. 5.12 where top views of the monolayers oriented along the alkyl chains are shown. The unequal chain formation causes the energy differences in the classical part as reported in Tab. 5.2. The hydrocarbon chain packing of the two monolayers adsorbed as thiolates exhibit an entirely different symmetry but are energetically degenerate. In the thiolate "1 chain" model the angle between the carbon backbones is $\beta \sim 40°$ in opposition to the "4 chain" model with $\beta \sim 85°$ corresponding to an almost orthogonal packing. It is interesting to see that the high symmetric chain packing of the thiolate "1 chain model" is not energetically more favourable than the less symmetric thiolate "4 chain model". A closer look at the different energy contributions reveals that the energy from the valence interactions as well as the van-der-Waals energy are similar. The small difference in the tilt angle (ψ_m=37° resp. 36°) and the large energy difference found with respect to the disulfide model indicates that the adsorption as thiolates allows the hydrocarbon chains to optimise their van-der-Waals contacts.

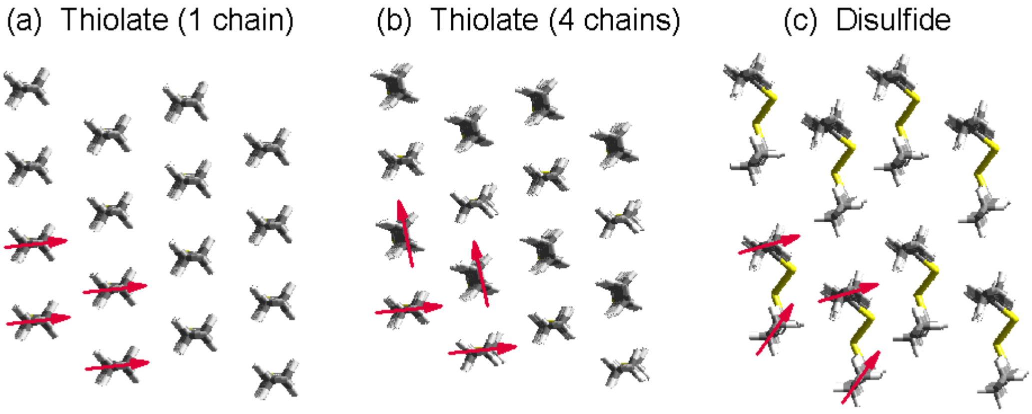

Figure 5.12: Illustration of hydrocarbon chain packing. The figure shows a top view of the monolayer oriented along the alkyl chains. The red arrows indicate the orientation of the C-C bonds at the methyl groups of the monolayer. The cohesive energy of the two thiolate models (a) and (b) is degenerate but favoured by $\sim$ 3 kcal/mol over the disulfide packing (c). The angle β between the two carbon backbone orientations is $\sim$0°(a), $\sim$85°(b) and $\sim$40°(c).

The chain tilt in the disulfide model is only ψ_m=28° which seems to be a less favourable value for the chain tilt: dimerisation at the surface leads to a chain packing that is less favourable by 2.6 kcal/mol per chain. The energy difference originates mainly from the weaker van-der-Waals interactions. The hydrocarbon packing of the thiolates is more favourable by 1.8 kcal/mol, the valence interactions by 0.8 kcal/mol. The major reason is that the constraint of the S-S bond reduces the possible configurational space of the chain formation dramatically (e.g. forcing a too low tilt angle). The orientation of the chains is much more determined by the sulfur positions as in the case of the thiolates. In addition, a close inspection of Fig. 5.12 shows that the chains in the disulfide are splayed and not parallelly aligned as in the thiolate "1 chain" model. Obviously, the parallel alignment causes a more efficient packing. Furthermore for an efficient packing in the disulfide monolayer a gauche defect must be introduced into the chains as already discussed in Section 5.2 (see also Fig. 5.2). This explains why the disulfide model is not only disfavoured in terms of the van-der-Waals interactions but also in terms of the valence interactions.

The contributions from the quantum part also speaks for the thiolate model. The pairing of the sulfur atoms is equivalent to the formation of an additional bond but at the same time the number of Au-S bonds is reduced. The adsorption energies found in the simulations demonstrate that the lower number of sulfur-surface bonds is not compensated by the sulfur dimerisation. This is in agreement with the results in the low coverage regime and n=1 [43].

X-ray diffraction data

In Section 5.5.2 a comparison between theory and experiment was drawn in terms of the chain orientation in real space. Other information to which the results from the QM/MM simulation can be compared to, is available in form of X-ray diffraction patterns. According to diffraction theory (see e.g. [140, 141]), the overall amplitude of a wave diffracted by the (hkl) plane of a crystal is given by the structure factor

$$F_{hkl} = \int_V \rho(\mathbf{r}) e^{i\mathbf{qr}} d\mathbf{r} \, . \tag{5.14}$$

Here, $\mathbf{q}$ is a reciprocal lattice vector, defined by the primitive translations of the reciprocal lattice $\mathbf{b_x}, \mathbf{b_y}, \mathbf{b_z}$

$$\mathbf{q} = (h\mathbf{b_x} + k\mathbf{b_y} + l\mathbf{b_z}) \, . \tag{5.15}$$

The integral in equation (5.14) is over the volume of the unit cell V. The intensity of the (hkl)-reflection is proportional to the square of the structure factor:

$$I \propto |F_{hkl}|^2 \, . \tag{5.16}$$

Thus, in order to obtain the diffraction pattern of the structures from the QM/MM simulations, the electron density of the system has to be calculated. Since no electron density is available for the classical part of the system a way had to be found to access ρ in another way. A relatively easy approach to obtain the electron density of the valence electrons ρ_{val} is provided by semi-empirical methods. The semi-empirical methods are based on the Hartree-Fock approach. The difference to the Hartree-Fock

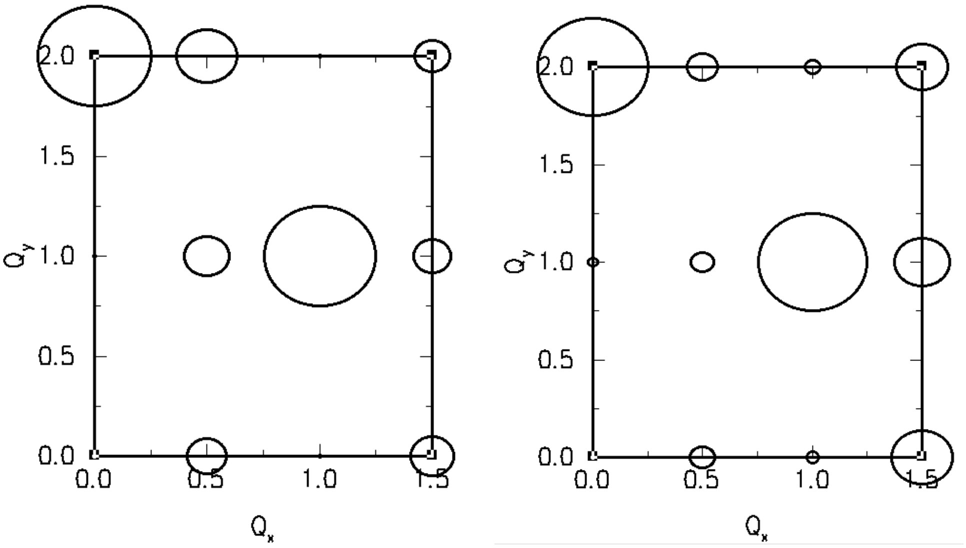

(a) Experiment **(b)** Thiolate “4 chain”

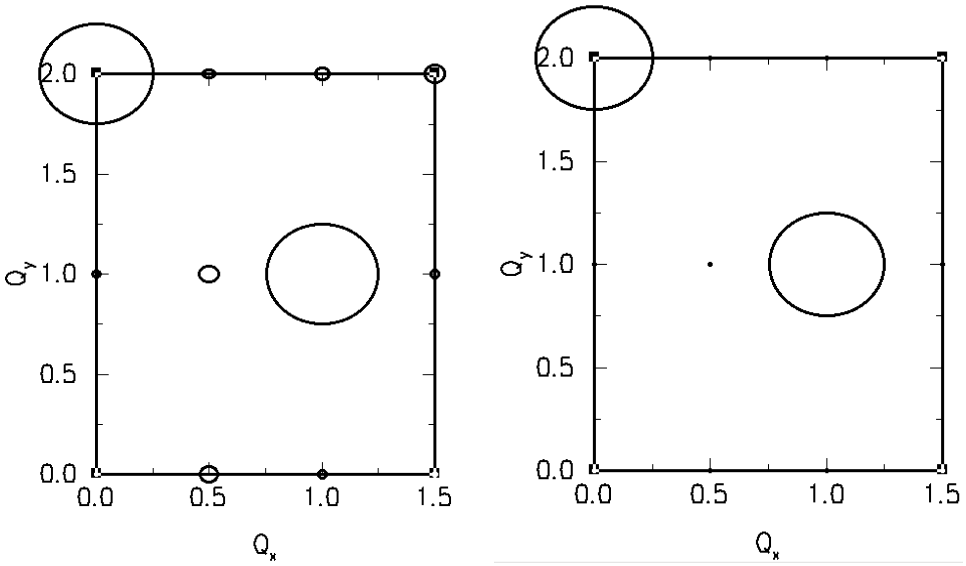

(c) Disulfide **(d)** Thiolate “1 chain”

Figure 5.13:
Comparison of the X-ray data from experiment (a) to the calculated diffraction patterns of the different models using the procedure explained in the text. All intensities were scaled such that the intensity of the hexagonal peaks (1,0) and (0,2) is the same in all graphs.

method is that some of the integrals are assumed to be zero or are replaced by empirical parameters, which are derived from experiment. For this reason these approximate quantum mechanical methods require significantly less computational resources. The level of description is by far not as high as for *ab initio* methods but in quite a short time the electron density is available for different atomic configurations in an accuracy that is sufficient for the calculation of a diffraction pattern. Different levels of approximation exist whereby the AM1 method [142] is one of the most popular methods. This method is incorporated in the MOPAC [143] program and was used in this form to calculate ρ_{val} based on the coordinates from the QM/MM simulation.

To account for the core density ρ_{core} Slater orbitals were placed at the atomic positions of the chain atoms. The unnormalised radial term for a "Slater-type orbital" (STO) [144] (see also [145]) is

$$R(n, Z, s) = r^{(n-1)} \exp[-(Z - s)r/n] \tag{5.17}$$

where Z is the nuclear charge in atomic units, n is the principal quantum number, and s is a "screening constant" which has the function of reducing the nuclear charge Z seen by an electron. The screening constants s according to the Slater rules [144] are 5.7 for the carbon 1s level, 15.7 for the sulfur 1s level and 5.925 for the sulfur 2s and 2p levels. Finally, the Fourier transformation (equation (5.14)) of the total electron density

$$\rho_{\text{tot}} = \rho_{\text{val}} + \rho_{\text{core}} \, , \tag{5.18}$$

which was calculated on a grid with a point spacing of 0.1 Å, yields the diffraction pattern of the crystalline structure. Note, that diffraction from the gold surface atoms was neglected. SAMs on gold form three different kind of domains at full coverage according to the symmetry of the Au(111) surface. To account for this symmetry the structure obtained from the simulations were rotated by 120° and 240° and the diffraction intensity from the resulting structures was added to the one of the original geometry.

The experimental reference regarding diffraction data is the study by Fenter and co-workers [94]. They performed grazing incidence X-ray diffraction experiments ($q_z \sim 0.1\text{Å}^{-1}$) of a decanethiol monolayer on gold. Based on their diffraction data they suggested self-assembly as disulfides ("disulfide model", see Section 5.2). For a direct comparison to this experiment q_z was set to 0.1Å^{-1} in equation (5.14) and in addition the intensity of the hexagonal diffraction peaks (1,1) and (2,0) was divided by three as done in Ref. [94] to receive the diffraction pattern of a single domain. Furthermore the data is displayed in terms of $Q_x = q_x/b_x$ and $Q_y = q_y/b_y$ (Q_z is constant) and the x- and y-axis are exchanged. In Fig. 5.13 the calculated diffraction patterns for the thiolate "1 chain" and "4 chain" and the disulfide model are compared to the experimental data.

The most dominant features are the hexagonal peaks which arise from the hexagonal structure of the monolayer. As expected these are the only peaks in the thiolate fcc model and refer to the $\sqrt{3} \times \sqrt{3}R30°$ unit cell (corresponding to one chain per unit cell). The appearance of additional peaks (e.g. (0.5,0), (0.5,1) and (1.5,0)) are not compatible with the $\sqrt{3} \times \sqrt{3}R30°$ unit cell. Those peaks indicate a lower symmetry of the monolayer. They correspond to the $c(4 \times 2)$ superstructure of the $\sqrt{3} \times \sqrt{3}R30°$ unit cell as already discussed in Section 5.2. The diffraction pattern in Fig. 5.13(d) reveals even more information on the monolayer structure. The non-existence of some of the $c(4 \times 2)$ related peaks [(1,0),(0,1),(1,2) and (0,3)] could only be explained under the assumption that there are two distinct types of chains in the system differing in the adsorption site of the sulfur or in the orientation of the hydrocarbon chains. Two of the atomic configurations considered in this study are compatible with this observation: the thiolate "4 chain" model and the "disulfide" model.

The calculated diffraction pattern of the $c(4 \times 2)$ model is in very good agreement to experiment. The non-existent peaks in experiment have the lowest intensity even though they are not equal to zero. The intensity of the other '$c(4 \times 2)$-peaks' relative to hexagonal peaks is close to the experimental results. The diffraction pattern obtained on the basis of the disulfide model has similar features but the relative peak intensities are much better reproduced in the $c(4 \times 2)$ model. For example in experiment there was quite a strong intensity observed at (1.5,0) but almost no intensity is predicted at this wavevector in the disulfide model.

These findings give an additional support to the binding of alkanethiol to the gold surface in form of thiolates and not as disulfides. However, it is possible that the thiolate "4 chain" model masks the thiolate "1 chain" model and the "disulfide" model. For this reason the coexistence of different configurations cannot be excluded.

Scanning Tunneling Microscopy data

Scanning Tunneling Microscopy (STM) are an extremely useful tool to gain insight into the structure of self-assembled monolayers. Indeed the $c(4 \times 2)$ superstructure suggested from helium diffraction data was confirmed in STM measurements [101]. Additionally, it was possible via STM to study the different phases in the growth process of SAMs [93]. The high-resolution STM images obtained by Poirier *et al.* [101] for the C8/Au(111) monolayer allow a qualitative comparison to the structures calculated in the QM/MM simulations.

In order to compare the optimised geometries to STM measurements height profiles of the different configurations were calculated in a simple model [116]. In this model using an imaginary tip the surface was scanned whereby the height of the monolayer at a (x,y)-position was determined by assuming the dimension of an atom to be roughly like its van-der-Waals radius. The van-der-Waals radii used are 1.7 Å for carbon and 1.2 Å for hydrogen. This model can not account for the complex physics behind STM pictures but at least it gives an impression how likely the different models coincide with the system in the experiment.

The results of this procedure are given in Fig. 5.14. One can see that the monolayers in the $c(4 \times 2)$ superlattice, the thiolate "4 chain" model and the "disulfide" model, both exhibit a height profile that is compatible with experimental results. In contrast, the chains in the thiolate "1 chain" model do all have the same height relative to the surface what is not surprising since that model corresponds to equivalent hydrocarbon chains.

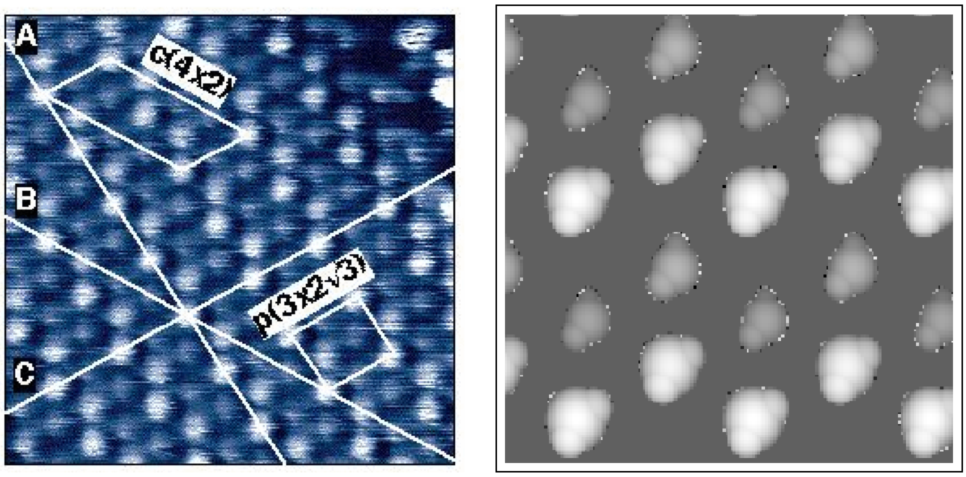

(a) Experiment **(b)** Thiolate “4 chain”

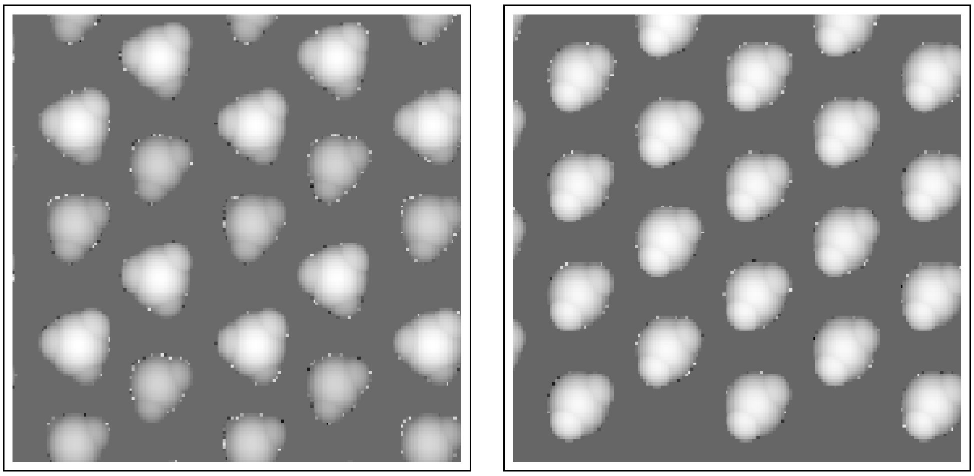

(c) Disulfide **(d)** Thiolate “1 chain”

Figure 5.14:
STM image [101] from a C8/Au(111) monolayer and calculated topological maps of the different models (n=10) using the procedure explained in the text.

5.5.3 Electronic properties

Quantum mechanical simulations have the great advantage that electronic properties are accessible. In this section electronic properties of the C10/Au(111) system will be discussed in terms of the electronic density of states (EDOS). The one-particle Kohn-Sham eigenvalues provide a reasonable approximation to the EDOS though they are not deduced from a many-particle wavefunction. The EDOS for the thiolate “1 chain” and “4 chain” models, the “disulfide” model and the bare Au(111) surface are shown in Fig. 5.15. Additionally the contribution of the sulfur atoms to the EDOS is indicated separately by the red shaded region. The contribution of specific atoms can be calculated by projecting the total wavefunction on the pseudo atomic orbitals. All eigenstates are broadened with an 0.1 eV Gaussian. The EDOS was shifted such that the highest occupied state is located at 0 eV.

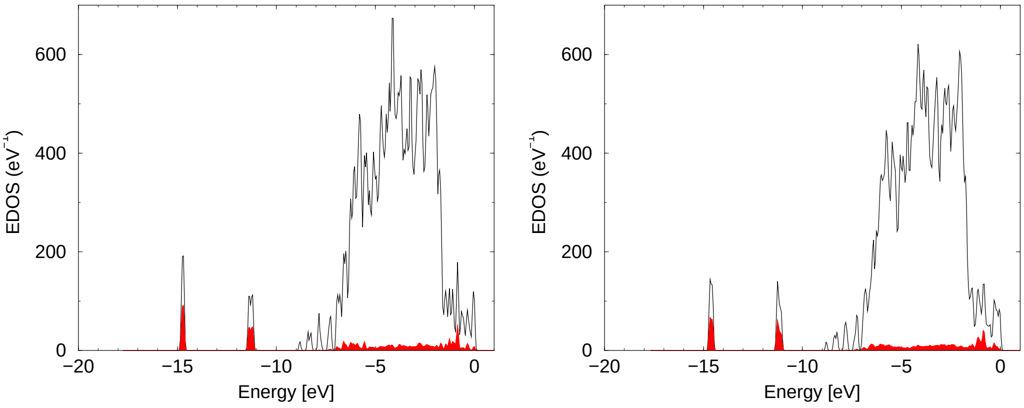

(a) Thiolate “1 chain” **(b)** Thiolate “4 chain”

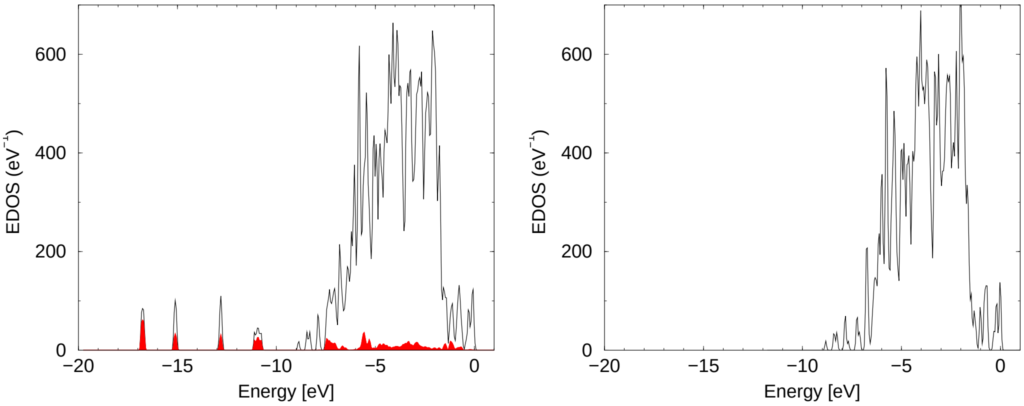

(c) Disulfide **(d)** Bare Au(111) surface

Figure 5.15:
Electronic density of states for different models of C10/Au(111) in (a-c) and the bare Au(111) surface in (d). The eigenstates are broadened with an 0.1 eV Gaussian. The red shaded part is the projection on the sulfur atoms. The EDOS was shifted in such a way that highest occupied state is located at 0 eV.

The EDOS of the bare gold surface is dominated by the manifold of d-states between 2 eV and 7 eV. The states around 0 eV and 8 eV correspond to the intrinsic surface states of the Au(111) surface as observed in photoemission experiment [146]. Upon adsorption the range of eigenstates is extended noticeably. Adsorption as thiolates leads to new states at ∼ 11 eV and ∼ 15 eV. These states which differ only slightly between the thiolate models have a strong contribution of the sulfur atoms. In the disulfide model an additional splitting of the sulfur dominated states occurs. Due to the different nature of the sulfur species, different headgroup-metal interactions take place that cause the splitting in the states. Besides the low-lying states there is some small sulfur contribution over the energy range with the exception of the region between 7 eV and 9 eV. The EDOS of the two thiolate models are very similar. Only the states close to the Fermi energy have different shapes. Interestingly, those states are almost unchanged upon disulfide adsorption compared to the bare surface.

5.6 Summary

In this chapter self-assembled monolayers formed by alkanethiols on the Au(111) surface were studied by means of a combined QM/MM approach. The results of the computer simulations revealed that adsorption as thiolates in the bridge position is energetically most favourable at the chain length n=10. The potential energy of this configuration is ~ 8 kcal/mol lower per chain than the monolayer based on disulfide adsorption. For the thiolates the binding to the surface is stronger (~ 5 kcal/mol) but it is also favoured in terms of the packing of the hydrocarbon chains (~ 3 kcal/mol). The two investigated thiolate configurations corresponding to the $\sqrt{3} \times \sqrt{3}R30°$ and $c(4 \times 2)$ unit mesh are energetically nearly degenerate. This strongly suggests the possibility that these two phases may coexist on the surface as indeed observed in an STM study [108].

The structural analysis of the monolayer further supported the thiolate model. The molecular tilt of the chains observed in experiment (32°- 37°) is much closer to the value found for the thiolate models (36° resp. 37°) than for the disulfide model (28°). The information provided by the precession of the chains is in slightly better agreement with the disulfide model whereas the twist angles determined in experiment tends to speak for thiolate adsorption. The comparison of experimental X-ray diffraction data to calculated diffraction pattern shows an excellent agreement between experiment and the $c(4\times 2)$ structure in contrast to the disulfide structure. Assuming that the $c(4\times 2)$ structure masks the thiolate "1 chain" and the disulfide structure and considering the data for the precession angle, coexistence of thiolates and disulfides cannot be excluded.

The chain length and coverage of the monolayer has an impact on the relative stability of the different models and the chain orientation. At shorter chain length (n=4) the energetical ordering of the chains is unchanged. The two thiolate models are still energetically degenerate but the energy difference to the disulfide model is reduced to 6 kcal/mol. Almost no changes occurred in the interface structure whereas the orientation of the chain is changed by some degrees. The comparison of the full coverage regime at long chain length to the low coverage regime at short chain length revealed the following: the adsorption to the surface is much weaker in the former case but on the other hand the monolayer is stabilised by ~ 1.5 kcal/mol per CH_2 unit due to the chain-chain interactions. In addition the simulations demonstrated a different site preference in the two regimes: adsorption in the bridge site at full coverage (n=10) in contrast to adsorption in the fcc hollow site at low coverage (n=1).

Chapter 6

Summary

In this thesis density functional theory was applied to various systems taken from the field of nanostructures on surfaces and clusters. The overall goal of the work was to answer open questions emerging from experimental data and provide information for a better understanding of the selected systems.

The study of hydrogenated gold clusters was motivated by the experimental results of a photodetachment study of small Au_nH^- clusters which called for a deeper analysis by means of *ab initio* calculations. The first task was to identify the cluster isomers which were actually detected in experiment. By comparing calculated and measured vertical detachment energies for a large number of isomers, it was possible to determine the cluster geometry for each cluster size. It arose from the discussion that the interpretation that is usually applied fails for this particular system. Instead, a new interpretation was introduced that gives excellent agreement with experiment. Subsequently, the surprising experimental finding that the vertical detachment energies of $Au_{n-1}H^-$ and Au_n^- exhibit a striking similarity was investigated. As a first result it was concluded that this effect can only be expected when geometries of bare and hydrogenated clusters with the same number of atoms are similar. To illuminate the phenomenon from the electronic point of view, the wavefunction of the detached electron was considered. The analysis revealed that the detached electron is to a large extent localised in the same regions of the bare and hydrogenated cluster. For this reason the replacement of a gold atom by a hydrogen does not alter the vertical detachment energy significantly.

The study of deposited Si_4 clusters in the second part of the thesis links the fields of surface and cluster physics. The purpose of this investigation was to examine if the "magic" silicon tetramer is a suitable candidate for the formation of a new cluster material. A major requirement is that a barrier exists between cluster species which prevents the merging of clusters into amorphous bulk material. The DFT calculations that were performed showed that a repulsive barrier along certain paths exists when two Si_4 clusters are approached. This result, which proposes the existence of separated Si_4 cluster species on a surface is in agreement with XPS measurements indicating the same findings. The combination of the theoretical and experimental results suggests that the silicon tetramer may serve as a building block in new materials.

In the last part of the thesis the focus was on self-assembled monolayers formed by alkanethiols on a gold surface. These monolayers have been identified as playing a key role in today's nanotechnology but nonetheless the detailed structure of the monolayers have still not been established. The theoretically challenging requirement of describing both the chain-chain and substrate-chain interactions accurately made it necessary to apply an approach that is not solely based on DFT. Due to the known deficiencies of DFT in describing dispersive interactions - as they occur between hydrocarbon chains - classical methods had to be introduced into the model. Using this hybrid approach, the long-standing question, of whether adsorption takes place as thiolates or disulfides was investigated at different chain lengths. The calculations revealed that thiolate adsorption is favoured energetically for both short (butanethiol) and long (decanethiol) chains. The energy difference between the two models is 8 kcal/mol per chain for the longer and 5 kcal/mol for the shorter chains and decreases linearly with chain length. In the thiolate model the position of the adsorbed sulfur atom at the head of the chain is the bridge site slightly off-centred towards the hollow site. A comparison to different sets of experimental data, ranging from X-ray diffraction to STM to IR absorption, supports the thiolate model however it is possible that disulfide may coexist.

The results in all three parts of this work demonstrate that the understanding of physical systems can be improved significantly when information from theory and experiment are put into context. In some cases, as shown here for the self-assembled monolayers, the development of new methods is necessary to provide the needed accuracy. Although a lot has been learned about the structure of self-assembled monolayers, there is still much to explore in terms of understanding the formation process and efficient tailoring of the monolayer, in order to control specific properties for the use in technical applications. In the experiments on hydrogenated gold clusters the adsorption of more than one hydrogen atom onto a gold cluster was observed very rarely. Can we understand this behaviour quantitatively with numerical simulations and does it change at larger cluster sizes? Finally, the encouraging results found in the study of Si_4 clusters stimulate similar investigations of other "magic" clusters. These investigations may start with a screening of candidates using computer simulations before clusters are actually deposited in the laboratory.

Chapter 7

Zusammenfassung

In dieser Doktorarbeit wurden drei Systeme aus der Oberflächen- und Clusterphysik behandelt, die alle im Zusammenhang zur Nanophysik stehen. Zu den wesentlichen Problemstellungen in der Nanophysik heutzutage gehört die Bestimmung von möglichen Bausteinen, die zur Strukturierung von Oberflächen verwendet werden können. Eine andere Aufgabe ist die Entwicklung von Methoden diese Bausteine in einer technologisch sinnvollen Weise anzuordnen. Desweiteren von Interesse ist ein grundlegendes Verständnis von Adsorptionsvorgängen an kleinen Teilchen. Insbesondere Nanoteilchen aus Gold besitzen vielversprechende Eigenschaften, welche z.B. in der Katalyse ausgenutzt werden können. Die untersuchten Systeme in dieser Arbeit, hydrogenierte Goldcluster Au_nH, auf einer Oberfläche deponierte Si_4 Cluster und selbst-aggregierte Monolagen aus Alkanthiolketten auf einer Goldoberfläche, stehen im direkten Bezug zu diesen Problemstellungen.

Die Methode, die zum Studium dieser Systeme angewandt wurde, ist die Dichtefunktionaltheorie (DFT). Diese Theorie erlaubt die quantenmechanische Untersuchung von atomaren Systemen anhand von Computersimulationen. Der besondere Vorteil dieser Methode ist, daß keinerlei empirische Parameter in die Theorie eingehen, welche die Ergebnisse verfälschen könnten. Darüberhinaus sind mit der Dichtefunktionaltheorie Systeme einer Größenordnung zugänglich (~ 1000 Atome), die bei Verwendung von anderen Methoden nicht erreichbar sind. Zur Bearbeitung der ersten beiden Themen, Au_nH Cluster und deponierte Si_4 Cluster, wurde die Standardimplementation der Dichtefunktionaltheorie verwendet. In der Studie der selbst-aggregierten Monolagen war es aufgrund der vorherrschenden Kräfte in diesem System nötig, zusätzliche, klassische Wechselwirkungen zu berücksichtigen. Es wurde ein sogenannter "QM/MM"-Zugang entwickelt, in dem ein Teil des Systems mit quantenmechanischen (QM), und der andere Teil mit klassischen (MM) Wechselwirkungen beschrieben wird.

Die Motivation zur Untersuchung von hydrogenierten Goldclustern Au_nH ($n \leq 6$), beruhte auf einer Photoelektronenspektroskopie-Studie, die in der Arbeitsgruppe von G. Ganteför durchgeführt wurde. Hierbei zeigte sich, daß die vertikale Detachmentenergie (VDE) eine verblüffende Ähnlichkeit zwischen Au_n^- und $Au_{n-1}H^-$ Clustern aufweist, was darauf hindeutet, daß sich das Wasserstoffatom in dieser speziellen chemischen Umgebung wie ein Goldatom verhält. Zum weiteren Verständnis war es zuerst nötig, die Geometrie der Cluster zu bestimmen, welche im Experiment beobachtet wurden. Dazu wurde für eine Vielzahl von Clustergeometrien, die potentielle Energie und die VDE anhand von Computersimulationen bestimmt. Der Vergleich der theoretischen und experimentellen Ergebnisse zeigte, daß die übliche Standardinterpretation, welche das Isomer mit der niedrigsten Energie als das im Experiment beobachtete vorschlägt, in diesem Falle nicht gültig ist. Stattdessen wurde eine Interpretation vorgeschlagen, welche annimmt, das die Au_nH^- Teilchen in der Clusterquelle durch Adsorption eines anionischen Wasserstoffs H^- an einem neutralen Goldcluster erzeugt werden. Dies bedeutet, daß die Geometrien der Au_nH^- Cluster mit denen der neutralen Goldcluster eng verwandt sind. Wenn man die VDE dieser Isomere mit den experimentellen Daten vergleicht, zeigt sich eine hervorragende Übereinstimmung. Nachdem die im Experiment vorkommenden Cluster bestimmt wurden, war es nun möglich die elektronische Struktur der Au_n^- und $Au_{n-1}H^-$ Cluster miteinander zu vergleichen. Die Analyse ergab, daß für bestimmte Clustergrößen, die Wellenfunktion des vom Anion entfernten Elektrons in beiden Fällen in den gleichen Bereichen des Clusters lokalisiert ist. Diese chemische Ähnlichkeit erklärt, wieso die VDE von reinen und hydrogenierten Goldclustern mit der gleichen Atomanzahl fast identisch sind.

Im zweiten Teil der Arbeit wurde untersucht, ob Si_4 möglicherweise als Baustein in neuen Materialien verwendet werden könnte. Der Si_4 Cluster gehört zu den sogenannten “magischen” Clustern, die sich durch besonders hohe Stabilität auszeichnen. Zuerst wurde das Verhalten eines Si_4 Clusters auf einer Goldoberfläche simuliert. Die Ergebnisse der Simulation ließen allerdings darauf schließen, daß die Goldoberfläche kein geeignetes Substrat darstellt. Die starken Wechselwirkungen zwischen Cluster und Oberfläche führten zu starken strukturellen Relaxationen im Cluster. Erwünschenswert wäre dagegen eine relativ schwache Cluster-Substrat Wechselwirkung, die den Cluster in seiner ursprünglichen Geometrie erhält und die Diffusion der Cluster auf der Oberfläche erlaubt. Dieser Fall ist gegeben für eine Graphitoberfläche, die als inert bekannt ist. Um die Eignung von Si_4 Cluster als ein Baustein zu überprüfen, muß untersucht werden ob eine Barriere existiert, die das Verschmelzen der Cluster zu amorphem Silizium verhindert. Aufgrund der schwachen Wechselwirkung mit dem Substrat und der Tatsache, daß Graphit in DFT nur ungenau beschrieben werden kann, wurde diese Fragestellung anhand zweier Si_4 Cluster in der Gasphase untersucht. In der Folge wurde die Potentialkurve für die Annäherung zweier Cluster bezüglich verschiedener Richtungen aufgenommen. Für alle untersuchten Richtungen existierte entweder eine Potentialbarriere oder es bildete sich gar keine Bindung zwischen den Clustern aus. Diese Ergebnisse deuten an, daß Si_4 in der Tat die erforderten Eigenschaften als mikroskopischer Baustein erfüllt. Diese theoretischen Erkenntnisse sind in Einklang mit experimentellen Ergebnissen, welche die selben Schlußfolgerungen nahe legen.

Eine vielversprechende Methode zur Erzeugung von Nanostrukturen ist die Selbst-Organisation. Ein Beispiel dafür sind selbst-aggregierte Monolagen aus organischen Molekülen auf einer Au(111) Oberfläche. Vor etwa 20 Jahren wurde entdeckt, daß Alkanthiolketten ($HS(CH_2)_{n-1}CH_3$) die einer Goldoberfläche ausgesetzt sind, sich selbständig in einer hochgeordneten Struktur organisieren. Der Grund für dieses erstaunliche Phänomen liegt in der Balance der Wechselwirkungen zwischen den Kettenmolekülen auf der einen Seite, und der Wechselwirkung zwischen Substrat und

Kettenmolekülen auf der anderen Seite. Die Wechselwirkung zwischen den Alkanthiolketten wird von van-der-Waals Kräften bestimmt, die in DFT nur unzureichend beschrieben werden können. Aus diesem Grund wurde ein klassisches Kraftfeld in das Modell eingeführt, welches eine akkurate Beschreibung dieser Kräfte garantiert. Trotz hohem experimentellem Aufwand ist bislang ungeklärt, welcher Art die Bindung der Alkanthiolketten an die Oberfläche ist. Auf der Grundlage von experimentellen Daten sind in der Literatur zwei Modelle vorherrschend, welche Adsorption als Thiolate oder als Disulfide vorschlagen. Um Licht in diese Debatte zu werfen, wurde die Struktur und Energie der beiden Modelle mit Hilfe von QM/MM Simulationen untersucht. Es zeigte sich, daß die Adsorption in Form von Thiolaten sowohl energetisch günstiger ist, als auch die bessere Übereinstimmung mit den experimentellen Ergebnissen bezüglich der Struktur aufweist. Weitere Unterstützung für das Thiolatmodell lieferte der Vergleich von berechneten mit experimentell bestimmten Beugungsbildern der Monolage, der eine deutlich bessere Übereinstimmung im Falle des Thiolatmodells zeigte. Abschließend wurden Simulationen von Ketten verschiedener Länge durchgeführt, um Einblick in den Einfluß der Kettenlänge auf die Monolagenstruktur zu erhalten.

Appendix A

Conversion of Units

- 1 Hartree = 1 a.u. $\hat{=}$ 27.21140 eV
- 1 Rydberg $\hat{=}$ 13.6057 eV
- 1 kcal/mol $\hat{=}$ 0.0433641 eV
- 1 cm^{-1} $\hat{=}$ $1.23985 \cdot 10^{-4}$ eV
- 1 Bohr $\hat{=}$ 0.529177 Å

Appendix B

Computational Details

B.1 Software

The software used for the simulations in this thesis is the CPMD (Car-Parrinello Molecular dynamics) program [21]. For the calculation in Chapter 3 and 4 the program in the version 3.0 and 3.4 was used. The code used in Chapter 5 is based on version 3.3b. For the implementation of the QM/MM approach several subroutines were written in FORTRAN 77 and added to the main program.

B.2 Computational Requirements

To give an idea about the computational requirements of the different simulations, the time needed to perform one wavefunction step is given in the following table:

	IBM RS/6000 (200 MHz)		IBM RS/6000 (375 MHz)	
	# Proc.	Time [s]	# Proc.	Time [s]
Au_5H cluster	1	180	15	17
2 Si_4 cluster	-	-	8	8
Si_4/Au(111)	-	-	18	100
SAM	64	350	52	200

Table B.1: Computational requirements of simulations in this thesis. In the table the time needed for one wavefunction step is given in seconds. It depends on the size of the studied system, the type of computer and the number of processors used.

For one geometry step it takes about 5-15 iterations of the wavefunction. The number of geometry steps needed to find a minimum on the potential energy depends strongly on the initial configuration, the degrees of freedom in the system, the convergence criterium and the optimisation technique used (see Section 2.8). In the Au_nH system it takes about 10-30 geometry steps to find a local minimum.

B.3 Input File

A typical input file for a geometry optimisation of a hydrogenated gold cluster looks like this:

```
 &CPMD
    OPTIMIZE GEOMETRY
    CONVERGENCE ORBITALS
      0.00001
    CONVERGENCE GEOMETRY
      0.0005
    EMASS
     500
    LSD
&END

&BASIS
PSEUDO AO 3
0 1 2
PSEUDO AO 1
0
&END

&SYSTEM
   SYMMETRY
    0
   CELL
    25.   1.0000  1.   1.   .0000   .0000
   CUTOFF
    50.
&END

&DFT
SLATER
0.6666666666666667
LDA CORRELATION PZ
OLDCODE
GRADIENT CORRECTIONS PBEX PBEC
GC-CUTOFF
.10000E-05
&END

&ATOMS
Gold
*AU_MT_PBE   KLEINMANN-BYLANDER    RAGGIO=1.2
 2    0     9
 4
    13.5887 14.9821  8.9760
    11.6247 12.7983 13.1172
```

```
     9.1233 11.3458 16.9562
    15.6657 10.8486 10.9727
Hydrogen
*H_GIA_PBE     KLEINMANN-BYLANDER    RAGGIO=1.0
 0    0     9
 1
      12.0285 17.4268  8.1814
&END
```

Acknowledgment

Finally I would like to thank the following people who have helped to make this thesis possible:

- ....in Rüschlikon
  - Wanda Andreoni for advising my thesis, for teaching me a lot about DFT and chemistry, for the exciting topic and for giving me the opportunity to present my work at international workshops
  - Alessandro Curioni for all his support, in particular in terms of computers, physics and chemistry and for many clever ideas on how to solve problems
  - the whole group in Rüschlikon for the nice atmosphere and entertaining z'Nünis and Schoggi-Gipfelis
  - the IBM Research Laboratory in Rüschlikon for the kind hospitality
  - Lindsey, Salomon and Nikolaj for proof-reading my thesis
- ....in Konstanz
  - Peter Nielaba for advising my thesis, for many helpful conversations about physics and other things, for the continuous support and encouragement during the thesis (especially in the final stages) and for the trips to various workshops
  - Gerd Ganteför for initiating my interest for cluster physics and for many interesting discussions during our collaboration
  - Yolanda Fischer for always organising a hotel room for me even when I called last minute
  - the whole group in Konstanz for an entertaining time when I was in Konstanz, especially for providing the coffee and the cookies
- ....at home
  - my family for advise, encouragement, support, delicious food when I was at home and much more

Bibliography

[1] R. Feynman, "There's Plenty of Room at the Bottom" in Engineering and Science, California Institute of Technology, 1960.

[2] G. Binnig and H. Rohrer, Helv. Phys. Acta **55**, 726 (1982).

[3] D. M. Eigler and E. Schweizer, Nature **344**, 524 (1990).

[4] H.-G. Boyen, G. Kästle, F. Weigl, B. Koslowski, C. Dietrich, P. Ziemann, J. P. Spatz, S. Riethmüller, C. Hartmann, M. Möller, G. Schmid, M. G. Garnier, and P. Oelhafen, Science **297**, 1533 (2002).

[5] R. G. Nuzzo and D. L. Allara, J. Am. Chem. Soc. **105**, 4481 (1983).

[6] H. F. Schaefer, *The Electronic Structure of Atoms and Molecules: A Survey of Rigorous Quantum-Mechanical Results* (Addison-Wesley, Reading, Massachusetts, 1972).

[7] B. L. Hammond, W. A. Lester, and P. J. Reynolds, *Monte Carlo Methods in Ab Initio Quantum Chemistry* (World Scientific, Singapore, 1994).

[8] G. Galli and A. Pasquarello, in *Computer Simulation in Chemical Physics*, edited by M. P. Allen and D. J. Tildesley (Kluwer Academic Publishers, Netherlands, 1993), Chap. First-Principles Molecular Dynamics.

[9] M. Payne, M. P. Teter, D. C. Allan, T. A. Arias, and J. D. Joannopoulos, Rev. Mod. Phys. **64**, 1045 (1992).

[10] D. Marx and J. Hutter, in *Modern Methods and Algorithms of Quantum Chemistry*, edited by J. Grotendorst (John von Neumann Institute for Computing, Jülich, 2000), Chap. Ab initio molecular dynamics: Theory and Implementation.

[11] A. R. Leach, *Molecular Modelling* (Pearson Education Limited, Edinburgh, 2001).

[12] "Random Walk through CPMD", J. Hutter (1995), revised by A. Curioni (1998).

[13] R. G. Parr and W. Yang, *Density-Functional Theory of Atoms and Molecules* (Oxford University Press, Oxford, 1989).

[14] P. Hohenberg and W. Kohn, Phys. Rev. **136**, B864 (1964).

[15] W. Kohn and L. J. Sham, Phys. Rev. **140**, A1133 (1965).

[16] J. P. Perdew and A. Zunger, Phys. Rev. B **23**, 5048 (1981).

[17] D. M. Ceperley and B. I. Alder, Phys. Rev. Lett. **45**, 466 (1980).

[18] J. P. Perdew, K. Burke, and M. Ernzerhof, Phys. Rev. Lett. **77**, 3865 (1996).

[19] A. D. Becke, Phys. Rev. A **38**, 3098 (1988).

[20] C. Lee, W. Yang, and R. G. Parr, Phys. Rev. B **37**, 785 (1988).

[21] CPMD code by J.Hutter: Copyright IBM Corporation (1990,1997,2001) and MPI für Festkörperforschung Stuttgart (1997), see www.cpmd.org.

[22] R. Feynman, Phys. Rev. **56**, 340 (1939).

[23] P. Pulay, Molec. Phys. **17**, 197 (1969).

[24] P. Pulay, Adv. Chem. Phys. **69**, 241 (1987).

[25] D. R. Hamann, M. Schlüter, and C. Chiang, Phys. Rev. Lett. **43**, 1494 (1979).

[26] N. Troullier and J. L. Martins, Phys. Rev. B **43**, 1993 (1991).

[27] G. B. Bachelet, D. R. Hamann, and M. Schlüter, Phys. Rev. B **26**, 4199 (1982).

[28] C. G. Broyden, J. Inst. Math. Appl. **6**, 222 (1970).

[29] R. Fletcher, Comp. J. **13**, 317 (1970).

[30] D. Goldfarb, Math. Comp. **24**, 23 (1970).

[31] D. F. Shanno, Math. Comp. **24**, 647 (1970).

[32] R. Car and M. Parrinello, Phys. Rev. Lett. **55**, 2471 (1985).

[33] G. Pastore, E. Smargiassi, and F. Buda, Phys. Rev. A **44**, 6334 (1991).

[34] W. A. de Heer, Rev. Mod. Phys. **65**, 611 (1993).

[35] H.-G. Boyen, T. Herzog, G. Kästle, F. Weigl, P. Ziemann, J. P. Spatz, M. Möller, R. Wahrenberg, M. G. Garnier, and P. Oelhafen, Phys. Rev. B **65**, 075412 (2002).

[36] K.-M. Ho, A. A. Shvartsburg, B. Pan, Z.-Y. Lun, C.-Z. Wang, J. G. Wacher, J. L. Fye, and M. F. Jarrold, Nature **392**, 582 (1998).

[37] G. von Helden, M. T. Hsu, N. G. Gotts, and M. T. Bowers, J. Phys. C: Solid State Phys. **97**, 8182 (1993).

[38] A. Sanchez, S. Abbet, U. Heiz, W.-D. Schneider, H. Häkkinen, R. N. Barnett, and U. Landman, J. Phys. Chem. A **103**, 9573 (1999).

[39] G. Rubio-Bollinger, S. R. Bahn, N. Agrait, K. W. Jacobsen, and S. Vieira, Phys. Rev. Lett. **87**, 026101 (2001).

[40] S. Link, A. Beeby, S. Fitzgerald, M. A. El-Sayed, T. G. Schaaff, and R. L. Whetten, J. Phys. Chem. B **106**, 3410 (2002).

[41] S. Burkart, Ph.D. thesis, Universität Konstanz, 2000.

[42] F. C. Tompkins, *Chemisorption of Gases on Metals* (Academic Press, London, 1978).

[43] H. Grönbeck, A. Curioni, and W. Andreoni, J. Am. Chem. Soc. **122**, 3839 (2000).

[44] R. N. Barnett and U. Landman, Phys. Rev. B **48**, 2081 (1993).

[45] R. Wesendrup, T. Hunt, and P. Schwerdtfeger, J. Chem. Phys. **112**, 9356 (2000).

[46] P. Pyykkö, Chem. Rev. **88**, 563 (1988).

[47] K. P. Huber and G. Herzberg, *Constants of diatomic molecules* (Van Norstrand-Reinholt, New York, 1979).

[48] A. Zupan, K. Burke, M. Ernzerhof, and J. Perdew, J. Chem. Phys. **106**, 10184 (1997).

[49] H. Grönbeck and W. Andreoni, Chem. Phys. **262**, 1 (2000).

[50] C.-Y. Cha, G. Ganteför, and W. Eberhardt, Rev. Sci. Instr. **63**, 5661 (1992).

[51] D. Krüger, H. Fuchs, R. Rousseau, D. Marx, and M. Parrinello, J. Chem. Phys. **115**, 4776 (2001).

[52] G. S. Icking-Konert, H. Handschuh, G. Ganteför, and W. Eberhardt, Phys. Rev. Lett. **76**, 1047 (1996).

[53] W. Andreoni and J. L. Martins, Surface Science **156**, 635 (1985).

[54] V. Bonaçiç-Koutecký, L. Cespiva, P. Fantucci, and J. Koutecký, J. Chem. Phys. **98**, 7981 (1993).

[55] F. Furche, R. Ahlrichs, P. Weis, C. Jacob, and M. Kappes, J. Chem. Phys. **117**, 6982 (2002).

[56] H. Häkkinen, M. Moseler, and U. Landman, Phys. Rev. Lett. **89**, 033401 (2002).

[57] S. Gilb, P. Weis, F. Furche, R. Ahlrichs, and M. Kappes, J. Chem. Phys. **116**, 4094 (2002).

[58] R. R. Hudgins, M. Imai, M. F. Jarrold, and P. Dugourd, J. Chem. Phys. **111**, 7865 (1999).

[59] B. Vezin, P. Dogourd, C. Bordas, D. Rayane, M. Broyer, V. Bonaçiç-Koutecký, J. Pittner, C. Fuchs, J. Gaus, and J. Koutecký, J. Chem. Phys. **102**, 2727 (1995).

[60] H. Häkkinen and U. Landman, Phys. Rev. B **62**, R2287 (2000).

[61] M. Moseler, H. Häkkinen, R. N. Barnett, and U. Landman, Phys. Rev. Lett. **86**, 2545 (2001).

[62] J. Akola, M. Manninen, H. Häkkinen, U. Landman, X. Li, and L.-S. Wang, Phys. Rev. B **62**, 13216 (2000).

[63] H. Kietzmann, J. Morenzin, P. S. Bechthold, G. Ganteför, W. Eberhardt, D.-S. Yang, P. A. Hackett, R. Fournier, T. Pang, and C. Chen, Phys. Rev. Lett. **77**, 4528 (1996).

[64] S. Burkart, N. Blessing, B. Klipp, J. Müller, G. Ganteför, and G. Seifert, Chem. Phys. Lett. **301**, 546 (1999).

[65] J. K. Burdett and T. A. McCormick, J. Phys. Chem. A **102**, 6366 (1998).

[66] P. Fuentealba and A. Savin, J. Phys. Chem. A **105**, 11531 (2001).

[67] A. D. Becke and K. E. Edgecombe, J. Chem. Phys. **92**, 5397 (1990).

[68] K. Clemenger, Phys. Rev. B **32**, 1359 (1985).

[69] K. J. Taylor, C. L. Pettiette-Hall, O. Cheshnovsky, and R. E. Smalley, J. Chem. Phys. **96**, 3319 (1992).

[70] C. Xu, T. R. Taylor, G. R. Burton, and D. M. Neumark, J. Chem. Phys. **108**, 1395 (1998).

[71] J.-L. Li, J.-F. Jia, X.-J. Liang, X. Liu, J.-Z. Wang, Q.-K. Xue, Z.-Q. Li, J. S. Tse, Z. Zhang, and S. B. Zhang, Phys. Rev. Lett. **88**, 066101 (2002).

[72] M. S. Dresselhaus, G. Dresselhaus, and P. C. Eklund, *Science of Fullerenes and Carbon Nanotubes* (Academic Press, San Diego, 1995).

[73] O. Cheshnovsky, S. H. Yang, C. L. Pettiette, M. J. Craycraft, Y. Liu, and R. E. Smalley, Chem. Phys. Lett. **138**, 119 (1987).

[74] J. Müller, B. Liu, A. A. Shvartsburg, S. Ogut, J. R. Chelikowsky, K. W. Siu, K.-M. Ho, and G. Ganteför, Phys. Rev. Lett. **85**, 1666 (2000).

[75] M. Grass, Ph.D. thesis, Universität Konstanz, 2002.

[76] D. R. Lide, *CRC Handbook of Chemistry and Physics* (CRC Press, Bocs Raton, FL, 1994).

[77] T. N. Kitsopoulos, C. J. Chick, Y. Zhao, and D. M. Neumark, J. Chem. Phys. **1441**, 8312 (1991).

[78] S. Wei, R. N. Barnett, and U. Landman, Phys. Rev. B **55**, 7935 (1997).

[79] P. Ballone, W. Andreoni, R. Car, and M. Parrinello, Phys. Rev. Lett. **60**, 271 (1998).

[80] H. Kietzmann, R. Rochow, G. Ganteför, W. Eberhardt, K. Vietze, G. Seifert, and P. Fowler, Phys. Rev. Lett. **81**, 5378 (1998).

[81] B. Klipp, M. Grass, J. Müller, D. Stolcic, U. Lutz, G. Ganteför, T. Schlenker, J. Boneberg, and P. Leiderer, Appl. Phys. A **73**, 547 (2001).

[82] W. Yamaguchi, K. Yoshimura, Y. Maruyama, K. Igaraschi, S. Tanemura, and J. Murakami, Chem. Phys. Lett. **311**, 415 (1999).

[83] S. J. Caroll, S. G. Hall, R. E. Palmer, and R. Smith, Phys. Rev. Lett. **81**, 3715 (1998).

[84] M. Grass, D. Fischer, M. Mathes, G. Ganteför, and P. Nielaba, Appl. Phys. Lett. (2002).

[85] W. Eberhardt, P. Fayet, D. M. Cox, Z. Fu, A. Kaldor, R. Sherwood, and D. Sondericker, Phys. Rev. Lett. **64**, 780 (1990).

[86] J. E. Bower and M. Jarrold, J. Chem. Phys. **97**, 8312 (1992).

[87] A. Ulman, Chem. Rev. **96**, 1533 (1996).

[88] E. Delamarche, B. Michel, H. A. Biebuyck, and C. Gerber, Adv. Mater. **8**, 719 (1996).

[89] O. Chailapakul, L. Sun, C. Xu, and R. M. Crooks, J. Am. Chem. Soc. **116**, 2225 (1994).

[90] F. P. Zamborini and R. M. Crooks, J. Am. Chem. Soc. **116**, 2225 (1994).

[91] K. Motesharei and D. C. Myles, J. Am. Chem. Soc. **120**, 7328 (1998).

[92] A. Lio, D. H. Charych, and M. Salmeron, J. Phys. Chem. B **101**, 3800 (1997).

[93] G. E. Poirier, Langmuir **15**, 1167 (1999).

[94] P. Fenter, A. Eberhardt, and P. Eisenberger, Science **266**, 1216 (1994).

[95] L. Strong and G. M. Whitesides, Langmuir **4**, 546 (1988).

[96] R. G. Nuzzo, B. R. Zegarski, and L. H. Dubois, J. Am. Chem. Soc. **109**, 733 (1987).

[97] R. G. Nuzzo, L. H. Dubois, and D. L. Allara, J. Am. Chem. Soc. **112**, 558 (1990).

[98] N. Camillone III, C. E. D. Chidsey, G. Liu, and G. Scoles, J. Chem. Phys. **98**, 3503 (1993).

[99] N. Camillone III, C. E. D. Chidsey, P. Eisenberger, P. Fenter, J. Li, K. S. Liang, G. Y. Liu, and G. Scoles, J. Chem. Phys. **99**, 744 (1993).

[100] P. Fenter, P. Eisenberger, and K. S. Liang, Phys. Rev. Lett. **70**, 2447 (1993).

[101] G. E. Poirier and M. J. Tarlov, Langmuir **10**, 2853 (1994).

[102] P. Fenter, F. Schreiber, L. Berman, G. Scholes, P. Eisenberger, and M. J. Bedzyk, Surface Science **412/413**, 213 (1998).

[103] G. J. Kluth, C. Carraro, and R. Maboudian, Phys. Rev. B **59**, R10449 (1999).

[104] K. Heister, M. Zharnikov, M. Grunze, and L. S. O. Johansson, J. Phys. Chem. B **105**, 4058 (2001).

[105] T. Ishida, S. Yamamoto, W. Mizutani, M. Motomatsu, H. Tokumoto, H. Hokari, H. Azehara, and M. Fujihira, Langmuir **13**, 3261 (1997).

[106] X. D. Cui, A. Primak, X. Zarate, J. Tomfohr, O. F. Sankey, A. L. Moore, T. A. Moore, D. Gust, G. Harris, and S. M. Lindsay, Science **294**, 571 (2001).

[107] H. S. Kato, J. Noh, M. Hara, and M. Kawai, J. Phys. Chem. B **106**, 9655 (2002).

[108] J. Pflaum, G. Bracco, F. Schreiber, R. Colorado Jr., O. E. Shmakova, T. R. Lee, G. Scoles, and A. Kahn, Surface Science **89**, 498 (2001).

[109] M. S. Yeganeh, S. M. Dougal, R. S. Polizzotti, and P. Rabinowitz, Phys. Rev. Lett. **74**, 1811 (1995).

[110] C. Wöll, S. Chiang, R. J. Wilson, and P. H. Lippel, Phys. Rev. B **39**, 7988 (1989).

[111] D. Zerulla and T. Chasse, Langmuir **15**, 5285 (1999).

[112] P. Fenter, A. Eberhardt, K. S. Liang, and P. Eisenberger, J. Chem. Phys. **106**, 1600 (1997).

[113] J. Hautman and M. L. Klein, J. Chem. Phys. **91**, 4994 (1989).

[114] W. L. Jorgenson, J. Phys. Chem. **90**, 6379 (1986).

[115] W. Mar and M. L. Klein, Langmuir **10**, 188 (1993).

[116] R. Bhatia and B. J. Garrison, Langmuir **13**, 4038 (1997).

[117] H. Sellers, Surface Science **294**, 99 (1993).

[118] A. J. Pertsin and M. Grunze, Langmuir **10**, 3668 (1994).

[119] K. M. Beardmore, J. D. Kress, N. Gronbech-Jensen, and A. R. Bishop, Chem. Phys. Lett. **286**, 40 (1998).

[120] W. Andreoni, A. Curioni, and H. Grönbeck, Int. J. Quant. Chem. **80**, 598 (2000).

[121] M. C. Vargas, P. Giannozzi, A. Selloni, and G. Scoles, J. Phys. Chem. B **105**, 9509 (2001).

[122] Y. Yourdshahyan, H. Zhang, and A. M. Rappe, Phys. Rev. B **63**, 081405(R) (2001).

[123] T. Hayashi, Y. Morikawa, and H. Nozoye, J. Chem. Phys. **114**, 7615 (2001).

[124] J. Gottschalk and B. Hammer, J. Chem. Phys. **116**, 784 (2002).

[125] B. Montanari, P. Ballone, and R. O. Jones, J. Chem. Phys. **108**, 6947 (1998).

[126] E. J. Meijer and M. Sprik, J. Chem. Phys. **105**, 864 (1996).

[127] H. Grönbeck, report, personal communication (unpublished).

[128] N. Karasawa, S. Dasgupta, and W. A. Goddard III, J. Phys. Chem. **95**, 2260 (1991).

[129] J. J. Gerdy and W. A. Goddard III, J. Am. Chem. Soc. **118**, 3233 (1996).

[130] S. L. Mayo, B. D. Olafson, and W. A. Goddard III, J. Phys. Chem. **94**, 8897 (1990).

[131] D. Bakowies and W. Thiel, J. Phys. Chem. **100**, 10580 (1996).

[132] M. Eichinger, P. Tavan, J. Hutter, and M. Parrinello, J. Chem. Phys. **110**, 10452 (1999).

[133] S. R. Billeter and A. Curioni, submitted to Comp. Mat. Sci. (unpublished).

[134] J. F. Nagle, Faraday Discuss. **81**, 151 (1986).

[135] P. Fenter, A. Eberhardt, K. Liang, and P. Eisenberger, J. Chem. Phys. **106**, 1600 (1996).

[136] L. H. Dubois, B. R. Zegarski, and R. G. Nuzzo, J. Chem. Phys. **98**, 678 (1993).

[137] T. T. Ehler, N. Malmberg, and L. J. Noe, J. Phys. Chem. B **101**, 1268 (1997).

[138] D. Fischer, A. Marti, and G. Hähner, J. Vac. Sci. Technol. A **15**, 2173 (1997).

[139] R. Arnold, A. Terfort, and C. Wöll, Langmuir **17**, 4980 (2001).

[140] N. W. Ashcroft and N. D. Mermin, *Solid State Physics* (Holt-Saunders International Editions, Oxford, 1976).

[141] P. W. Atkins, *Physical Chemistry* (Oxford University Press, Oxford, 1990).

[142] M. J. S. Dewar, E. G. Zoebisch, E. F. Healy, and J. J. P. Stewart, J. Am. Chem. Soc. **107**, 3902 (1985).

[143] "MOPAC 93", J. J. P. Stewart, Fujitsu Limited, Tokyo, Japan (1993).

[144] J. C. Slater, Phys. Rev. **35**, 210 (1930).

[145] J. P. Lowe, *Quantum Chemistry* (Acadmic Press, Orlando, FL, 1978).

[146] S. D. Kevan and R. H. Gaylord, Phys. Rev. B **36**, 5809 (1987).